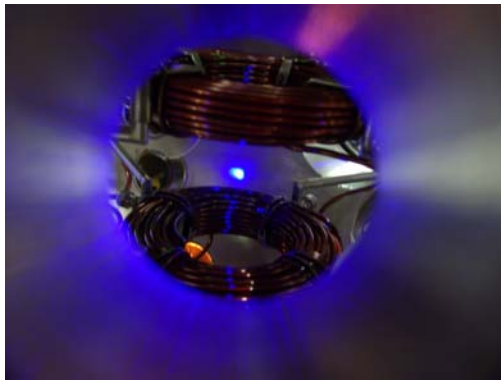


Towards the Quantum Noise Limit in Ramsey-Bordé Atom Interferometry



Von der Fakultät für Mathematik und Physik der
Gottfried Wilhelm Leibniz Universität Hannover
zur Erlangung des Grades

Doktor der Naturwissenschaften
Dr. rer. nat.

genehmigte Dissertation
von

Dipl.-Phys. Tatiana Nazarova
geboren am 27.10.1976 in Novosibirsk (Russland)

2007

Referent: Prof. Dr. Wolfgang Ertmer

Korreferent: Prof. Dr. Fritz Riehle

Tag der Promotion: 05 November 2007

Kurzzusammenfassung

Im Rahmen dieser Arbeit wurden die relevanten Rauschquellen in Atominterferometern vom Ramsey-Bordé-Typ untersucht. Dazu gehören das Rauschen durch den Anregungsprozess und das Rauschen bei der Detektion der atomaren Anregung. Im ersten Teil der Arbeit werden Methoden zur Reduzierung des Frequenzrauschens des Abfragelasers sowohl im niederfrequenten als auch im hochfrequenten Bereich vorgestellt. Eine Analyse der Kopplung der Vibrationen an den Resonator, auf den der Laser stabilisiert ist, wurde durchgeführt. Daraus wurde eine neuartige Halterung des Referenzresonators entwickelt und realisiert, mit der das Frequenzrauschen im niederfrequenten Bereich reduziert wurde. So konnte die Vibrationsempfindlichkeit um zwei Größenordnungen in der vertikalen und um eine Größenordnung in der horizontalen Richtung gegenüber dem bisherigen von unten gehaltenen Resonator verringert werden. Des Weiteren wurden die Reduzierung des hochfrequenten Frequenzrauschens durch die Filterung durch einen optischen Resonator demonstriert und der Einfluss des hochfrequenten Rauschens auf die Frequenzstabilität des Atominterferometers untersucht.

Der zweite Teil der Arbeit zeigt die erreichten Verbesserungen in der Detektion des Quantenzustands der Atome, die prinzipiell einen quantenprojektionsbegrenzten Nachweis von $4 \cdot 10^6$ Atomen erlauben. Mit dem rauscharmen Abfragelaser und der verbesserten Detektionsmethode wurden atominterferometrische Messungen an Ensembles bestehend aus $4 \cdot 10^6$ ultrakalter Calciumatome ($20 \mu\text{K}$) durchgeführt und die Kurzzeitstabilität des Atominterferometers bestimmt. Aus dem gemessenen Signal-zu-Rausch-Verhältnis wurde eine Frequenzstabilität von $\sigma_y(1 \text{ s}) = 7 \cdot 10^{-15}$ für eine Zykluszeit von 50 ms berechnet. Die nun durch den Dick-Effekt limitierte Stabilität liegt nur noch eine Größenordnung über dem Quantenprojektionsrauschlimit.

Schlagnworte: Ramsey-Bordé-Atominterferometrie, Frequenzstabilität des Atominterferometers, hochstabile Laser, Quantenprojektionsrauschen, Dick-Effekt

Abstract

In this work, the relevant noise sources in atom interferometers of Ramsey-Bordé type were investigated, which are the noise of the excitation induced by the interrogation and the noise of the detection of the excitation. In the first part of the work, the methods for the considerable reduction of the frequency noise of the interrogation laser in the low and in the high frequency range are described and demonstrated in the experiment. The coupling of vibrations onto the reference cavity was analysed and a novel mounting configuration for the reference cavity allowing to reduce the frequency noise in the low frequency range was realized. This mounting reduces the sensitivity to vibrations by two orders of magnitude in the vertical and one order of magnitude in the horizontal direction compared to the previous support from below. Furthermore, the reduction of the high-frequency laser frequency noise using the filtering through an optical cavity is demonstrated and the influence of the high-frequency noise on the frequency stability of an atom interferometer was studied.

In the second part of this work, the scheme for the detection of the quantum state of the atoms was improved. The scheme allows now the quantum projection noise limited detection of $4 \cdot 10^6$ atoms. Atom-interferometric measurements were performed on ensembles of $4 \cdot 10^6$ ultracold calcium atoms at $20 \mu\text{K}$ using the improved interrogation laser system and the improved detection scheme and the short-term stability of the atom interferometer was characterized. From the observed signal-to-noise ratio a frequency stability of the atom interferometer of $\sigma_y(1 \text{ s}) = 7 \cdot 10^{-15}$ was determined for the cycle time of 50 ms. The achieved stability, which is now limited by the Dick effect, is one order of magnitude above the quantum projection noise limit.

Keywords: Ramsey-Bordé atom interferometer, frequency stability of an atom interferometer, high stable lasers, quantum projection noise, Dick effect

List of Publications

C. Degenhardt, T. Nazarova, Ch. Lisdat, H. Stoehr, U. Sterr, and F. Riehle, "Influence of chirped excitation pulses in an optical clock with ultracold calcium atoms." *IEEE Trans. Instrum. Meas.*, **2005**, *54*, 771-775

C. Degenhardt, H. Stoehr, Ch. Lisdat, G. Wilpers, H. Schnatz, B. Lipphardt, T. Nazarova, P.-E. Pottie, U. Sterr, J. Helmcke, and F. Riehle, "Calcium optical frequency standard with ultracold atoms: Approaching 10^{-15} relative uncertainty." *Phys. Rev. A*, **2005**, *72*, 062111-1-17

T. Nazarova, Ch. Lisdat, C. Degenhardt, H. Stoehr, Ch. Grain, P.-E. Pottie, H. Schnatz, U. Sterr, and F. Riehle. "An optical clock with ultracold calcium atoms." *Annales francaises des microtechniques et de chronometrie*, **2005**, *75*, 65–69

T. Nazarova, F. Riehle, and U. Sterr, "Vibration-insensitive reference cavity for an ultra-narrow-linewidth laser." *Appl. Phys. B*, **2006**, *83*, 531-536

Ch. Grain, T. Nazarova, C. Degenhardt, F. Vogt, Ch. Lisdat, E. Tiemann, U. Sterr, and F. Riehle, "Narrow-line cooling in optical dipole traps." *Eur. Phys. J. D*, **2007**, *42*, 317-324

F. Vogt, Ch. Grain, T. Nazarova, U. Sterr, F. Riehle, Ch. Lisdat, and E. Tiemann, "Determination of the calcium ground state scattering length by photoassociation spectroscopy at large detunings," *Eur. Phys. J. D*, **2007**, *44*, 73-79.

Contents:

1. INTRODUCTION.....	3
2. RAMSEY-BORDÉ ATOM INTERFEROMETRY	7
2.1. Theoretical outline	7
2.1.1. Atom-light interaction.....	7
2.1.2. 4-pulse atom interferometer	9
2.1.3. 3-pulse atom interferometer	10
2.2. Atom interferometer as a frequency standard.....	11
2.2.1. Principles of a frequency standard.....	11
2.2.2. Frequency stability of an atom interferometer	13
2.2.3. State selective detection	13
2.3. Experimental realisation	14
2.3.1. Calcium atom	14
2.3.2. Experimental apparatus	15
2.3.3. Cooling and trapping of calcium atoms	16
2.3.4. Optimization of the cooling cycle	19
3. HIGHLY STABLE LASER SOURCE FOR ATOM INTERFEROMETRY	21
3.1. Characterization of frequency noise	21
3.2. Laser setup.....	23
3.2.1. Extended cavity diode laser	24
3.2.2. Frequency stabilization to a high-finesse cavity	24
3.2.3. Self-heterodyne technique.....	25
3.3. Vibration insensitive reference cavity	27
3.3.1. Stability of the reference cavity	27
3.3.2. FEM Simulations	30
3.3.3. Uncertainty of FEM simulations	32
3.3.4. Suspension of the cavity.....	34
3.3.5. Measurement of the vibration sensitivity	35
3.3.6. Vibration isolation.....	36
3.3.7. Fully compensated cavities	38
3.4. Suppression of high-frequency noise.....	38
3.4.1. Noise suppression by optical filtering.....	38
3.4.2. Noise of the injection-lock	40
3.4.3. Spectrum of frequency fluctuations of the interrogation laser	40
3.5. Quality of the injection-lock.....	42
3.6. Frequency stability of the laser.....	43
3.6.1. Long term drift of the reference cavity	44
3.6.2. Influence of power fluctuations	44

3.6.3.	Residual amplitude modulation	45
3.6.4.	Comparison of highly stable lasers.....	47
3.6.5.	Thermal noise	50
3.7.	Laser system at 657 nm	52
4.	NOISE IN ATOM INTERFEROMETERS	55
4.1.	Quantum projection noise	55
4.2.	Detection noise.....	56
4.2.1.	Detection noise – a model	56
4.2.2.	Optimization of the detection	60
4.2.3.	Detection performance	66
4.3.	Noise of the single pulse excitation	67
4.4.	Dick effect	69
4.5.	Noise of the Ramsey-Bordé interrogation.....	71
4.6.	Reducing the Dick effect.....	74
4.6.1.	Dick effect in the Ramsey-Bordé interrogation.....	74
4.6.2.	Dick effect in the Rabi interrogation.....	75
5.	CONCLUSIONS.....	77

1. Introduction

Interferometry is one of the most successful techniques for high precision measurements in metrology, technology, and fundamental research. Matter wave interferometry, based on the postulate made by de Broglie in 1924 that all matter has a wave-like nature, can improve the sensitivity of the interferometer by several orders of magnitude compared to the optical interferometers due to the smaller de Broglie wavelength of particles. The first experimental confirmation of this wave character was worked out by Davidson and Germer in 1927 by observing the diffraction of electrons [dav27]. This was followed by the observation of the diffraction of helium atoms on crystal surfaces [est30]. The first matter wave interferometer was realised with electrons using an electrostatic biprism as a beam splitter [moe57] followed by a neutron interferometer using a biprism [mai62] and later Bragg reflection in single crystals [rau74].

Atom interferometry enhances the interferometric method due to the smaller de Broglie wavelength of atoms compared to those of electrons and neutrons and offers new applications by exploiting the internal structure of atoms. Because of the high sensitivity to a variety of effects, atom interferometers are used in different applications such as highly sensitive gyroscopes [gus97], gravity gradiometers [mcg02], accelerometers [pet01], and optical frequency standards [ste04a], which is the emphasis of this thesis.

Like any interferometer, atom interferometers require coherent beam splitters and mirrors for matter waves. The construction of beam splitters for atoms is difficult by the fact that atoms do not carry any charge like electrons and cannot penetrate the matter like neutrons. The further challenge of the finding the suitable beam splitters for the atom interferometry is due to the small de Broglie wavelength. The first beam splitters acting only on the external degree of freedom were realized as a double slit [car91] or a micro grating [kei91]. These nanostructure optics show a disadvantage of clogging up if used with high intensity atom beams. An elegant solution of this problem is the use of the additional internal degrees of freedom of atoms. In this approach, the atomic wave function is split by the interaction of atoms with an electromagnetic field, which acts as a beam splitter, transferring the energy and momentum from the field to atoms by absorption or stimulated emission. The partial waves leave the beam splitter in a coherent superposition of the ground and the long-lived excited state where the momenta of both states differ by the transferred photon momentum. Thus, the different paths of the interferometer are labelled by the internal states of the atoms. Matter-wave interferometers are constructed by combining the beam splitters with zones of free propagation.

The first atom interferometer of this type, even not recognized as an interferometer at that time, was Ramsey's separated oscillatory fields setup for the microwave domain in 1950 [ram50], where an atomic beam passes two interaction zones separated in space. This method was used for the microwave spectroscopy, especially for the realisation of the caesium atomic clock by Essen and Parry in 1955 [ess55a]. It was later extended to the optical domain first theoretically by Baklanov [bak76] and later experimentally by Bergquist *et al.* [ber77b] using three beam splitters and by Helmcke *et al.* [hel82] and Bordé *et al.* [bor84] using four beam splitters. Only as late as 1989 Bordé discovered that the four-zone optical Ramsey excitation scheme forms an atom interferometer in the Mach-Zehnder configuration, where the laser beams split, deflect, and recombine the atomic wave function.

The first experiments with atom interferometers were carried out on atomic beams, i.e. the Mach-Zehnder interferometer was built by four laser beams separated in space. In this case, the time between the pulses, which gives the resolution of the interferometer, is limited by the velocity of the atomic beam. Furthermore, the achievable uncertainty is limited by not fully compensated linear and quadratic Doppler effect. A big improvement in this respect was the use of laser cooled atoms [phi85], which allows to apply the pulses separated in time. Thus, the Mach-Zehnder interferometer in the time domain does not depend on the velocity of the atoms but can be adjusted by the separation time between the pulses [bor89].

The essential point for understanding of this kind of the atom interferometry is the imprint of the instantaneous phase of the laser beam on the phase of the atomic wave function at the interaction points. This allows one to vary the interference signal of the interferometer via the phase of the laser beam, i.e. the phase of the beam splitter. The use of this kind of the atom interferometer allowed the precise determination of the dc- and ac- polarizability of atoms [ste92, rie92a] or of the quadratic Zeeman effect [bev87a].

Different interferometer geometries can be constructed using variable numbers of the beam splitters. In general, one distinguishes between asymmetric and symmetric interferometers. In the asymmetric interferometers, the laser beams come from the opposite directions. Thus, the partial waves have different trajectories, where they accumulate different phases. The total phase shift of the interference signal depends linearly on the laser frequency. This kind of interferometers is used for creating high precision frequency standards [bor89]. In the symmetric interferometers, all beam splitting laser beams are applied from the same direction. Since all partial waves have spent the same time in the ground and excited state, the phase of the interferometric signal does not depend on the laser frequency in the first order. However, keeping in mind the imprint of the instantaneous laser phase on the phase of the atomic wave function, the important role of the lasers in the atom interferometry becomes visible because the phase fluctuations of the laser introduce noise in the measurement. Similar to optical interferometers, where mechanical fluctuations of beam splitters lead to the noise of the interference signal, the fluctuations of the beams splitters for the matter wave, i.e. the frequency fluctuations of the laser beams, also introduce noise in the measurements. Thus, highly stable and narrow-linewidth lasers are required. A high frequency stability of a atom interferometer is inevitable because this allows us to achieve the desired accuracy within a realistic measurement time. The condition of the narrow linewidth is essential for resolving the narrow atomic transition.

As interferometry is a technique for very accurate measurements, it is important to find the principal limits of the achievable accuracy. In general, the principal limit of the accuracy is given by the fluctuations of the detected phase. In an atom interferometer with independent particles, the so-called quantum projection noise [ita93] leads to the minimal detectable phase scaling with the number N of particles as $N^{-1/2}$ [jac95]. This limit can be reduced by using non-independent particles (like a Bose-Einstein condensate [bou97]) or by spin squeezing leading [win92] to the Heisenberg limit, which scales as $1/N$. However, in practice the signal-to-noise ratio of the interferometric signal is dominated by technical influences, e.g. the noise of the detection of the quantum state of the atoms on the exit of the interferometer. In order not to be limited by the shot noise of the detected photons, the so-called electron-shelving detection scheme is widely used in atom interferometric measurements. It was first proposed by Dehmelt for a single trapped ion [deh75] and realized for a single Ba^+ ion by [nag86]. It collects the fluorescence from the strong cycling transition also used for cooling. This detection

scheme enables in principle spectroscopic measurements only limited by the quantum projection noise, which is routinely reached in measurements with single ions [pei06]. Extending the electron-shelving scheme to measurements with a big number of neutral atoms (10^5 to 10^7) one faces the problem of atom number fluctuations from cycle to cycle. Thus, the detection scheme often is modified by adding a normalization process.

Unlike the optical interferometers, where the fringes are observed continuously, most atom interferometers are operating in a discontinuous mode because the atomic ensemble are cooled and prepared for the interrogation in each cycle. Thus, the atom interferometers are suffering from the Dick effect [dic87], where the high-frequency laser frequency noise is converted to the low frequency range due to aliasing and can degrade the signal-to-noise ratio. Even with the state-of-the-art laser linewidth of one Hertz the Dick effect leads to a signal-to-noise ratio, which can be two orders of magnitude above the quantum projection noise [deg05a].

The focus of this thesis is the investigation of the principal limits in atom interferometers of the Ramsey-Bordé type and the methods, which would allow us to reach the fundamental limit by reducing the technical influences appearing in the interferometric measurements.

An essential step towards the quantum projection limit is the reduction of the frequency noise of the laser in both the low and the high frequency range. In the low frequency range the frequency noise is mostly caused by acoustic vibrations acting on the reference cavity, which the laser is stabilized to. In this work a novel vibration insensitive reference cavity was invented, which reduces the sensitivity to vibrations by two orders of magnitude compared to the previous used support [naz06]. Further influences on the frequency stability in this range caused by the residual amplitude modulation and fluctuation of the coupled laser power are studied. Moreover, the reduction of the high-frequency laser frequency noise using the filtering through an optical cavity is shown. Due to this improvement the influence of the Dick effect was reduced by a factor of three.

Furthermore, in the present work the noise of the detection of the quantum state of the atoms after performing the interferometry is examined and reduced. Therefore the influences of the frequency and amplitude fluctuations of the detection laser on the signal-to-noise ratio are studied and the ways for their reduction are shown.

This work is organised as follows:

- In Chapter 2 a theoretical outline of Ramsey-Bordé atom interferometry is given. A particular application of the atom interferometer as a frequency standard is introduced as well as the realisation of the new improved experimental setup is described.
- Chapter 3 focuses on the highly stable ultra narrow linewidth laser sources for the atom interferometry. It describes a novel vibration-insensitive reference cavity, which allows one to reduce the frequency noise in the low-frequency range. Other effects, which influence the frequency stability of the laser in the low-frequency range as the residual amplitude modulation and the fluctuations of the coupled power are characterized. Furthermore, the method for the reduction of the high-frequency noise is described and the result from a comparison of highly stable lasers is shown.

- Finally a comprehensive investigation of the relevant noise sources in atom interferometers is presented in Chapter 4. The scheme for the detection of the excitation probability based on a standing wave is introduced, which has advantages compared to the previously used propagating wave configuration. Finally, the improvements obtained with these measures are evaluated by using Ramsey-Bordé interferometry.

2. Ramsey-Bordé atom interferometry

2.1. Theoretical outline

In analogy to optical interferometers, atom interferometers require coherent beam splitters and mirrors for matter wave. They are realised by the interaction of an atom with a resonant laser beam. The absorption or stimulated emission of a photon leads to a coherent superposition of partial waves of the ground and excited state and a change of the momentum. A suitable application of several interaction zones, which split, deflect, and recombine the atomic wave function, results in atom interferences.

In the subsection 2.1.1 the formalism describing the interaction between a laser beam and an atom is developed. In the following subsections the symmetric and asymmetric atom interferometers are introduced and their distinctions are discussed. The phase shift of the interferometric signal is derived.

2.1.1. Atom-light interaction

In the following the interaction of a two-level atom with momentum \vec{p}_0 with a plane wave with wavevector $\pm\vec{k}$ is described in the rotation-wave-approximation (RWA) [bor84]. The atomic wave function $|\Psi\rangle$ can be expanded in terms of the momentum eigenstates of the ground $|g\rangle$ and excited $|e\rangle$ states

$$|\Psi\rangle = b_{m\pm 1} \left| e, \vec{p}_0 + (m \pm 1)\hbar\vec{k} \right\rangle + a_m \left| g, \vec{p}_0 + m\hbar\vec{k} \right\rangle. \quad (2.1)$$

The number m represents the number of photons exchange in the previous interaction zones with the laser beam of the direction $\pm\vec{k}$. The time development of the quantum system can be described by means of a 2×2 matrix M [bor84]:

$$\begin{pmatrix} b_{m\pm 1}(t_0 + \tau) \\ a_m(t_0 + \tau) \end{pmatrix} = e^{i\Omega_0\tau/2} M(\tau, \varphi) \begin{pmatrix} b_{m\pm 1}(t_0) \\ a_m(t_0) \end{pmatrix}, \quad (2.2)$$

with the unitary matrix

$$M(\tau, \varphi) = \begin{pmatrix} A & B e^{-i\varphi} \\ C e^{i\varphi} & D \end{pmatrix}. \quad (2.3)$$

In RWA frame, the components of the matrix are in case of rectangular excitation pulses of duration τ

$$\begin{aligned} A = D^* &= \cos\left(\frac{\Omega_{eff}\tau}{2}\right) + i \frac{\Delta_m}{\Omega_{eff}} \sin\left(\frac{\Omega_{eff}\tau}{2}\right) \\ B = -C^* &= i \frac{\Omega_{res}}{\Omega_{eff}} \sin\left(\frac{\Omega_{eff}\tau}{2}\right) \end{aligned} \quad (2.4)$$

The coefficients

$$\begin{aligned}
 \Delta_m &= 2\pi \left(\nu_L - \nu_{Ca} \mp \frac{\nu \nu_{Ca}}{c} + (\mp 2m - 1) \delta_{rec} \right), \\
 \Omega_{res} &= \sqrt{\frac{3c^2 \gamma I}{2\pi \hbar \nu_{Ca}^3}}, \\
 \Omega_{eff} &= \sqrt{\Omega_{res}^2 + \Delta_m^2}
 \end{aligned} \tag{2.5}$$

are the effective detuning Δ_m between the frequency of the atomic transition ν_{Ca} and the frequency of the interrogation laser ν_L seen by the atom, the resonant Rabi-frequency Ω_{res} and the effective Rabi-frequency Ω_{eff} for the non-resonant interaction with the laser pulses. The detuning Δ_m takes into account not only the detuning of the laser but also the Doppler-shift due to the velocity of the atom and the photon recoil δ due to exchange photons in previous interaction zones. The photon recoil is given by

$$\delta_{rec} = \frac{h \nu_{Ca}^2}{2m_{Ca} c^2} \tag{2.6}$$

and amounts to $2\delta_{rec} = 23.1$ kHz.

The excitation probability depends on the intensity I of the laser field, the duration of the excitation pulse τ and the detuning Δ_m . These parameters can be chosen in a such way that the excitation pulse acts as a 50% beam splitter ($\Omega_{res} \tau = \pi/2$, i.e. a $\pi/2$ -pulse) or a mirror ($\Omega_{res} \tau = \pi$, i.e. a π -pulse), resulting in a population inversion.

The instantaneous phase of the laser beam at the points of interaction is imprinted on the phase of the atomic wave function. The phase of the i^{th} interaction zone is given by the phase of the laser field at the position r_i and at the time t_i as:

$$\phi_i = \pm (\vec{k}_i \cdot \vec{r}_i - 2\pi \nu_L t_i + \varphi_i) \tag{2.7}$$

The sign is negative in case of absorption and positive in case of stimulated emission, φ_i is an additional phase shift of the laser field (e.g. imprinted through an additional phase shifter in the experiment).

Between the interaction zones during the dark time T a free evolution of the atomic wave function occurs. This is described using (2.2)-(2.4) with $\Omega = 0$

$$\begin{pmatrix} b_{m\pm 1}(t_0 + T) \\ a_m(t_0 + T) \end{pmatrix} = e^{i\Omega_0 T/2} \begin{pmatrix} e^{i\Delta_m T/2} & 0 \\ 0 & e^{-i\Delta_m T/2} \end{pmatrix} \begin{pmatrix} b_{m\pm 1}(t_0) \\ a_m(t_0) \end{pmatrix}. \tag{2.8}$$

Due to their different internal energies the ground and the excited state accumulate different phases during the dark time.

Using (2.2) and (2.8) all possible interferometer geometries can be described. As an example we consider the method of separated oscillatory fields that was developed by Ramsey [ram50] for the microwave domain. It consists of two identical $\pi/2$ -pulses. The interference signal is proportional to $(1 + \cos(2\pi(\Delta - \delta - \nu/\lambda)T + (\phi_2 - \phi_1)))$ and periodic in $\nu T/\lambda$, where ν is the velocity of atoms. The interference fringes are preserved when $\sigma_\nu T < \lambda$, with σ_ν the width of the velocity distribution. In the opposite case the velocity distribution averages out the fringes (so-called Doppler-dephasing).

In the optical atom interferometer, in general the latter case is observed because of the smaller wave length of the laser field compared to that of the microwave field. The velocity distribution of an atomic ensemble of cold atoms is bigger than the interaction

broadened line width of the transition $\gamma_{IA} = 1/(2\pi\tau)$. Only atoms with the Doppler-shift smaller than γ_{IA} contribute to the interferometric signal. Using $\gamma_{IA} = \sigma_v/\lambda$ one finds the condition for the pulse separation time $T < 2\pi\tau$, which indicates that the interference fringes are averaged out already for a pulse separation time in order of several pulse width τ .

Ramsey spectroscopy was modified for the optical domain by [bak76] and [ber77b]. To solve the problem of washing out of the interference fringes, a suitable geometry was used with three and more interaction zones, where the partial wave packets are overlapped in the last interaction zone leading to closed geometries. In this case the interference signal is first-order Doppler-shift free. In the following two interferometer geometries used in this work are discussed in more detail.

2.1.2. 4-pulse atom interferometer

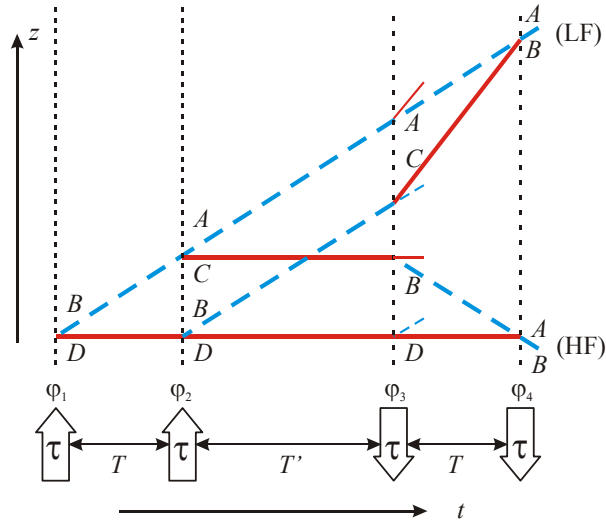


Fig. 2.1 Four-pulse Ramsey-Bordé interferometer in the time domain. The solid lines indicate the trajectories of the atomic wave packets in the ground state, the dashed lined in the excited state. The letters indicate the coefficients of the unitary matrix M as given in (2.4)

The 4-pulse Ramsey-Bordé atom interferometer in the time domain is similar to a classical optical Mach-Zehnder interferometer. In an optical interferometer the light is split with one beam splitter. Both beams propagate free in space until they are recombined on the second beam splitter. The two outputs of the interferometer show interference pattern depending on the length difference between the two arms of the interferometer. In a light-atom interferometer the two states of the atom can be considered as the two arms of an optical interferometer.

An asymmetric 4-pulse atom interferometer consists of four rectangular pulses of collimated, propagating laser beams which are applied in two counter-propagating pairs (Fig. 2.1). The pulse width τ is chosen together with the intensity of the laser beam so that it provides an excitation probability of 0.5 for the atoms ($\pi/2$ -pulse). The first pulse splits the atomic wave function into a superposition of the ground and excited state wave function like a beam splitter and changes the momentum of the deflected partial wave by one photon recoil. This change of the momentum leads to a separation of the partial wave functions during the dark time T (also called pulse separation time). The second and the third pulses redirect the separated trajectories while the fourth pulse recombines the both paths of the partial wave functions. The time between the second and the third pulse is denoted as T' . Thus, two closed interferometer geometries exist

with different numbers of photon recoils.

At the exits of the atom interferometer the probability p_e to find the atom in the excited state depends on the phase difference accumulated by the partial wave functions on their paths. This phase is a function of the detuning of the frequency of the excitation pulse ν_L with respect to the atomic transition ν_{Ca} . The overall excitation probability p_e is derived using (2.2) and (2.8) in [bor84] as

$$\begin{aligned}
 p_{HF} &= \left((BCBA)(DDDB)^* \exp(i[4\pi T(\nu_L - \nu_{Ca} - \delta) + \Delta\Psi]) + c.c \right) \exp(-\gamma(T + 2\tau)) + \\
 &\quad \left(|BCDB|^2 + |DDBA|^2 + |BCBA|^2 \exp(-\gamma T) + |DDDB|^2 \exp(\gamma T) \right) \exp(-\gamma(T + 2\tau)) \\
 p_{LF} &= \left((BAAA)(DBCB)^* \exp(i[4\pi T(\nu_L - \nu_{Ca} - \delta) + \Delta\Psi]) + c.c \right) \exp(-\gamma(T + 2\tau)) + \\
 &\quad \left(|BACB|^2 + |DBAA|^2 + |BAAA|^2 \exp(-\gamma T) + |DBCB|^2 \exp(\gamma T) \right) \exp(-\gamma T) \\
 p_e &= p_{HF} + p_{LF}
 \end{aligned} \tag{2.9}$$

The excitation probability p_e oscillates with a period

$$\Delta_{fringe} = \frac{1}{2(T + \eta\tau)}, \tag{2.10}$$

where $(T + \eta\tau)$ is the effective pulse separation time with $\eta = 4/\pi$ for resonant rectangular pulses [van89a]. The resolution of the atom interference is given as the half-width of the fringes

$$\Delta = \frac{1}{4(T + \eta\tau)}. \tag{2.11}$$

The two recoil patterns have the same period but are shifted with respect to each other by twice the recoil shift δ . The high frequency interferometer (HF) is centred at $(\nu_{Ca} + \delta)$ and the low frequency (LF) at $(\nu_{Ca} - \delta)$. To achieve the optimal contrast, the resolution must be set to an integer fraction of the recoil splitting 2δ allowing the two interference pattern to interfere constructively

$$(T + \eta\tau) = \frac{n}{2\delta}. \tag{2.12}$$

Besides the detuning of the laser with respect to the atomic resonance also the phase shift of

$$\Delta\Psi = \varphi_4 - \varphi_3 + \varphi_2 - \varphi_1 \tag{2.13}$$

contributes to the interference signal.

In this treatment the possibility of re-excitation of atoms after the decay in one of the following interaction zones is not taken into account. However, this incoherent excitation does not contribute to the interferometric signal but to the background.

2.1.3. 3-pulse atom interferometer

A symmetrical 3-pulse atom interferometer (Fig. 2.2) consists of three laser beams propagating in the same direction with a pulse separation time T . Here, the second pulse is a π -pulse. The excitation probability p_e at the output of the interferometer can be calculated using (2.2) and (2.8) as

$$p = \left((DBA)(BCB)^* \exp(i[\Delta\Psi]) + c.c \right) \exp(-\gamma(T+2\tau)) + \left(|DBA|^2 + |BCB|^2 + |BAA|^2 \exp(-\gamma T) + |DDB|^2 \exp(\gamma T) \right) \exp(-\gamma(T+2\tau)) \quad (2.14)$$

Since the atom stays in both interferometer paths the same time in the ground and the excited state the interference signal is independent of the laser frequency and oscillates with the phase difference

$$\Delta\Psi = -\varphi_1 + 2\varphi_2 - \varphi_3. \quad (2.15)$$

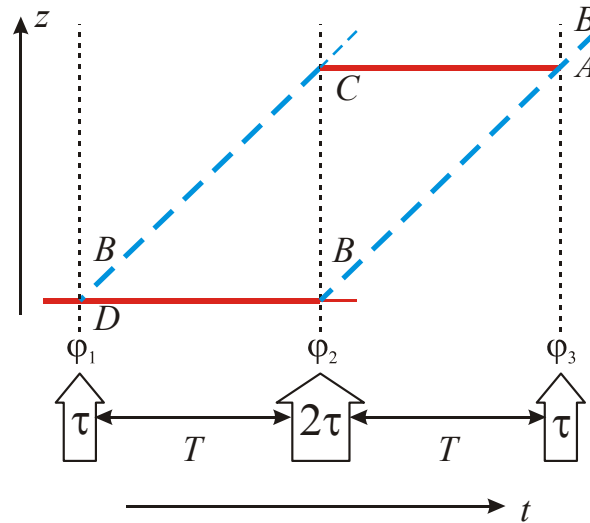


Fig. 2.2 Three pulse Ramsey-Bordé interferometer in the time domain. The solid lines indicate the trajectories of the atomic wave packets in the ground state, the dashed lines in the excited state. The letters indicate the coefficients of the unitary matrix M as given in (2.4)

2.2. Atom interferometer as a frequency standard

2.2.1. Principles of a frequency standard

One of the applications for an atom interferometer is its use as a frequency standard. The general principle of a frequency standard is shown in Fig. 2.3.

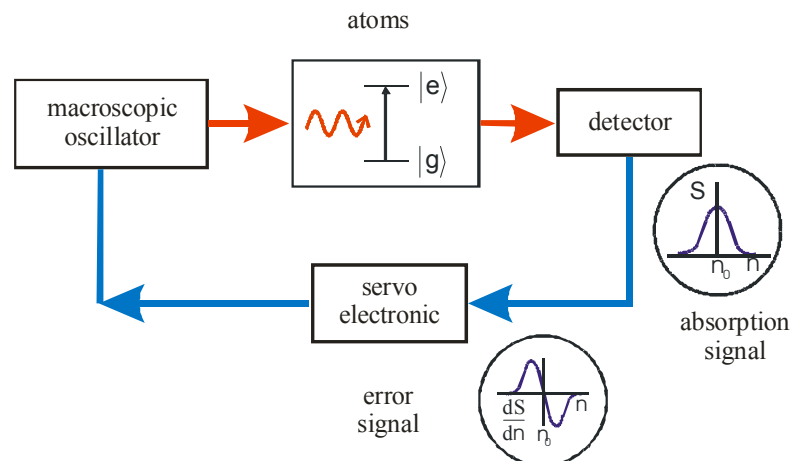


Fig. 2.3 Schematics of a frequency standard

A frequency standard consists of an macroscopic oscillator (e.g. a highly stable laser) and a frequency reference (e.g. an ensemble of atoms). For the precision spectroscopy Doppler-free techniques must be applied in order to reduce the sensitivity to the first-order Doppler shift. One well known technique is the saturation spectroscopy, where two pulses from opposite directions interact with atoms producing a saturation dip in the centre of the velocity distribution, because the atoms with velocities around zero are resonant with both beams. The resolution of the saturation spectroscopy is given by the Fourier transformation of the width of a single pulse. Thus, the pulse must become longer to achieve better resolution. Longer pulses however lead to a smaller range of velocities which can be excited so that less atoms contribute to the signal. Another technique is to interrogate the atomic transition using a frequency-dependent 4-pulse Ramsey-Bordé atom interferometer. The advantage of the Ramsey-Bordé interferometry is that it provides high spectral resolution, which is determined by the pulse separation time, and at the same time the whole velocity distribution of the atoms can be addressed with short pulses.

The interrogation signal leads to an excitation probability p_e with a maximum or minimum of the absorption at the resonance frequency ν_0 . From this signal an anti-symmetric error signal is derived and fed back to the oscillator. When the servo loop is closed the oscillator is locked to the reference frequency ν_0 (i.e. the atomic transition). In this case any noise in the interrogation of the atomic line is converted to frequency fluctuations of the oscillator. The excitation probability close to the resonance frequency can be calculated by averaging (2.9)

$$p_e(\nu) = p_{mean}(1 + C \cdot \cos(4\pi T(\nu - \nu_0) + \phi_2 - \phi_1 + \phi_4 - \phi_3)), \quad (2.16)$$

where p_{mean} is the mean excitation probability, C the contrast, and ν the instantaneous frequency of the interrogation laser (see Fig. 2.4).

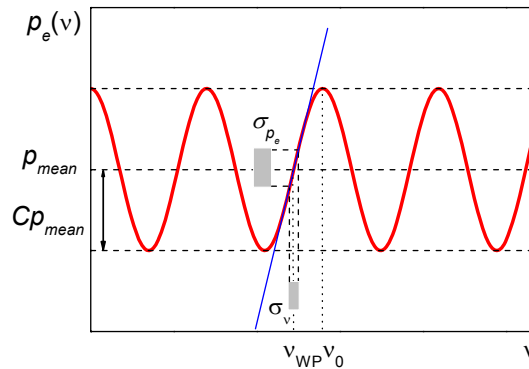


Fig. 2.4 Excitation probability p_e close to the resonance for a 4-pulse Ramsey-Bordé atom interferometer with an average excitation probability p_{mean} and contrast C .

In order to keep the laser frequency as close as possible to the frequency of the atomic transition, the working point ν_{WP} should be chosen as that with the steepest slope. This provides the highest possible sensitivity to the frequency fluctuations of the laser. Let σ_ν be the frequency fluctuations of the interrogation laser at the working point and σ_{p_e} the corresponding fluctuations of the measured excitation probability. Both fluctuations are linked by the slope of the interference fringes at the working point as follows:

$$\sigma_{p_e} = \frac{dp_e}{d\nu} \sigma_\nu. \quad (2.17)$$

Using (2.16) the noise in the measured excitation probability at the working point can be determined in case when no additional laser phase noise is introduced as

$$\sigma_{p_e} = 4\pi T C p_{mean} \sigma_v. \quad (2.18)$$

2.2.2. Frequency stability of an atom interferometer

In the particular application of an atom interferometer as a frequency standard not only the accuracy of the measurements is important but also the high frequency stability is essential, because it allows us to reach the accuracy within the realistic measurement time.

The frequency stability is often described by Allan standard deviation [all66]

$$\sigma_y(\tau) = \frac{1}{\nu_0} \sqrt{\frac{1}{2(n-1)} \sum_{k=1}^{n-1} (\overline{\nu_{k+1}} - \overline{\nu_k})^2}, \quad (2.19)$$

where $\overline{\nu_k}$ is the average frequency within interval k of the duration τ and ν_0 is the oscillator frequency. The Allan standard deviation is discussed more in detail in subsection 3.1.

For white noise in σ_{p_e} , i.e. assuming uncorrelated fluctuations between the successive interrogations, the frequency stability of a frequency standard $\sigma_y(\tau)$ can be derived from (2.17) using $\sigma_v = \nu_0 \sigma_y(\tau)$

$$\sigma_y(\tau) = \frac{1}{\pi} \frac{1}{Q} \frac{1}{S/\mathbf{N}} \sqrt{\frac{T_c}{\tau}}, \quad (2.20)$$

where $Q = \nu_{Ca}/\Delta\nu$ is the quality factor of the atomic line with $\Delta\nu = 4\pi T$ the resolution of the fringe. S denotes the signal amplitude which is given by $S = C p_{mean}$. $\mathbf{N} = \sigma_{p_e}$ is the noise of the detection performed in a measurement cycle of the duration T_c . For white noise the frequency stability averages down like the inverse square root of the averaging time τ .

2.2.3. State selective detection

After performing the atom interferometry the excitation probability of the atoms has to be measured. A sufficient signal-to-noise ratio of the detection is requested e.g. to achieve the ultimate high stability, when an atom interferometer is used as an atomic frequency standard. One method to measure the number of atoms, which leave the atom interferometer in the excited state, is to detect the fluorescence of the atoms on the clock transition itself (i.e. at 657 nm for ^{40}Ca as shown in Fig. 2.6) when they decay from the excited state and emit photons. Because of the small solid angle of the detection and PMT detection efficiency the probability to detect an excited atom is about 10^{-3} . Thus the measured signal-to-noise ratio is given by the shot-noise of the detected photons. In addition the measured fluorescence and thus the excitation probability depends on the atom number and fluctuates from cycle to cycle.

A better alternative is the so called electron-shelving technique. The idea was first proposed by Dehmelt for a single trapped ion [nag86]. If the ion is in the ground state and the resonant cooling beam shines on the ion fluorescence can be measured (Fig. 2.5, left). In case if the ion is in the excited state no fluorescence can be collected (Fig. 2.5, right). With single ions the quantum state of the ion can be detected perfectly. Working with a large number of neutral atoms one faces the problem of atom number fluctua-

tions from cycle to cycle. Thus, the scheme is modified as the following: Directly after the atom interferometry a laser pulse of 40 μs pulse duration resonant with the broad cooling transition $^1\text{S}_0$ - $^1\text{P}_1$ at 423 nm shines on the atoms.

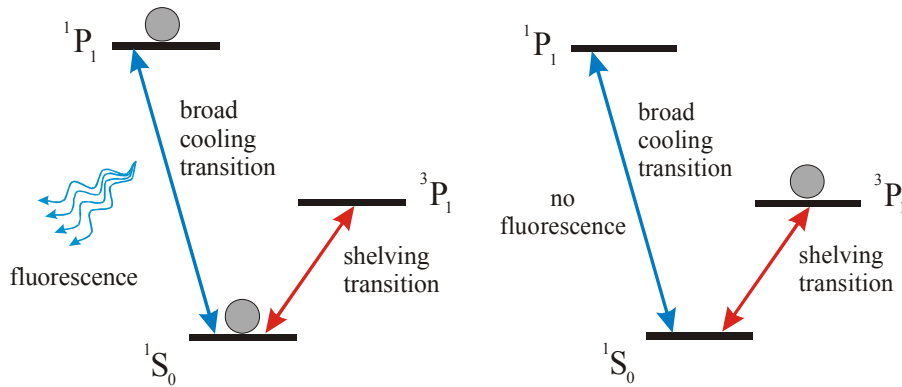


Fig. 2.5 Electron-shelving detection. On the left-hand side: the atom is not in the excited state $^3\text{P}_1$, thus the light resonant with the cooling transition excites the atom, which immediately decays emitting fluorescence. On the right-hand side: the atom is in the excited state $^3\text{P}_1$, so no fluorescence can be detected.

The measured fluorescence signal I_1 is proportional to the number of atoms leaving the atom interferometer in the ground state. Then these atoms are removed either by radiation pressure of the pulse itself (in case of the detection with a propagating wave) or by a separate pulse (as in case of the detection with a standing wave). After a delay of approx. 1 ms corresponding to twice the lifetime of the excited state a second detection pulse is applied. The fluorescence signal I_2 is proportional to the number of atoms in the excited state directly after the atom interferometry. Thus, two detection pulses are necessary to get a normalized excitation probability. In this simple model both measured signals have the same proportionality factors and the excitation probability is independent of the detected atom number and frequency and power fluctuations of the detection laser from cycle to cycle.

The excitation probability is defined as

$$p_e = N_e / (N_g + N_e), \quad (2.21)$$

where N_e and N_g is the number of atoms in the excited and the ground state respectively. In the experiment, the ratio n is measured

$$n = I_2 / (I_1 + I_2). \quad (2.22)$$

The measured ratio is equal to the excitation probability only if $I_1 \propto N_g$ and $I_2 \propto N_e$. In the experiment, however, corrections must be done. This will be discussed in subsection 4.2.1.

2.3. Experimental realisation

2.3.1. Calcium atom

The experiments presented in this work were performed on ^{40}Ca . An excerpt from the level scheme is shown in Fig. 2.6. Calcium is an earth alkaline metal. Due to a symmetric nuclear structure the bosonic isotope has no hyperfine splitting. Furthermore, it possesses a narrow intercombination transition at 657 nm with a natural linewidth of

375 Hz [deg05a]. These features make ^{40}Ca an attractive candidate for atom interferometry and frequency standards since the narrow line enables a good resolution while the absence of the hyperfine splitting in the ground state results in low sensitivity to external electrical and magnetic fields.

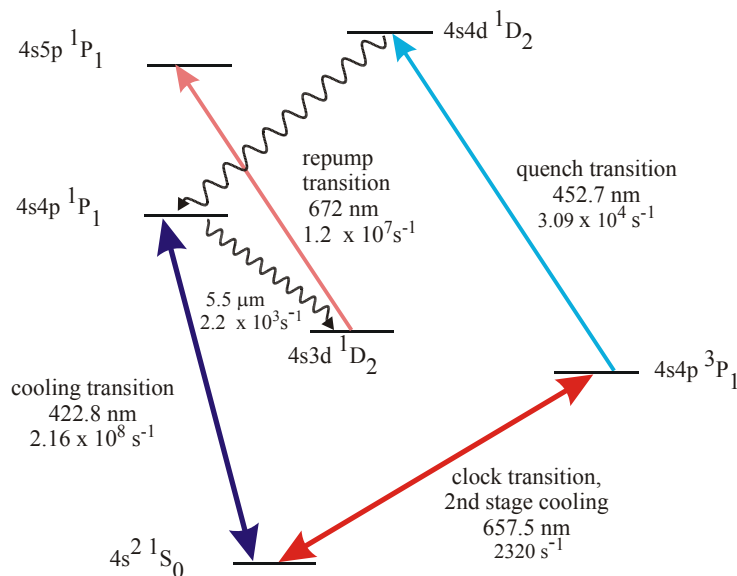


Fig. 2.6 Partial energy level diagram of calcium. Only transitions relevant for this work are shown. The positions of the energy levels are not to scale. The numbers are the corresponding wavelengths and the Einstein A coefficients of the transition.

Ca atoms are first cooled on the allowed $^1S_0 - ^1P_1$ transition at 422.8 nm. From the 1P_1 -state a weak loss channel with a probability of 10^{-5} to the 1D_2 -state exists [lel87, bev89]. From the 1D_2 -state the atoms decay to the metastable 3P_2 and long-lived 3P_1 states and are lost for the cooling process. This loss channel is closed by an additional laser at 672 nm (so-called repumper laser), which pumps the atoms into $4s5p^1P_1$ -state, from where they decay to the $4s4p^1S_0$ -state. Due to the broad linewidth of the $^1S_0 - ^1P_1$ transition of 35 MHz the Doppler limit amounts to 0.8 mK. In the experiment the reached temperatures of 1.5 mK are slightly higher.

The known sub-Doppler cooling methods can not be applied in case of ^{40}Ca since they are based on the magnetic substructure of the ground state. In order to enable temperatures in the microkelvin range, the so-called quenched narrow-line cooling is used [bin01a, ste03], where the intercombination line itself is used for further cooling. Due to the narrow linewidth of the transition the maximal cooling force is only 1.5 times larger than the gravity force. Thus, an additional laser at 453 nm (quench laser) is used in order to shorten the lifetime of $4s4p^3P_1$ -state due to the excitation in $4s4d^1D_1$ -state resulting in the increasing of the cooling force. The quench cooling step leads to the final temperature of an atomic ensemble of 10 μK [deg05a].

2.3.2. Experimental apparatus

During this work a new experimental apparatus was built. The previous vacuum chamber [wil02] was originally designed for use as a transportable frequency standard and thus was built in a very compact way. Since no Zeeman slower was used, only a small fraction of the atoms were loaded into the magneto-optical trap (MOT) from the thermal atomic beam. This resulted in a low loading rate for the atoms, e.g. in order to get 10^7 ultracold atoms a loading time of 320 ms was necessary [deg05a]. As it is shown

in subsection 4.4, a low repetition rate degrades the stability of an atom interferometer via the Dick effect. Furthermore, the black-body shift of the oven seen by the atoms in the MOT was the dominant contribution in the uncertainty budget of the Ca-frequency standard [deg05a]. These were the main motivations to build a new chamber. The new setup includes a Zeeman slower, which increases the loading rate, and a 2D molasses, which deflects the atom into the MOT preventing them from the black body radiation of the oven. The further advantages of the new chamber are a better optical access due to bigger windows, a better vacuum ($p = 1 \cdot 10^{-9}$ mbar), and a longer lifetime of the MOT since there are no collisions with the hot background atoms from the atomic beam.

The schematic drawing of the new experimental setup is shown in Fig. 2.8. The beam of thermal calcium atoms stems from an oven reservoir that is filled with approx. 2 g calcium granulates. The oven is a stainless steel cylinder of 40 mm length and an inner diameter of 9 mm. The cylinder is heated by the surrounded heating wire to a temperature of 630 K. The nozzle has seven bores of approx. 0.5 mm diameter and 10 mm length. The lifetime of the filling of the oven is about 2200 hours.

2.3.3. Cooling and trapping of calcium atoms

The frequencies of the laser cooling beams used for the cooling on the broad transition are shown in Fig. 2.7. The light from the frequency doubler (see Fig. 2.8) is locked to the atomic transition. First, the atoms from the thermal beam are decelerated by a Zeeman slower technique described in detail in [wit92, wit92a]. A laser beam with a detuning corresponding to the Doppler shift of the moving atoms is cooling the thermal atomic beam. Since the atoms get soon out of resonance, they cannot be further cooled. Using a Zeeman slower the magnetic field can be varied spatially along the beam path keeping the atomic transition in resonance with the laser beam. When the atoms leave the Zeeman slower they are still in resonance with the laser beam. They are further cooled and possibly can not reach the MOT region. Thus, at the exit of the Zeeman slower the magnetic field has to be changed in that way that the atoms are not in resonance with the cooling beam anymore. This is done in our case by means of the so-called anti-phase coil.

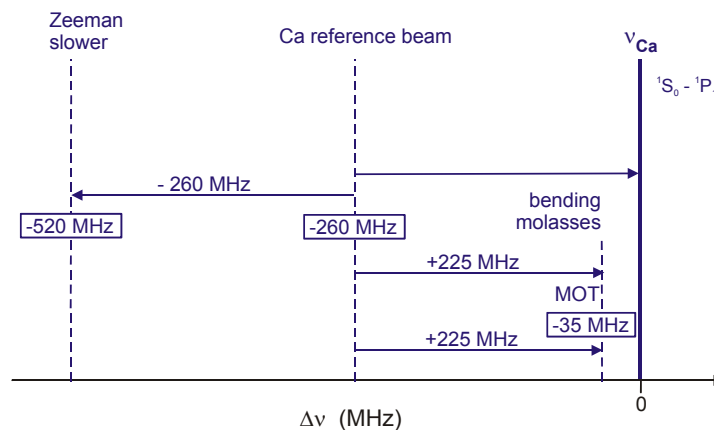


Fig. 2.7 Frequency distribution of the laser cooling beams for the cooling on the broad cooling transition $^1S_0-^1P_1$. The values in boxes give the absolute detuning from the atomic transition, the other values are the frequencies of the AOMs.

The Zeeman slower laser cooling beam is red detuned by 520 MHz from the $^1S_0-^1P_1$ transition, has a power of 50 mW and is focused by a lens system of $f = 100$ mm and $f = 150$ mm onto the entrance port of the slower.

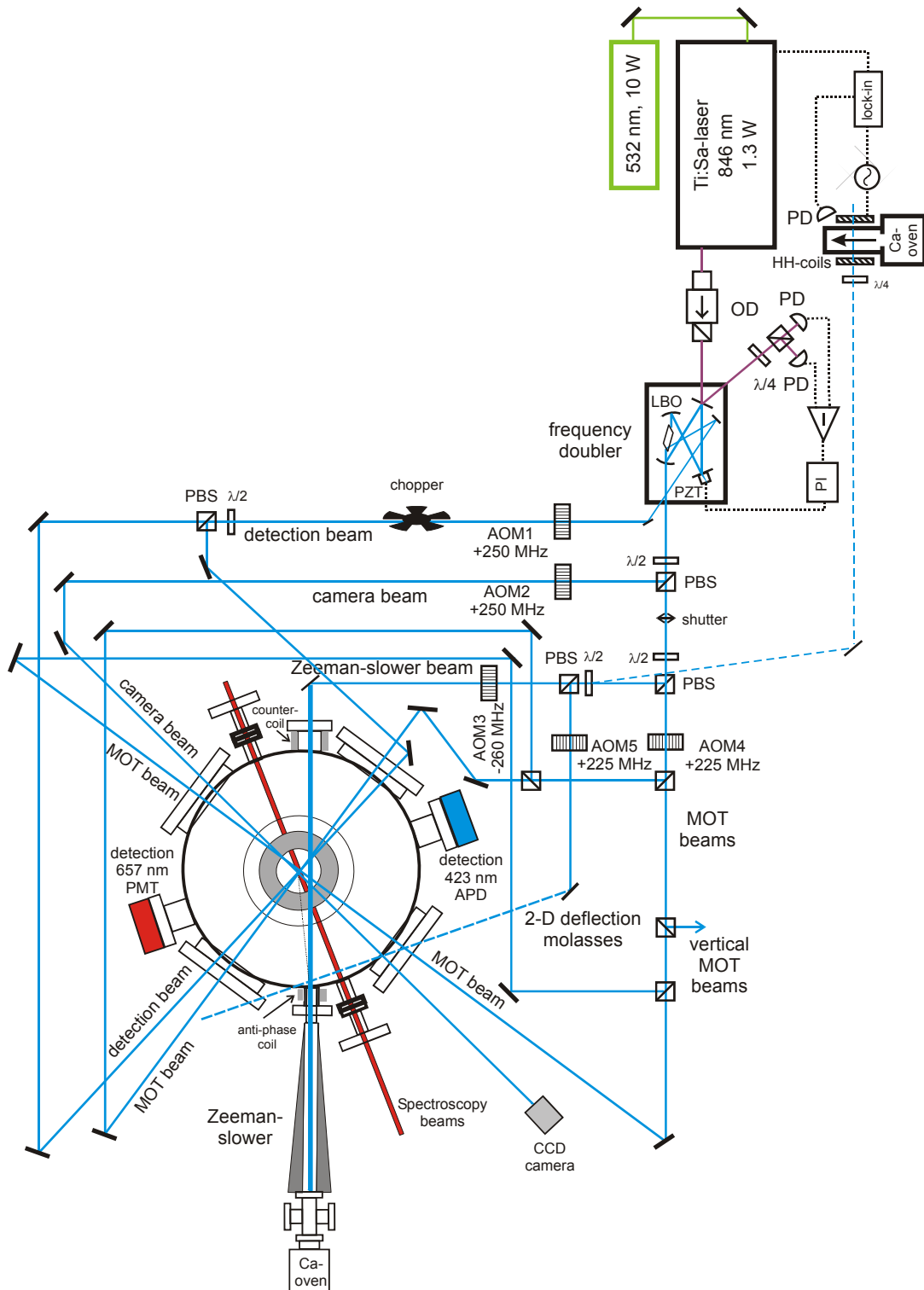


Fig. 2.8 Schematic drawing of the new vacuum chamber. Right upper corner: the laser system for 423 nm. Middle: the vacuum chamber with coils inside. Only the laser beams for 423 nm and the direction of the spectroscopy beams are shown. APD: avalanche photo diode, PMT: photo multiplier tube, AOM: acousto-optical modulator, PBS: polarizing beam splitter, $\lambda/2$: half-wave plate.

The Zeeman slower has a length of 38 cm. A current $I_{sl} = 9.8$ A is flowing through the main coil and $I_{gs} = 12.8$ A through the anti-phase coil (5 x 11 windings) resulting in the maximal magnetic field of $B_{max} = 0.1$ T. The magnetic field created by the anti-phase coil amounts to $B = 0.04$ T. The atoms are decelerated from the initial velocity of 600 m/s to a velocity of 40 m/s. Assuming constant deceleration, a deceleration of $5 \cdot 10^5$ m/s² is acting on the atoms. Both coils are made of capton coated copper wires, an additional water cooling is applied to remove the heat.

After the implementation of the setup, difficulties in cooling of the atoms at the intercombination transition were observed. Since the quench cooling is very sensitive to the external magnetic field, the setup was again inspected. We found out that the anti-phase coil created a magnetic field gradient of 5 μ T/cm. Thus, an additional counter coil was designed in order to compensate this gradient. It is mounted opposite to the anti-phase coil, has 42 windings (7 x 6 layers) and is operated at 13 A. After this measure the quench cooling was working more reliable.

After the slow atoms leave the Zeeman slower, they are further cooled and deflected to the trap region by a two-dimensional optical molasses. In an optical molasses the atoms are only cooled in the direction along the laser beam. Due to the geometry of the vacuum chamber the atoms are deflected by 15°. The molasses laser beams are red detuned by 35 MHz from the atomic resonance. The waist radius of the beams amounts to 5 mm, the power of the beams is 20 mW and 5 mW.

The atoms are trapped in the MOT formed by six independent, pairwise counter-propagating, mutually perpendicular, and circular-polarized ($\sigma^+ - \sigma^-$ configuration) beams. The beams have a waist radius of 10 mm and power of up to 4.5 mW depending on the application. The lifetime of the blue MOT exceeds three seconds because there are no collisions with the hot atoms from the atomic beams and due to a better pressure in the new chamber. The quadrupole field for the MOT stems from water-cooled coils (7 x 6 windings) in anti-Helmholtz configuration, which are placed inside the vacuum chamber to avoid eddy currents. This enables rapid switching of the magnetic field within 200 μ s, which is important for the cooling on the intercombination line as well as for the spectroscopy. The anti-Helmholtz coils have a measured gradient of 0.15 mT \cdot cm⁻¹ per Ampere for the strong axis. The loading rate in the MOT is higher when the magnetic field gradient is low. Thus, one would like to operate the MOT at lower gradients in order to get maximum number of atoms. On the other hand, the atomic cloud gets bigger with lower gradients. This becomes a disadvantage because a bigger cloud leads to more fluctuations for example during the spectroscopy, when the atoms are excited by a resonant beam with a finite size. Hence, the magnetic field gradient is a trade-off and has to be adjusted for different applications. In case of optimizing the setup for running at high cycle frequencies, a current of 30 A is sent through the coils leading to a gradient of 4.5 mT/cm. For the cooling on the intercombination line, the gradient must be reduced. Otherwise the atoms will run out of resonance due to the Zeeman shift if the magnetic field gradient is too big. During this step the current is reduced to 1 A corresponding to a gradient of 0.15 mT/cm. As it was mentioned above, the cooling on the intercombination line is very sensitive to the external magnetic fields. Thus, three pairs of compensation coils were installed outside the vacuum chamber. The compensation magnetic field is optimized by minimizing the Zeeman splitting due to the cross-over effect and should be checked every month.

The homogeneous magnetic field needed for the spectroscopy is generated by an additional pair of coils in Helmholtz configuration. Each coil has 2 x 2 windings. The coils are wound around the quadrupole coils. Since only a current of 5 A is sent

through, no water cooling is applied. The following table gives an overview about the coils used in the setup.

coil	current (A)	
Zeeman slower	9.8	$B_{max} = 0.1$ T
anti-phase coil	12.8	$B = 0.04$ T
counter coil	13	$\Delta B_r = 5$ μ T/cm
quadrupole coils	30 ... 40	$\Delta B/(\Delta I \Delta r) = 0.15$ mT/(A·cm)
Helmholtz-coils	5	$\Delta B/\Delta I = 0.2$ mT/A
compensation coils (in all three space dimensions)	x: 0.79 y: 1.215 z: 0.915	$\Delta B/\Delta I = 0.64$ μ T/A

Table 2.1 Properties of coils used in the experimental setup

2.3.4. Optimization of the cooling cycle

The new setup was optimized to get a maximum number of ultracold atoms in a possible short time. First, the loading rate into the blue MOT was studied. Fig. 2.9 shows the number of atoms loaded into the blue MOT as a function of the loading time for two different quadrupole field gradients. The power in a single MOT beam amounted to 4.5 mW corresponding to a saturation parameter of 0.05. The loading rate was measured to be $1.8 \cdot 10^9$ atoms/s for the field gradient of 6 mT/cm and $1.2 \cdot 10^9$ atoms/s for the gradient of 9 mT/cm. The loading rate is inversely proportional to the quadrupole field gradient because at lower gradients more atoms are within the region, where their Zeeman shift doesn't exceed the value that allows the trapping.

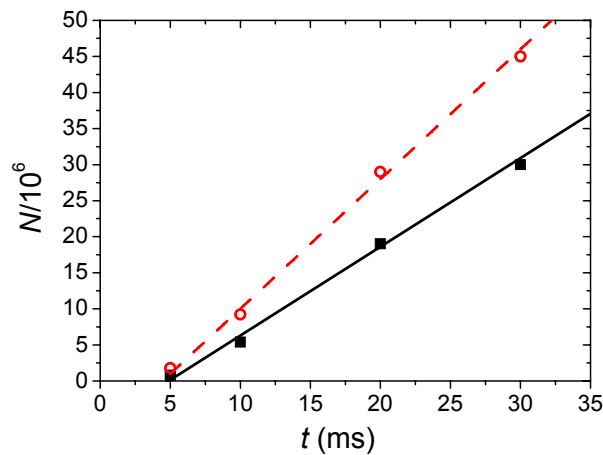


Fig. 2.9 The number of atoms loaded into the blue MOT as a function of the loading time t for different quadrupole field gradients (circles: 6 mT/cm, squares: 9 mT/cm). The loading rate amounts to $1.8 \cdot 10^9$ atoms/s and $1.2 \cdot 10^9$ atoms/s respectively. The power in the MOT beam was 4.5 mW.

The cold calcium atoms at a temperature of 1.2 mK are further cooled on the intercombination line (657 nm). During this second cooling stage the quench laser at 453 nm is additionally applied. The quench laser is realized as a retro-reflected wave in a two dimensional configuration in order to reduce the power imbalance and the beam divergence effects due to the multiple passage through the windows compared to a three dimensional configuration.

The optimal cycle consists now of 30 ms cooling on the broad transition followed by 20 ms cooling on the intercombination line. Up to 10^7 ultracold atoms at a temperature

of 15 μK are trapped in a MOT with $\sigma_{x,\text{rms}} = 0.5$ mm and $\sigma_{y,\text{rms}} = 0.3$ mm. Densities up to $2 \cdot 10^{10} \text{ cm}^{-3}$ are achieved. The loading rate was improved by a factor of six compared to the previous used setup.

In the following, the relevant beam parameters for the cooling are listed:

beam	$\Delta\nu$ (MHz)	power (mW)	w_r^1 (mm)
Zeeman slower	-520	50	
molasses	-35	20 (5)	5
MOT (423 nm)	-35	1 ... 4.5	10
camera	0	0.025	3.7
detection	-8	20	2.5
MOT (657 nm)			
cooling comb width:	1.2	5.8 (hor.)	2.5
detuning	0.2	11.5 (vert.)	2.5
spectroscopy 1	0	13	1.85
spectroscopy 2	0	10.2	1.64
quench beam (453 nm)		70	4

Table 2.2 Relevant parameters for the cooling of calcium atoms

The laser light at 423 nm is generated by frequency doubling light from a titanium-sapphire laser in an external build-up cavity and described in detail in [deg04a]. In total, a power of more than 500 mW is available.

Up to 200 mW of the laser light at 453 nm is delivered by a commercial MOPA system (*Toptica, TA-SHG-110*). The laser is stabilized by means of the offset lock technique to a tunable cavity [deg04a].

¹ The waist of a laser beam is defined as a radius, where its intensity drops to $1/e^2$.

3. Highly stable laser source for atom interferometry

Highly stable and spectrally narrow lasers are necessary for atom interferometer of the Ramsey-Bordé type because the fluctuations of the laser phase between the pulses add directly to the phase of the interferometric signal. In a particular application of an atom interferometer as an optical frequency standard, lasers also serve as local oscillators where they deliver the short-term stability between interrogations of the atomic transition. When the laser frequency is locked to the atomic transition the information about its evolution can be only collected during the interrogation time. During the preparation time of the atomic ensemble no information about the laser frequency can be obtained. This leads to a degradation of the frequency stability of an frequency standard due to the aliasing effect at the Fourier frequencies of the cycle frequency. This so-called Dick effect is treated in detail in the subsection 4.4. There it will be shown that for achieving the ultimate stability given by the quantum projection noise it is essential to reduce the spectral density of the laser's frequency noise both in the low-frequency and in the high-frequency range.

First a short overview about the characterisation of the frequency noise is given in subsection 3.1.

In subsection 3.2 the laser setup and the frequency stabilisation to a high-finesse cavity by means of the Pound-Drever-Hall technique are introduced.

In subsection 3.3 a novel vibration insensitive reference cavity, which allows to reduce the frequency noise in the low frequency range, is described.

The suppression of the high-frequency noise is treated in subsection 3.4.

The stability of the laser system is characterised in subsection 3.5.

3.1. Characterization of frequency noise

To characterize the properties of a laser, the quantities are needed, which give information about the stability of the frequency and its time development. It is common to use the spectral density of frequency fluctuations in the frequency domain and the Allan standard deviation in the time domain to describe the frequency stability of a laser. In precision spectroscopy however the term of linewidth is of interest since it determines the resolution of the spectrometer.

The frequency fluctuations are often characterised with respect to the nominal oscillator frequency ν_0 . The normalized frequency fluctuation $y(t)$ is defined in [rut78] as

$$y(t) = \frac{\nu(t) - \nu_0}{\nu_0} = \frac{\Delta\nu}{\nu_0}, \quad (3.1)$$

where $\nu(t)$ is the instantaneous frequency.

The spectral density of frequency fluctuations is given

$$S_\nu(f) = S_y(f) \nu_0^2, \quad (3.2)$$

where $S_y(f)$ gives the fluctuations of the normalised frequency at different Fourier frequencies. It has a dimension of Hz^2/Hz meaning that the fluctuations are normalised

in 1 Hz bandwidth.

The following equation gives the correlation between the spectral density of frequency and of phase fluctuations $S_\varphi(f)$

$$S_\nu(f) = f^2 S_\varphi(f). \quad (3.3)$$

Often the spectral density of frequency fluctuations can be approximated by the following power law

$$S_\nu(f) = \sum_{\alpha=-2}^{\alpha=2} h_\alpha f^\alpha, \quad (3.4)$$

where the exponent α characterises the kind of the noise process. The different noise processes are summarised below

α	<i>noise process</i>
-2	random walk frequency noise
-1	flicker frequency noise
0	white frequency noise
1	flicker phase noise
2	white phase noise

The Allan standard deviation describes the time evolution of the frequency stability of an oscillator. It was already used in 2.2.2 and is treated here in more detail. The Allan standard deviation of the normalised frequency fluctuations is defined [rut78] as

$$\sigma_y^2(\tau) = \frac{1}{2(N-1)} \sum_{k=1}^{N-1} \left(\overline{y_{k+1}} - \overline{y_k} \right)^2. \quad (3.5)$$

It gives the variance of the measured normalised average frequency differences between consecutive points as a function of the averaging time τ . The advantage of the Allan standard deviation compared to the classical standard deviation is the fact that it is convergent for most noise types (and also for the drift). The Allan standard deviation can be calculated for the measured spectral density as [rut78]

$$\sigma_y^2(\tau) = \int_0^\infty S_\nu(f) \frac{2 \sin^4(\pi f \tau)}{(\pi f \tau)^2} df. \quad (3.6)$$

It can also be written as a power law

$$\sigma_y^2(\tau) \propto \tau^\mu, \quad (3.7)$$

where the exponent μ is given by

$$\mu = \begin{cases} -\alpha - 1 & \text{for } \alpha \leq 1 \\ -2 & \text{for } \alpha > 1 \end{cases}. \quad (3.8)$$

The behaviour of the spectral density of frequency fluctuation for different noise types and the corresponding course of the Allan standard deviation are shown in Fig. 3.1.

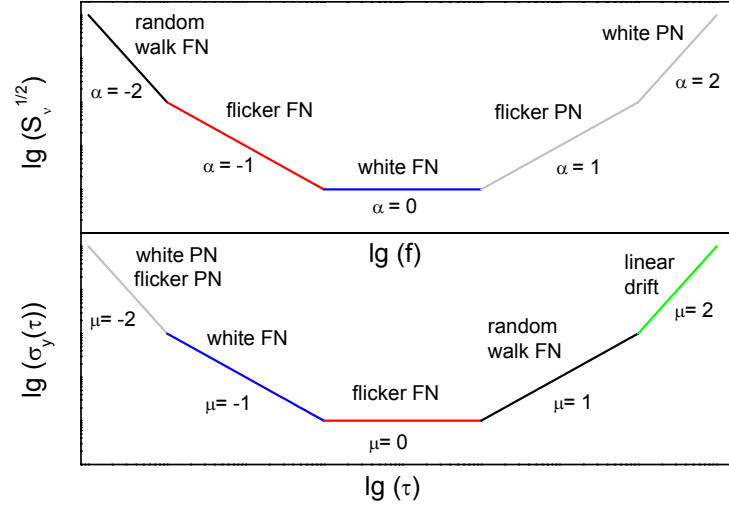


Fig. 3.1 The spectral density of frequency fluctuations (upper graph) and the Allan standard deviation (lower graph) for different noise types. (FN: frequency noise, PN: phase noise)

For some noise processes often considered in this work the conversions factors are summarised below

noise process (α)	$S_v(f) = a v_0^2 \sigma_y^2(\tau)$, $a =$	$\sigma_y^2(\tau) = b S_\varphi(f)$, $b =$
white frequency (0)	2τ	$\frac{f^2}{2\tau v_0^2}$
flicker frequency (-1)	$\frac{1}{2 \ln 2 f}$	$\frac{2 \ln 2 f^3}{v_0^2}$

For white frequency noise the optical power spectrum of a laser has a Lorentzian form and the relation between the spectral density of the frequency fluctuations and the linewidth is given as [ell82]

$$\Delta\nu = \pi S_v. \quad (3.9)$$

The term of the laser linewidth makes only sense if the measurement time is given. The fluctuations of the laser frequency on the short-time scale average down with longer measurement time while the influence of the long-term stability (i.e. drift) rises with increasing time. In this chapter, the term of the fast laser linewidth is used, which describes the laser linewidth for short measurement times.

3.2. Laser setup

To interrogate the calcium intercombination line at 657 nm, two similar but independent laser systems (called Master1 and Master2) are available. They were built by H. Stoehr within the scope of his Ph.D. work [sto04]. With this setup a laser linewidth of 1 Hz has been demonstrated [sto06]. One of those systems (Master2) was modified in the scope of the present work. The properties of the laser systems are described in detail in [sto04]. Here, a short summary follows.

3.2.1. Extended cavity diode laser

Diode lasers are widely used in a variety of fields of the modern experimental physics. Their advantages are wide tuning range, compactness, reliability, low cost, and low power consumption. Due to their structure and size they exhibit however typical free running linewidths in the Megahertz range. The laser linewidth can be reduced to some hundreds kilohertz by optical feedback using extended cavity lasers. For further reduction of the linewidth of extended cavity diode lasers (ECDL) the laser frequency is locked to eigenmodes of a high stable reference cavity using an active servo system.

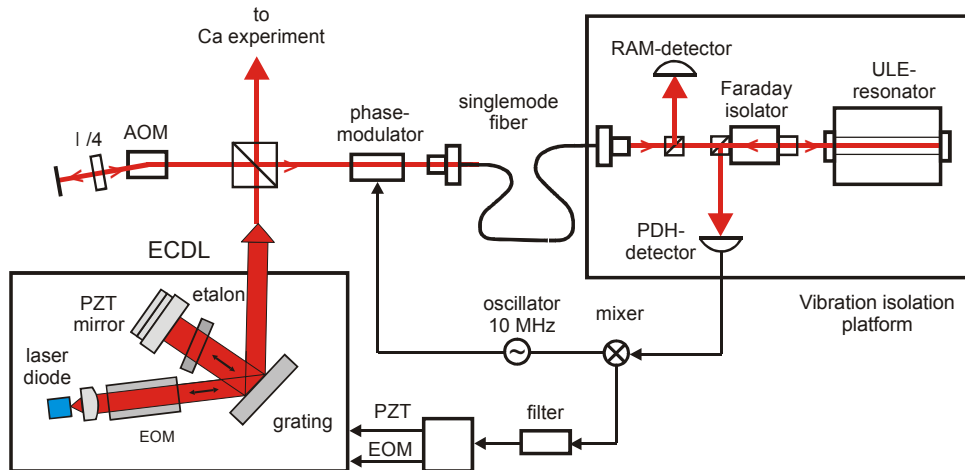


Fig. 3.2 Setup of the extended cavity diode laser in Littman configuration (left) and of the Pound-Drever-Hall stabilisation scheme (right).

The schematic setup of the ECDL is shown in Fig. 3.2. The ECDL is built in the Littman configuration, i.e. the antireflection-coated end surface of the laser diode and the mirror which reflects the -1. diffraction order of the grating (1400 lines/mm) form the laser resonator. The resonator length amounts to 13 cm. The zeroth order provides the output beam. An intra-cavity LiNbO_3 electro-optical modulator (EOM) is used for fast and the PZT-actuator for slow frequency control.

3.2.2. Frequency stabilization to a high-finesse cavity

One of most common techniques to improve the frequency stability of a laser is the Pound-Drever-Hall stabilization scheme [dre83]. The general principle is indicated in Fig. 3.2. The laser light is phase modulated by an electro-optical modulator and sent to a reference resonator made of ultra-low expansion glass (ULE). The modulation frequency is 10 MHz and 16 MHz for Master1 and Master2 respectively, the modulation index $M = 0.6$ creates a spectrum consisting of a carrier and two side bands. Since the side bands are far away from the carrier and the line width of the reference cavity is about 19 kHz the side bands are reflected by the cavity. When the laser frequency is close to an eigenmode of the cavity the carrier is coupled into the cavity. Then a small part of a standing wave inside the cavity leaks back through the first mirror, which is not perfectly reflecting. This leakage beam carries the information about the laser frequency and the signal consisting of the sum of the beats with the reflected side bands is recorded on the Pound-Drever-Hall (PDH) detector. In the resonant case both beat signals have the same amplitude but different signs because the side bands have a phase shift of 90° . Thus, the signal mixed with the modulation frequency interfere destructively. If the laser frequency is slightly detuned from the resonance of the cavity, the reflected beam causes an asymmetry in the signal due to a phase shift. Hence, the

amplitude of the signal contains information about the instantaneous laser frequency. The mixer generates a dispersive error signal, which is sent to the servo electronics and feed back to the laser.

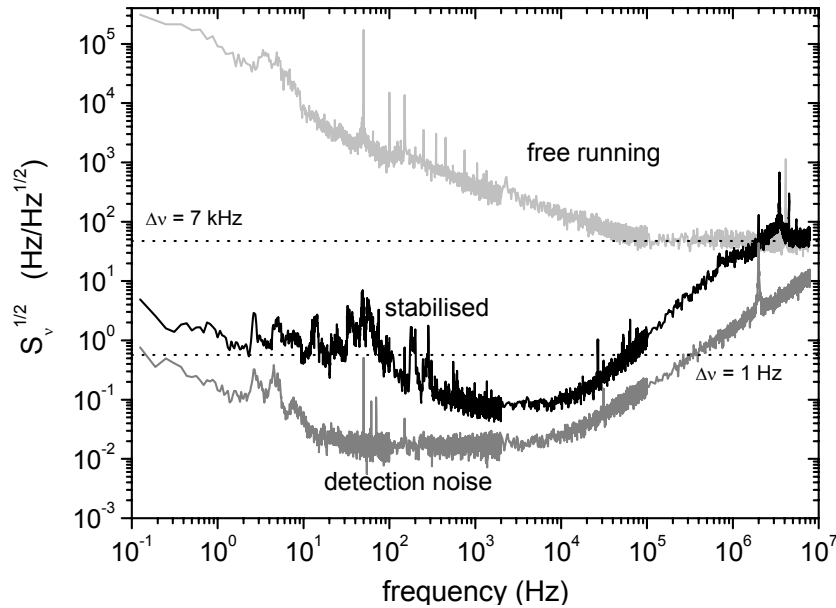


Fig. 3.3 Spectrum of frequency fluctuations of Master1 (taken from [sto04]).

Fig. 3.3 shows the spectrum of frequency fluctuations of Master1 (taken from [sto04]). The grey curve depicts the frequency fluctuations of the free running laser corresponding to a fast line width of approx. 7 kHz. By means of the Pound-Drever-Hall stabilisation the frequency fluctuations could be significantly reduced (black line). The servo electronic is in principle able to reduce the frequency noise to below $0.1 \text{ Hz/Hz}^{1/2}$ as it was determined from the measurement of the detection noise. The increase of the frequency fluctuations at higher frequencies is due to the limitation of the gain of the servo loop, which decreases towards at the unity-gain frequency (about 3 MHz in this case). The increase of frequency fluctuations at frequencies below one kilohertz is caused by fluctuations of the optical length of the reference cavity caused by acoustic and seismic vibrations acting on the cavity. The considerations about the Dick effect (see 4.4) indicate that frequency fluctuations in both ranges must be suppressed in order to achieve a high frequency stability of a frequency standard.

3.2.3. Self-heterodyne technique

In order to characterise the current frequency noise of the laser systems and to show improvements obtained during this work, the delayed self-heterodyne technique was used. The idea of this technique is to convert frequency fluctuations of the laser into variations of light intensity in a Mach-Zehnder interferometer (Fig. 3.4, left-hand figure). The laser beam is split on a beam splitter, one part is frequency shifted by means of an acousto-optical modulator, sent through a fibre and overlapped with the first part on a photodiode. The power spectrum of the fluctuations of the photodiode is recorded with a spectrum analyser (Fig. 3.4, right-hand figure). The advantage of this technique is that no reference system is needed to characterised a laser.

The measured spectrum consists of a narrow carrier peak and a broadened Lorentzian pedestal. Since the delay time in the fibre ($t_d = 0.4 \mu\text{s}$) is shorter than the coherence time of the laser, the phases of both electric fields, which interfere on the detector, are still partially correlated. Thus, the pedestal shows an oscillation pattern with the period $1/t_d$.

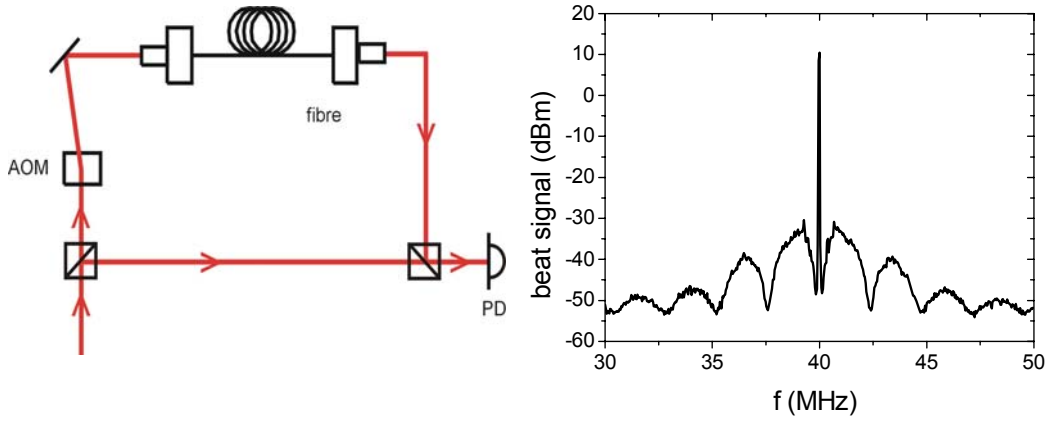


Fig. 3.4 The principle of delayed self-heterodyne technique (left-hand figure) and a power spectrum of fluctuations of the photodiode current (right-hand figure). The resolution bandwidth of the spectrum analyzer amounted to 10 kHz.

The spectrum can be described in the case of white frequency noise $S_{\nu 0}$ as the following sum [ric86]

$$S(\nu) = e^{at_d} \delta(2\pi\nu) + \frac{2e^{at_d}}{a^2 + (2\pi\nu)^2} (a \cos(2\pi\nu t_d) + 2\pi\nu \sin(2\pi\nu t_d)) - \frac{2a}{a^2 + (2\pi\nu)^2} - \frac{2e^{at_d}}{2\pi\nu} \sin(2\pi\nu t_d) \quad (3.10)$$

with t_d the delay time in the fibre and $a = -2\pi^2 S_{\nu 0}$. For short delay times (i.e. $|a| < 1/t_d < 2\pi\nu$) and high frequencies (i.e. far from the measured beat frequency) $S_{\nu 0}$ can be determined from the ratio between power in the carrier P^c (the first term in (3.10)) and in the pedestal $S(\nu)$ (the remaining terms in (3.10))

$$\frac{S(\nu)}{P^c} = e^{2\pi^2 S_{\nu 0} t_d} 2S_{\nu 0} \frac{\sin^2(\pi\nu t_d)}{\nu^2}. \quad (3.11)$$

If the $S_{\nu 0}$ is known the fast linewidth of the laser can be calculated using (3.9).

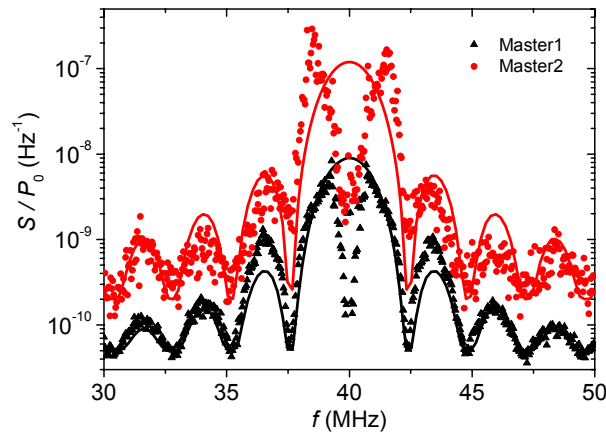


Fig. 3.5 The spectrum of relative fluctuations of the photodiode current (symbols) for Master1 and Master2 and fits (lines) according to (3.11). From the fits a fast linewidth of 8 kHz for Master1 and 90 kHz for Master2 was determined.

First the delayed self-heterodyne measurements were performed with existing laser systems Master1 and Master2. Fig. 3.5 shows the power spectrum of the photodiode

current for Master1 and Master2 (symbols). The lines depicts the fits according to (3.11). From the measurements a fast linewidth of 8 kHz for Master1 and 90 kHz for Master2 was determined. That means that Master2 has a significant higher frequency noise in high-frequency range (above 2 MHz) than Master1. This behaviour could not be improved by carefully alignment of the ECDL. Since both lasers have identical components, I assume that the difference comes from unique properties of single laser diode and its interaction with other optical components. In subsection 3.4 the way to reduce the frequency fluctuations in high-frequency range is shown.

3.3. Vibration insensitive reference cavity

The results presented here were originally published in Applied Physics B 83, 531-536 (2006). In the following subsection (3.3.1-3.3.5,3.3.7) the passages of the paper are cited.

To realize a highly stable narrow linewidth laser an active frequency stabilization to the eigenmodes of a stable high-finesse reference cavity is used. Then the stability of the locked laser is determined by the stability of the optical length of the reference cavity. The most severe fluctuations of the length are caused by low frequency (below 100 Hz) seismic and acoustic accelerations resulting in quasi-static deformations of the cavity. These vibrations couple through the mounting to the cavity and lead to forces, which deform the cavity and change its length.

In the widely used design where the reference cavity is supported from below this coupling typically leads to sensitivities to accelerations in the range of 100 kHz/(m/s²) [you99]. Then a sophisticated insulation of vibrations down to the range of 10⁻⁵ m/s² is needed to achieve linewidths of one Hertz. In a different approach the cavity is designed in a such way that it already shows a low sensitivity to accelerations [not96,not05]. Here we introduce a novel cavity mounting configuration [ros04], which allowed us to reduce the vibration sensitivity by two orders of magnitude in the vertical and one order of magnitude in the horizontal direction.

3.3.1. Stability of the reference cavity

General principles

We first introduce a model, which describes acceleration-induced deformations of the cavity. Depending on the frequency f of the vibrations compared to the mechanical eigenfrequencies f_i of the system (for 10 cm sized cavities in the range of kHz), two regimes can be distinguished. In the high frequency regime $f > f_i$ the external vibrations excite the eigenmodes and the response can be obtained by a decomposition of the individual modes and the response of the mode to the applied forces. In the low frequency limit $f \ll f_i$ that is of primary interest here, the forces that are coupled to the solid accelerate the solid as a whole and lead to quasi-static deformation of the solid under the external force.

For the small forces acting here a linear dependence between the stress tensor σ_{ij} and the strain ϵ_{kl} can be assumed given by Hooke's law [tim51]

$$\sigma_{ij} = \sum_{kl} c_{ijkl} \epsilon_{kl} , \quad (3.12)$$

with the strain tensor

$$\varepsilon_{ij} = \frac{1}{2} \left(\frac{\partial u_i}{\partial x_j} + \frac{\partial u_j}{\partial x_i} \right), \quad (3.13)$$

where u_i is the displacement vector along the axis i ($i = x, y, z$). Thus the changes of the dimension d of the cavity depend linearly on the forces

$$\Delta d = \sum \alpha_k F_k, \quad (3.14)$$

with α_k the respective proportional constant.

From symmetry considerations some initial hints for an optimized mount can be obtained. If the optical axis is invariant under a symmetry operation U of the body, i.e. $U(L) = L$ but if the forces reverse under the same symmetry operation, i.e. $U(\mathbf{F}_i) = -\mathbf{F}_i$ then from Hooke's law all deformations reverse sign under the symmetry operation $u(U(\mathbf{r})) = -u(\mathbf{r})$, therefore $U(L) = -L$. But as L is invariant under the symmetry operation this implies $\partial L = 0$. Thus, if the optical axis is included in the plane of symmetry and if all forces share the same symmetry with respect to that plane acceleration-induced changes of the length are completely suppressed. For instance for a horizontal mount of the cavity all support points have to lie in the symmetry plane, or if that is not possible, they have to act symmetrically to that plane. In the latter case, however, the requirement of symmetry in the forces is very difficult to obtain, as this requires that the elastic constants of symmetric supports are also exactly equal.

To illustrate the principles of an optimized mounting we first treat an example of a cuboid-shaped cavity of dimensions d_x, d_y, d_z . Only forces that accelerate the cavity are considered which cause quasi-static elastic deformations of the cavity. In the following we first assume that the cavity is held in a plane and therefore we do not need to take into account the bending which would appear if the cavity is held in discrete points. If the cavity is held asymmetrically from below (Fig. 3.6, a) an acceleration a_y along the y -direction leads to compression Δd_y in the same direction [tim51]

$$\Delta d_y = \frac{F d_y}{EA} = \frac{\rho d_y^2}{E} a_y, \quad (3.15)$$

where $F = \rho d_x d_y d_z a_y$ is the accelerating force, ρ the density, E Young's modulus, and A the cross section perpendicular to the acceleration.

The compression along the direction of acceleration leads to an expansion in the perpendicular direction of

$$\Delta d_z = \nu \frac{\rho d_y d_z}{E} a_y, \quad (3.16)$$

where ν denotes Poisson's ratio. In the case b) when the cavity is fixed at the top the deformations are reversed: the cavity expands in the direction parallel to the acceleration and shortens along the perpendicular axis.

Since the cavity length change reverses its sign depending on the position of the supporting plane in case a) and b) there must be a point where the change amounts to zero. This situation is achieved when the cavity is supported in its symmetry plane (case c). The length changes discussed here are due to vibration-induced accelerations, so they are independent on the orientation of the acceleration \vec{a} with respect to the gravitational acceleration \vec{g} .

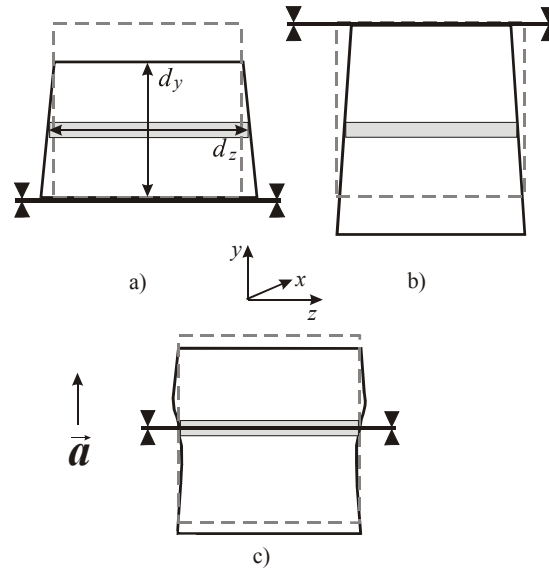


Fig. 3.6 Influence of accelerations on a cuboid for different positions of the supporting plane. The original shape of the cube is indicated by dashed lines. The deformed shape is considered in the accelerated coordinate system.

A support of an optical cavity in the symmetry plane was applied recently for a vertical orientation of the optical axis [not05] which corresponds to Fig. 3.6, c with the axis along the y -direction. Due to the acceleration the upper half of the cavity is compressed while the lower half expands. The expansion of the upper half and the contraction of the lower half along the cavity axis are equal and compensate each other which lead to a reduced vibration sensitivity of $10 \text{ kHz}/(\text{m/s}^2)$ [not05]. In this case the two relative length variations which have to be compensated depend linearly on the length of the cavity (3.15), which makes it more difficult to apply this configuration for longer cavities that are less affected by thermal noise [num04]. To reduce this effect we chose to put the optical axis in a horizontal symmetry plane. In this case, the acceleration-induced length variation along the optical axis i.e. in z -direction is reduced by Poisson's ratio. In addition the relative length change in z -direction does not depend on this length (3.16). Our novel cavity mounting, where the cavity is supported symmetrically on four support points, is shown in Fig. 3.7.

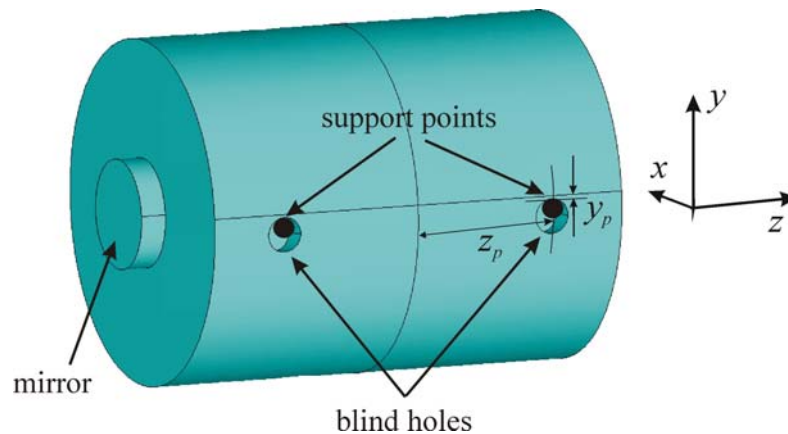


Fig. 3.7 Optimized mounting of the reference resonator.

When the cavity is held in discrete points, in addition to the change of the distance between the centres of the mirrors shown in Fig. 3.6 accelerations also lead to a bending which causes a mirror tilt about the geometrical axis. As the laser frequency is determined by the length L_{opt} of the optical axis, which is characterized as being perpen-

dicular to the mirror surfaces, the mirror tilt leads to a movement of the optical axis and a corresponding length change ΔL_{opt} . For small angles it amounts to [sie86]

$$\Delta L_{opt} = \frac{L\alpha^2(2 + g_1 + g_2)}{1 - g_1g_2}, \quad (3.17)$$

where α is the tilt angle and g_1 and g_2 are the cavity g factors defined as $g_i = 1 - L/R_i$ with R_i the radius of curvature of the mirror. Since $\Delta L_{opt} \propto \alpha^2$ and the tilt angle is in the range of several nrad this effect can be neglected. If, however, the optical axis is not exactly centred in the middle of the mirrors but displaced by an amount Δr then a tilt of the mirror with respect to its centre will directly change the length of the optical axis by $\Delta r\alpha$ which is a more severe effect.

Thus, to minimize the sensitivity to the acceleration the positions of the support points where the length change of the optical path of the cavity and the mirror tilt are minimal needs to be determined. The optimization by finite element analysis is described in the next section.

3.3.2. FEM Simulations

As in practice the spacer is not completely symmetric, the optimum positions of the support cannot be found analytically. Thus, in order to include all effects we performed finite element analysis using a commercial program [ans71].

The cavity spacer and the optically contacted mirrors are made of ultra-low expansion glass (ULE). The spacer has a length of 10 cm and a diameter of 8 cm. The Young's modulus of ULE is $E = 67.6 \cdot 10^9$ Pa, the Poisson's ratio amounts to $\nu = 0.17$ [rat68]. We use a Cartesian coordinate system that has its origin in the centre of the cylinder in such way that the z -axis shows in the direction of the cylinder axis, the y -axis in the vertical direction, and the x -axis in the radial direction of the cylinder (Fig. 3.7). From the FEM calculations the displacement u_z is obtained, which denotes the displacement of a volume element in the direction of the z -axis.

In our previous setup [sto04] the reference cavity was supported at the Airy points (at distances $0.21l$ from the ends) [wil62] from below by four small cylindrical elastomer pieces (Viton) under an angle $\alpha = 35^\circ$ with respect to the vertical direction. We simulated this mounting configuration by setting the boundary condition such that no displacement normal to the surface at the support points was allowed. Since the problem is symmetric with respect to the x - y -plane and the y - z -plane it is sufficient to simulate only a quarter of the cavity. The results of the simulation are shown in Fig. 3.8 in a cut at $x = 0$. In this case the change of the distance between the mirrors under an acceleration of $a_y = 10$ m/s² amounts to $3.7 \cdot 10^{-10}$ m leading to a calculated sensitivity to vertical acceleration of 170 kHz/(m/s²) while the measured sensitivity is 120 kHz/(m/s²) [sto06]. In this configuration the minimal change of length occurs in the lower part of the spacer (indicated by arrows in Fig. 3.8).

In the next step we simulated the symmetrical mounting configuration shown in Fig. 3.7. The deformed shape and the displacement u_z in the z -direction under an upward acceleration of $a_y = 10$ m/s² are shown in Fig. 3.9. Now the change of the distance is minimal between the mirrors, i.e. along the symmetry axis. The bending of the cavity in the middle amounts to approx. 0.3 nm.

In order to find the positions of the supporting points, where the length change between the mirrors and the mirror tilt both are minimized, the coordinates y_p and z_p of

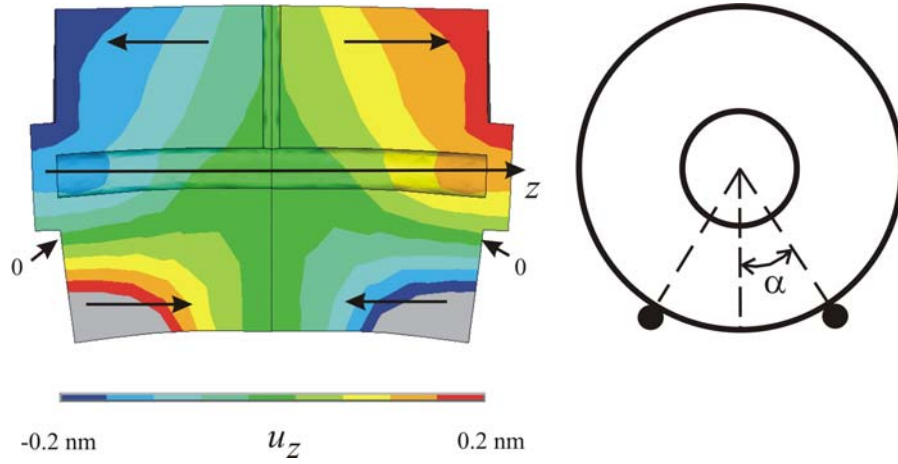


Fig. 3.8 Calculated deformation u_z of a resonator supported from below ($\alpha = 35^\circ$) under an acceleration of $a_y = 10 \text{ m/s}^2$ in the y -direction. The deformation of the cavity was magnified by a factor of 10^7 to make it visible. The long arrows show the direction of the displacement with respect to the z -axis and the short arrows indicate the region where $u_z \approx 0$.

the support points are varied. We assumed a support on the top of a hole with diameter 8 mm and depth 10 mm (cf. Fig. 3.7). For the calculation, the support was described by setting the boundary condition $u_y = 0$ inside a circle of 2 mm diameter with its centre located $x_p = 5 \text{ mm}$ inside the blind hole on its top. Due to the symmetry only one quarter of the cavity was calculated using symmetric boundary conditions at the planes $x = 0$ and $z = 0$.

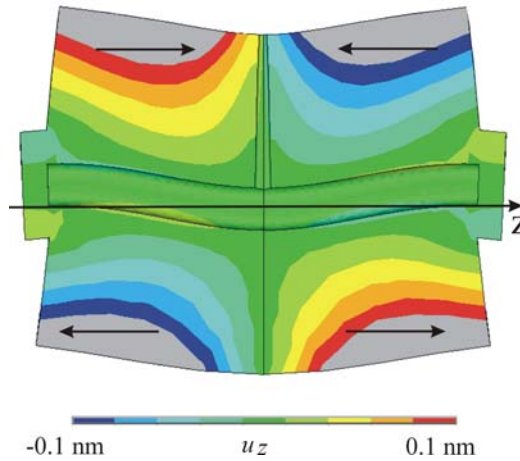


Fig. 3.9 Calculated deformation of a resonator supported symmetrically in the horizontal plane. The displacement u_z is shown under an acceleration of $a_y = 10 \text{ m/s}^2$ in the y -direction. The bending of the cavity was magnified by a factor of 10^7 to make it easily visible. The arrows show the direction of the displacement with respect to the z -axis.

The results for different positions z_p and y_p are shown in Fig. 3.10. The vertical position y_p of the supporting points determines the mass distribution and therefore mostly affects change in the length between the mirrors (Fig. 3.10, a) with minor influence on the tilt (Fig. 3.10, b). The axial position z_p of the supporting points influences the acceleration-induced bending of the cavity and thus the tilt of the mirrors with respect to the geometrical axis (Fig. 3.10, d). In this case the influence on the length is much smaller as in the variation of y_p . Thus, by optimization both the length change of the cavity and the mirror tilt can be zeroed at the same time at the optimal positions of the supporting points of $y_p = -0.9 \text{ mm}$, $z_p = 35 \text{ mm}$.

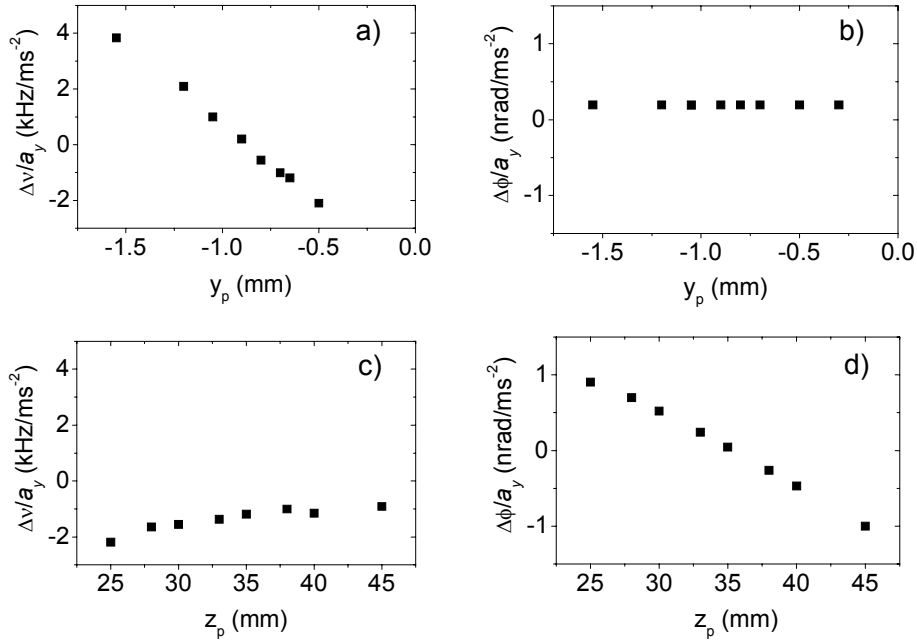


Fig. 3.10 Calculated acceleration sensitivity due to the length change (a and c) and the mirror tilt (b and d) as a function of position of supporting points. During the variation of z_p (y_p) the other coordinate y_p (z_p) was held at $y_p = -0.9$ mm and $z_p = 35$ mm.

The influence of tolerances of the mechanical processing can be obtained from the same figure. For 1 mm deviation of y_p from the optimum position, the acceleration sensitivity amounts to $k_y = 5.7$ kHz/(m/s²). The same deviation in z_p leads to a tilt of a few nrad. In combination with an deviation of the optical axis from the mirror center by 1 mm this tilt would lead to a sensitivity of $k_y = 1.8$ kHz/(m/s²). The sensitivity of the complete cavity to vibrations via the reaction forces on the four support points is given by (3.14). With the optimal design each coefficient α_k is equal to zero by virtue of the cavity symmetry. Thus the sensitivity remains zero even when the forces are not balanced.

Up to now we discussed the sensitivity k_y to vertical vibrations since in the laboratory vertical vibrations are more pronounced than horizontal ones. To also render the mounting insensitive to horizontal vibrations, the corresponding forces acting on the supporting points need to be perfectly balanced. In practice this is difficult to achieve since the symmetry of the reaction forces depends on mechanical parameters of the mounting like its elasticity and spring constant. We performed simulations to find out how sensitive our mounting is to force imbalance. For this purpose we simulated an imbalance of 100 % i.e. the cavity is supported on one supporting point. For this case we obtain a sensitivity to vibrations along z of $k_z = 320$ kHz/(m/s²). This value was used to estimate the residual imbalance of the mounting from the measured sensitivity to the horizontal vibration.

3.3.3. Uncertainty of FEM simulations

In this subsection the uncertainties of the numerical calculations and their origin are discussed. The errors can be caused by the calculation itself as well as by uncertainties of the material constants involved.

One of the important parameters in the FEM simulations is the mesh size, which is the size of the finite elements. The mesh size should be as small as possible in order to

ensure good accuracy. To evaluate the influence of the mesh size, the calculations were performed for two different sizes (small size and big size corresponding to 24 000 and 12 000 finite elements within the volume of the cavity respectively). The coordinate y_p of the supporting points was varied while the coordinate z_p was fixed to $z_p = 35$ mm. Fig. 3.11 shows the calculated acceleration sensitivity as a function of the position of the supporting points for the different mesh sizes. Choosing the mesh size too big leads to an error of 0.25 mm in y_p yielding in a residual acceleration sensitivity of 1.5 kHz/(m/s²).

The numerical uncertainty of the FEM simulations was estimated to 1 kHz/(m/s²) by comparing results for different meshing of the cavity and from the scatter of the results of Fig. 3.10, which amounts to 0.1 kHz/(m/s²). The uncertainties of the values of Young's modulus and Poisson's ratio as well as their dependence on the temperature [rat68] lead to uncertainties in the simulations. Assuming an uncertainty of 2 % in Young's modulus and Poisson's ratio we calculated an uncertainty of 0.04 kHz/(m/s²) and 0.08 kHz/(m/s²), respectively, for the optimal position of the supporting points. In addition also the mechanical tolerances of the cavity spacer should be taken into account as the cavity is not a perfect body as it is assumed in the simulations. For instance the parallelism of the end faces of the cylinder is specified by being less than 1.7 mrad. Further uncertainties up to 1 mm in the centring of the mirror can occur by wringing the mirrors to the spacer. Thus, we assume a total uncertainty of the simulation of 2 kHz/(m/s²).

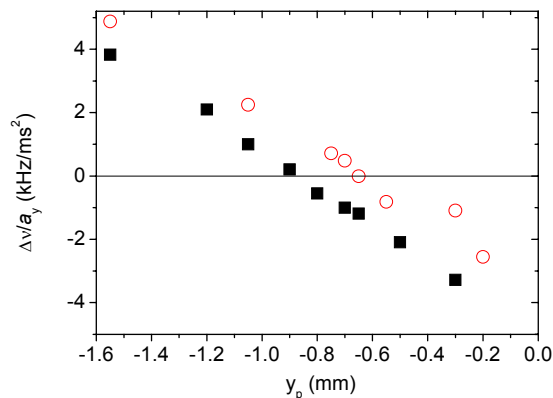


Fig. 3.11 Influence of the mesh size (squares: big size (12 000 finite elements) and circles: small size (24 000 finite elements)) on the optimal position of the supporting points y_p . The error in the numerical calculations corresponds to an acceleration sensitivity of 1.5 kHz/(m/s²).

During the simulations it turned out that the boundary conditions specially have an enormous influence on the results. In the experiment, the cavity is resting on four elastic viton cylinders. Thus the precise size of the contact area is not known. We performed simulations for two extreme cases: taking first the whole area of the upper half of the inner surface of the blind hole (squares in Fig. 3.12) and then a small 2 mm diameter area in the inner surface (circles in Fig. 3.12). The calculated acceleration sensitivity differs by 30 kHz/(m/s²).

Since the acceleration sensitivity is strongly influenced by the boundary condition of the simulation and the truly experimental conditions can not be precisely described, it is important to have an additional parameter, which can be experimentally adjusted, if the measured acceleration sensitivity is too high. This can be done for example by adding weights to the cavity in order to stress the distribution [not05].

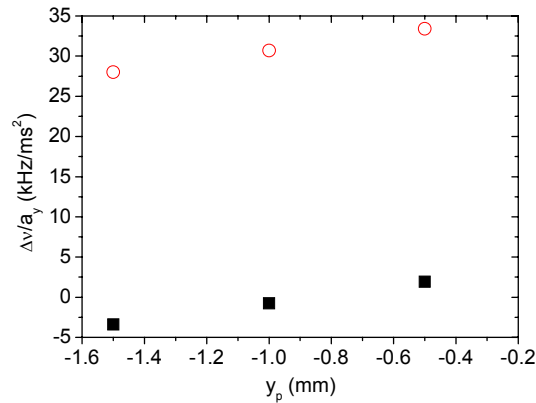


Fig. 3.12 Influence of the boundary condition on the calculated acceleration sensitivity. As the contact area was taken: squares – the whole area of the upper half of the inner surface of the blind hole and circles – an area in the inner surface of 2 mm diameter.

3.3.4. Suspension of the cavity

The cavity was prepared by drilling four blind holes with a diameter of 8 mm and a length of 10 mm at the position determined by the simulations (Fig. 3.13). Since the cavity is supported on four points the support plane is over determined and thus the distribution of the forces would depend sensitively on mechanical tolerances. Thus an elastic support on spring wires is used to compensate the unevenness and to balance the reaction forces. The spring constant of the wire of diameter 0.5 mm amounts to 4.3 N/mm. Viton cylinders of 3 mm diameter and 7 mm length were added to each spring wire to damp the oscillations of frequency 23 Hz. The spring wires were placed centrally in screws, which were installed in the surrounding gold-coated copper cylinder that acts as a heat shield. The setup is installed in a high vacuum chamber ($p < 10^{-6}$ Pa) with an active temperature stabilization.

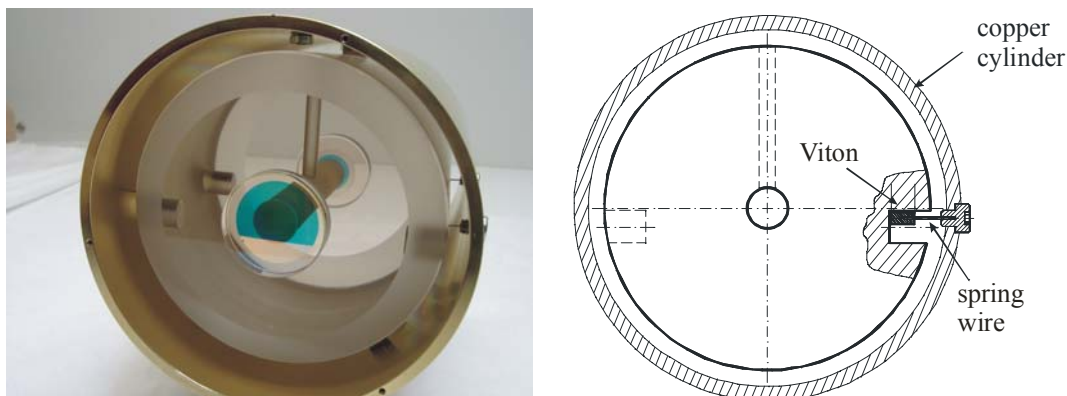


Fig. 3.13 Photo and drawing of the novel mounting configuration.

With this elastic mount the cavity can move with respect to the laser beam. This movement can broaden the laser spectrum due to the Doppler effect. Under a horizontal acceleration of 10^{-5} m/s^2 , which is a typical value in our laboratory, the cavity moves about 0.7 nm within one oscillation. As the amplitude of the oscillation is three orders of magnitude smaller than the laser wavelength of 657 nm the movement will only introduce a phase modulation with modulation index $M \ll 1$. This will only introduce sidebands at the 10^{-6} level but no additional linewidth broadening due to the Doppler shift.

3.3.5. Measurement of the vibration sensitivity

To determine the acceleration-induced frequency change of the cavity, the beat between the laser locked to the cavity and a second independent laser system was analysed. The cavity was placed on a platform hanging on four springs. The vibrations were measured with commercial seismometers: a_y with GS-1 (*GeoSpace Technology*, USA), a_z with L4-C (*Marc Products*, France), and a_x with an accelerometer (*PCB, Piezotronics*, USA). The movement of the platform was manually excited in three directions and the beat frequency and the accelerations of the platform in all three directions were recorded simultaneously. Even if the platform is oscillating mostly in one direction, there are still oscillations in the other two directions, which are one order of magnitude weaker than the major one. To determine the complex transfer coefficient k_i for each direction, the results of the three measurements $l = 1, 2, 3$ had to be separated, taking into account the amplitude as well as the phase of the signals because the accelerations along the three axes need not be in phase depending on the excitation movement.

The amplitude of the frequency variation in measurement l is then given by

$$f_i = \sum_{m=x,y,z} a_{lm} e^{i\varphi_{lm}} k_m, \quad (3.18)$$

where $a_{lm} e^{i\varphi_{lm}}$ are the complex acceleration components of measurement l in the three directions $m = x, y, z$ with amplitude a_{lm} and phase φ_{lm} relative to the observed frequency modulation. The amplitudes and the phases of the accelerations are summarized in the following table.

meas. l	a_{lx} (m/s ²)	a_{ly} (m/s ²)	a_{lz} (m/s ²)	φ_{lx} (rad)	φ_{ly} (rad)	φ_{lz} (rad)	f_l (Hz)
1	0.08	0.004	0.015	5.71	0.23	2.82	0.68
2	0.018	0.3	0.025	1.2	2.85	4.29	0.2
3	0.001	0.001	0.1	2.87	-0.04	0.18	1.32

Table 3.1 Amplitudes and phases of accelerations and beat frequencies for the measurements in three directions.

Combining three measurements along the x , y , and z axis and solving (3.18) we determined the acceleration sensitivity of $k_y = (1.5 \pm 0.3)$ kHz/(m/s²) in the vertical, $k_z = (14.5 \pm 1)$ kHz/(m/s²) in the axial, and $k_x = (11 \pm 0.8)$ kHz/(m/s²) in the radial x direction of the reference cavity. The values given here are the modulus of the complex transfer coefficient.

The coefficients k_x and k_z are in good agreement with the ones determined by tilting the resonator by a small angle β , which is equivalent to an acceleration of $a_x = g\beta$, where g denotes the gravitational acceleration.

The results of the measurements are shown in Fig. 3.14 for the vertical direction. On the left-hand side the acceleration (upper graph) and the corresponding beat frequency (lower graph) are presented in the case of the asymmetrical support where a high vibration sensitivity of $k_y = 120$ kHz/(m/s²) was determined. The analogous results for our new mounting on the right-hand side of Fig. 3.14 show an improvement of two orders of magnitude for the vertical direction. The measured acceleration sensitivity of $k_y = 1.5$ kHz/(m/s²) in vertical direction is in agreement with the simulation

$(0 \pm 2) \text{ kHz}/(\text{m}/\text{s}^2)$.

Since the vibration sensitivities for both horizontal directions (axial z and radial x) are an order of magnitude higher than for the vertical direction, we have analyzed our mounting in respect thereof. The symmetry of the forces in horizontal directions depends on the effective spring constant of the support points. It depends on the support area of the Viton cylinder as well as the accurate position and the spring constant of the spring wires. Using the results of the FEM simulations we estimated that the measured vibration sensitivity of $k_z = 14.5 \text{ kHz}/(\text{m}/\text{s}^2)$ is caused by an imbalance of 6% of the acting forces.

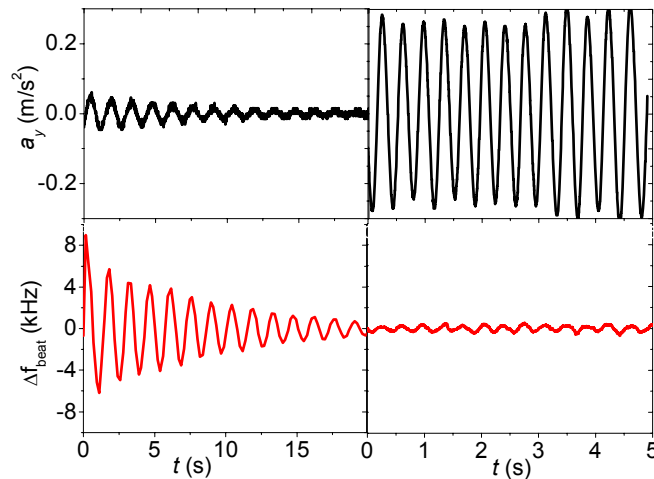


Fig. 3.14 Comparison of the sensitivity of the laser frequency Δf_{beat} to vertical accelerations a_y for the asymmetrical (left-hand figure) and the symmetrical (right-hand figure) mounting configuration.

3.3.6. Vibration isolation

A good performance of a vibration-insensitive cavity can be further improved by an isolation of the environmental vibrations. In the range below 100 Hz the vibrations are of seismic and acoustic origin. In this work a commercial passive vibration isolation (VI) system 100 BM-1 (*Minus-k Technology, Inglewood, CA, USA*) was used. This system has an eigenfrequency of 0.5 Hz in the horizontal and vertical direction.

Fig. 3.15 shows the vibration isolation system. The reference cavity, which is situated in a vacuum chamber, and the mode matching optics are located in a temperature stabilized aluminium cylinder surrounded by the styrofoam box (in the middle of the picture). The styrofoam box is covered by thin lead sheets with a thickness of 0.5 mm in order to suppress the eigenvibrations of the box. The box and the components for the Pound-Drever-Hall stabilization are placed on the top of the Minus-k vibration isolation platform. Special attention must be paid on the cables, which are connecting electronic devices with the components on the platform, since the cables transmit the environmental vibrations and degrade the performance of the VI system. Thus an additional mass-spring system (top of the photo) is used to uncouple the supply cables from the VI [tam06]. The mass-spring system has an eigenfrequency of 1 Hz. The vibration level on the VI was measured using a seismometer GS-1 (*GeoSpace Technology, USA*).

Fig. 3.16 shows the measured vibrations for the horizontal (left-hand figure) and vertical (right-hand figure) directions. The grey lines correspond to the level of vibrations on the top of the VI in the configuration as shown in Fig. 3.15, i.e. without the additional acoustic isolation box. The improvement due to this additional isolation is



Fig. 3.15 Vibration isolation system. The reference cavity is within the lead covered styrofoam box, which is situated on the top of the vibration isolation platform (Minus-k). The setup is surrounded by an additional acoustic isolation box (not jet installed on the photo).

indicated by the black lines and amounts up to one order of magnitude. In the frequency range below 10 Hz the air condition system in the lab contributes to the vibration level (compare the dashed lines taken when the air condition was switched off). The increase of the measured vibrations in the range below 0.5 Hz is due to the amplification of the external forces close to the resonance.

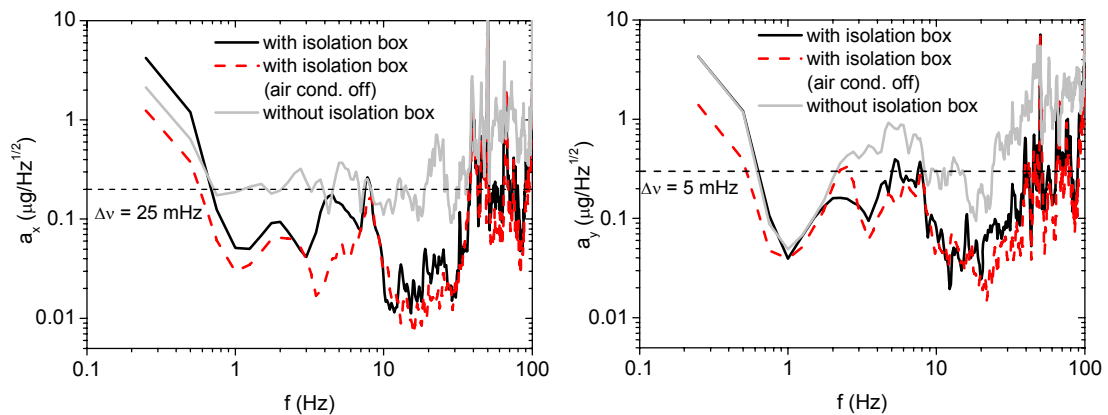


Fig. 3.16 Vibration isolation: the spectra of the horizontal a_x and vertical a_y vibrations measured on the vibration isolation platform without the acoustic isolation box (grey line), on the platform with the installed isolation box (black line), and in the last configuration when the air condition system was switched off (dashed line).

With the sensitivity coefficients measured in the subsection 3.3.5, the vibrations present in the lab contributes with only 25 mHz in the horizontal and 5 mHz in the vertical direction and are not the dominant contributions to the laser linewidth.

3.3.7. Fully compensated cavities

For a cavity mounting that is insensitive to acceleration in all directions, extensive vibration isolation suppression would not be necessary anymore. In the vertical direction the achieved suppression of vibration-induced length fluctuations comes close to the limit set by mechanical tolerances and numerical errors of the calculation. For further improvement towards $k_y = 0$ the mass distribution can be adjusted by adding small masses to the top or bottom of the cavity spacer, depending on the measured sensitivity.

To further reduce the influence of horizontal vibrations, the symmetry of the reaction forces acting in this directions needs to be adjusted. To symmetrize the effective spring constants by modifying the springs, seems to be quite challenging. A much simpler way would be to use nonlinear springs, i.e. springs where the spring constant depends on the working point. This can be achieved by using conical springs or elastomers where the area changes with load. If the nonlinearity of opposite supports has opposite sign, then the effective spring constant can be symmetrized by varying the static load by tilting the setup which can be performed even during operation [ste06].

3.4. Suppression of high-frequency noise

3.4.1. Noise suppression by optical filtering

In subsection 4.4 is shown that the frequency fluctuations in high-frequency range degraded significantly the stability of a frequency standard due to the Dick effect. Optical cavities have been used for spectral [wil98a] and spatial [hal05, zha07, lab07] cleaning of laser beams. For very high finesse cavities the storage time τ_{st} of the photons in the cavity can be so long that the frequency fluctuations of the light transmitted through the cavity are reduced for Fourier frequencies higher than $1/\tau_{st}$. Thus, the cavity acts as a low pass filter and suppresses the frequency fluctuations as follows

$$S_v^c(f) = S_v^0(f) \cdot \frac{1}{1 + (f / \Delta\nu_{HWHM_{cav}})^2}, \quad (3.19)$$

where S_v^c and S_v^0 are the frequency fluctuations of the cavity filtered and of the incident light respectively and $\Delta\nu_{HWHM_{cav}}$ is the half width at half maximum of the cavity.

The experimental setup for filtering laser light with an optical cavity is shown in Fig. 3.17. As filtering cavity the reference cavity itself is used. The full width at half maximum amounts to 19 kHz. From the total output power of Master2 of 6 mW, 0.45 mW are used for the Pound-Drever-Hall stabilisation. On resonance the cavity transmits about 9% of the incident power resulting in 40 μ W transmitted power. Since this power is not sufficient for using in the experiment, an additional slave laser is injection-locked to achieve a power of up to 30 mW.

First the new experimental setup was built without the Faraday isolator after the cavity. Measuring a beat note between Master1 and Master2 a significant degradation of the frequency stability of Master 2 was observed (see Fig. 3.18, lower line). The Faraday isolator in front of the slave laser sends due to an imperfect matching of its polarization and the polarization of the laser light a small fraction of the output power of the slave laser in the direction back to the reference cavity.

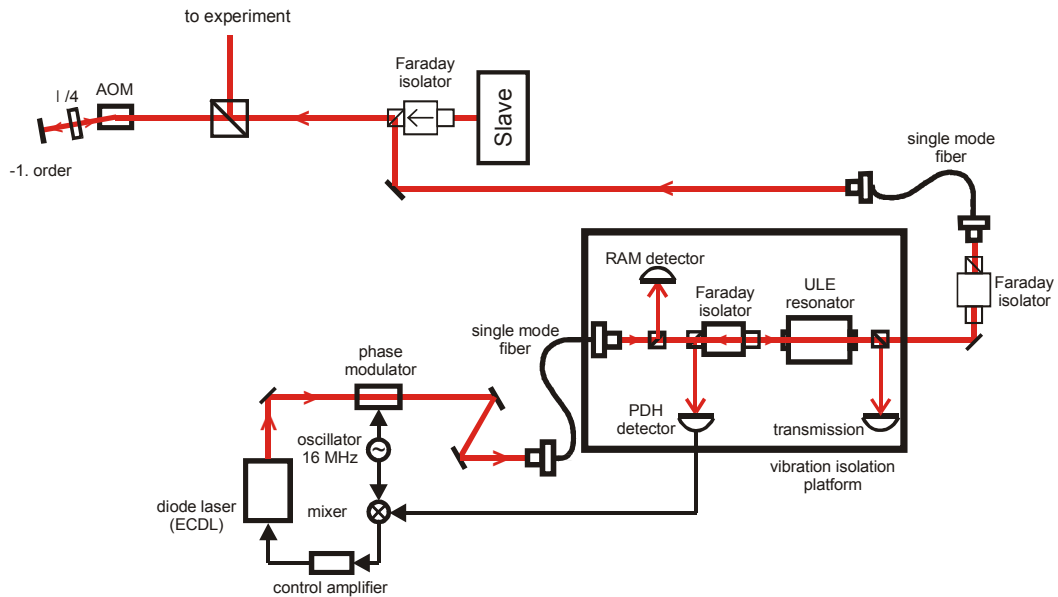


Fig. 3.17 Schematic setup for filtering laser light with an optical cavity

Since this light is perfectly mode matched and has the right polarisation as it goes through the cavity, it adds a signal on the Pound-Drever-Hall detector, which is used to stabilize Master2 laser, and degrades the frequency stability of the laser. The phase of the light field of the slave laser is changing slowly over the time leading to interferences in the beat note (lower line in Fig. 3.18). In the shown case 15 nW are falling onto the cavity resulting in interferences with an amplitude of 110 Hz. This spurious power could be reduced by careful alignment of the polarisation of the Faraday isolator to 10 nW leading to an interference amplitude of 80 Hz. The signal measured with the detector is proportional to the square root of the power of the incident beam. Thus, in order to reduce the influence of the optical feed back below one Hertz the spurious power had to be reduced by a factor of 10^4 . This was achieved using a second Faraday isolator between the reference cavity and the slave laser. This isolator was placed on the vibration isolated platform between the cavity and the fibre in order also to reduce the stray light from the fibre surface. The isolator has a measured attenuation of 37 dB and reduces the spurious power to 2 pW. The middle line in Fig. 3.18 shows the improvement of the frequency stability of Master2 laser due to the use of the additional isolator.

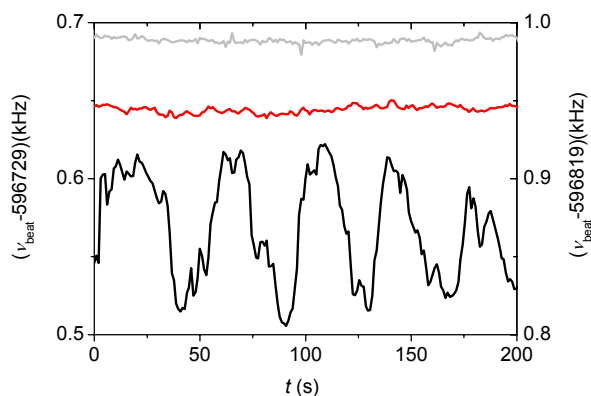


Fig. 3.18 Beat notes between Master1 and Master2 lasers with (low line) and without (upper line) optical feed back of the slave laser. The middle line shows the improvement due to the use of a second Faraday isolator.

In order to characterize the performance of the modified laser system, the delayed self-heterodyne measurement was performed again with the light from the slave laser. Fig. 3.19 shows the enormous improvement of the spectral purity of the cavity filtered light. The measured spectrum of the slave laser (red line) is now limited by the noise and the dynamic range of the spectrum analyser. The expected improvement according to (3.19) is depicted in grey. The additional noise caused by the injection-lock will be discussed in the next subsection. The influence of the reduced frequency noise in the high-frequency range on the Dick effect is discussed in 4.4.

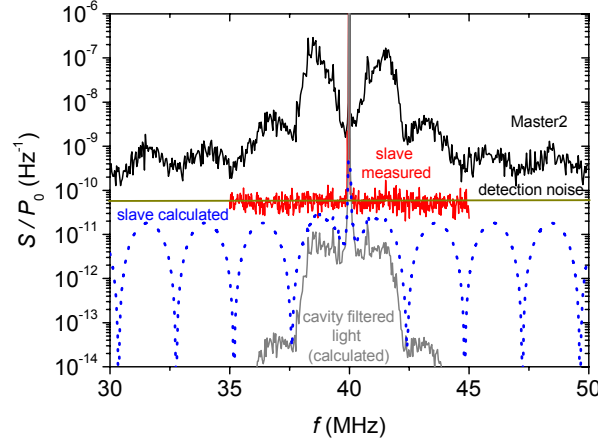


Fig. 3.19 Spectra of the fluctuations of the photodiode current taken with the master laser and with the slave laser. The expected improvement is calculated according to (3.19). The calculated spectrum for the slave laser takes into account the additional noise of the injection-lock (see 3.4.2)

3.4.2. Noise of the injection-lock

The light field of an injection-locked slave laser follows the frequency noise fluctuations of the master laser and exhibits the linewidth of the master light field. Furthermore, the slave laser adds an additional noise due to its own spontaneous emission. The frequency fluctuations of the slave field can be written according to [gal85] as

$$S_v(f) = S_v^{ML}(f) + S_v^{free}(f) \frac{f^2}{\Delta f_{lock}^2}, \quad (3.20)$$

where $S_v^{ML}(f)$ and $S_v^{free}(f)$ are the frequency fluctuations of the master field and of the free running slave field respectively, Δf_{lock} is the half-width of the locking bandwidth. For further calculations a level of $3 \cdot 10^6 \text{ Hz}^2/\text{Hz}$ for the free running frequency fluctuations corresponding to a fast linewidth of 10 MHz and $\Delta f_{lock} = 200 \text{ MHz}$ are assumed in agreement with our experimental conditions.

3.4.3. Spectrum of frequency fluctuations of the interrogation laser

In this subsection the frequency fluctuations of Master2 are characterized after the modifications mentioned above were carried out. It is important to know the spectrum of the frequency fluctuations of the interrogation laser in order to be able to calculate the Dick effect (see 4.4).

For the measurement of the frequency fluctuations of Master1 (Fig. 3.3) the light of the stabilized laser was also coupled into the second reference cavity and the Pound-Drever-Hall signal of the second cavity was taken as a frequency discriminator [sto04].

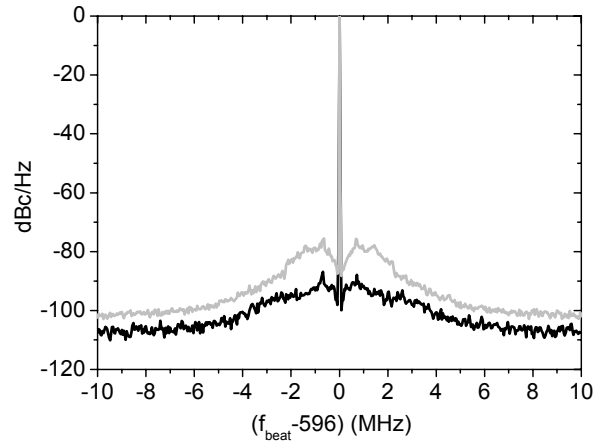


Fig. 3.20 Beat notes between Master1 and Master2 lasers (grey line) and Master1 and Slave lasers (black line).

To characterize the frequency fluctuations of Master2, the information was obtained from the comparison of the beat notes between Master1 and Master2 $S_{beat1}(f) = S_{M1}(f) + S_{M2}(f)$ and Master1 and slave laser $S_{beat2}(f) = S_{M1}(f) + S_{SL}(f)$ (Fig. 3.20).

Since the laser field of the slave laser is cavity filtered, its frequency fluctuations in the high-frequency range are negligible (see Fig. 3.19). Thus, $S_{beat2}(f)$ gives the frequency fluctuations of Master1 $S_{M1}(f)$. Knowing $S_{beat1}(f)$ and $S_{M1}(f)$ the frequency fluctuations of Master2 can be calculated in the high-frequency range (grey line in Fig. 3.21).

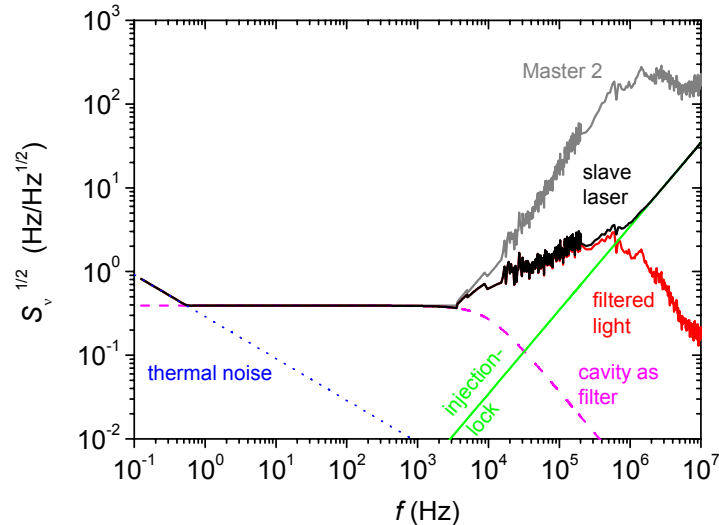


Fig. 3.21 Frequency fluctuations of Master2 (grey line) are suppressed by cavity filtering (red line). The noise contribution of the injection-lock (green line) reduces the performance yielding in the spectrum of frequency fluctuations of the slave laser field (black line).

In the low-frequency range S_v was estimated from the contribution of the dominant influence (i.e. the residual amplitude modulation, see 3.6.3). The red line corresponds to the frequency fluctuations of the cavity filtered light calculated according to (3.19). The contribution of the noise of the injection-lock is indicated in green. The laser field of the slave laser is characterized by the black line. This spectrum is used in subsection 4.4 for the calculation of the Dick effect.

3.5. Quality of the injection-lock

Since the output power of the master laser is not sufficient enough for the experiment, additional injection-locked slave lasers are used to reach enough power for the spectroscopy and cooling (see Fig. 3.36). As one wants to preserve the spectral properties of the master laser, the question about the quality of the injection-lock raises. Thus, the measurements to characterize the injection-lock were performed. For this a heterodyne optical interferometer was build, whose arms consist of the two slave beams used for the spectroscopy. This beat note is shown in Fig. 3.22. On the left-hand side, the frequency

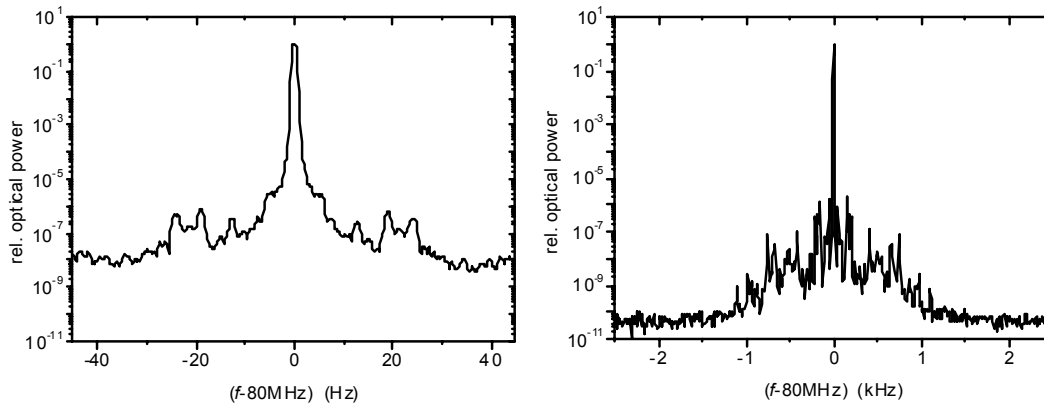


Fig. 3.22 Beat note between the two injection-locked slave lasers used for the spectroscopy. The resolution bandwidth of the spectrum analyzer was 1 Hz.

range close to the carrier is depicted. The width of the beat signal (FWHM = 1 Hz) is limited by the resolution bandwidth of the spectrum analyzer, which was 1 Hz in this case. On the right-hand side, the frequency range of ± 2.5 kHz around the carrier is mapped. Fitting a Lorentzian to the pedestal its fractional power was determined to be less than 0.1%.

Fig. 3.23 represents the relative Allan standard deviation calculated from the measured beat frequencies. Its $1/\tau$ decrease indicates that the noise process is dominated by the white phase noise.

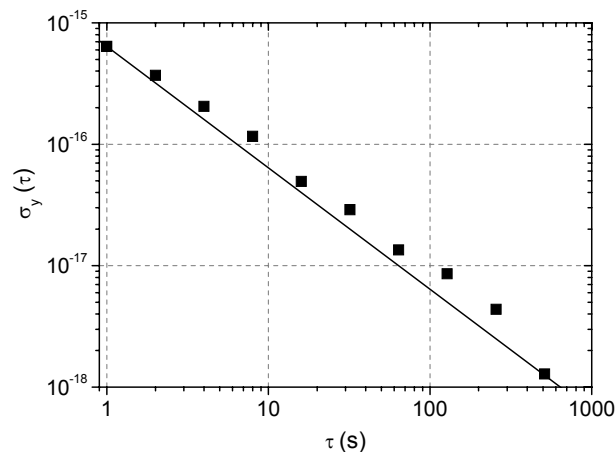


Fig. 3.23 Allan standard deviation calculated from the beat signal between the two spectroscopy lasers

Further, the spectral density of phase fluctuations of the spectroscopy laser was calculated from the measured beat signal (shown in Fig. 3.24). Since in the atom interferometer the instantaneous laser phase is imprinted on the phase of the atomic wave function, the phase excursions of the laser during the interrogation time, which can be up to 1 ms in our case, are important. To be able to reach the quantum projection

noise limit with 10^7 atoms, the phase noise of the laser must be below 0.1 mrad in the frequency range above 1 kHz.

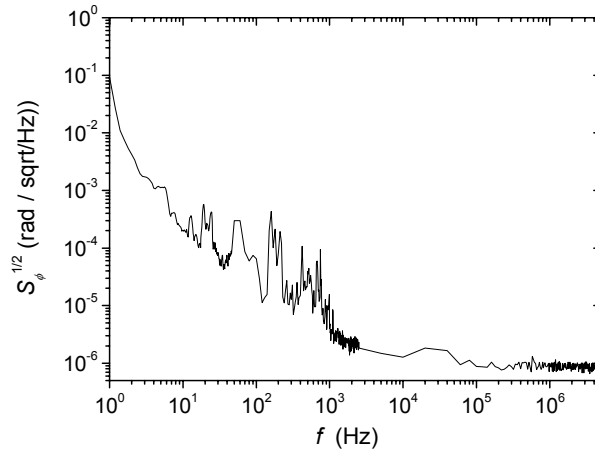


Fig. 3.24 Phase noise of the spectroscopy laser

In order to characterize the power spectrum of the slave laser over a range larger than it is possible with a beat measurement, the power spectrum was taken with an optical spectrum analyzer (*AQ6317C, Yokogawa*). Fig. 3.25 depicts on the left-hand side the power spectrum of the free running laser (grey line) and of the injection-locked laser (black line). The area close to the carrier is enlarged on the right-hand side for the locked laser. The shape of the carrier is determined by the filter function of the spectrum analyzer. The free running laser shows a broad pedestal whose power is only 20 dB below the carrier. When the laser is injection-locked, the power level in the pedestal lies 40 dB below the carrier. Approximately 60 modes of the laser diode have a relative power of 40 dB. From this the fractional power in the pedestal can be estimated to be less than 0.6 % (i.e. $60 \cdot 10^{-4}$).

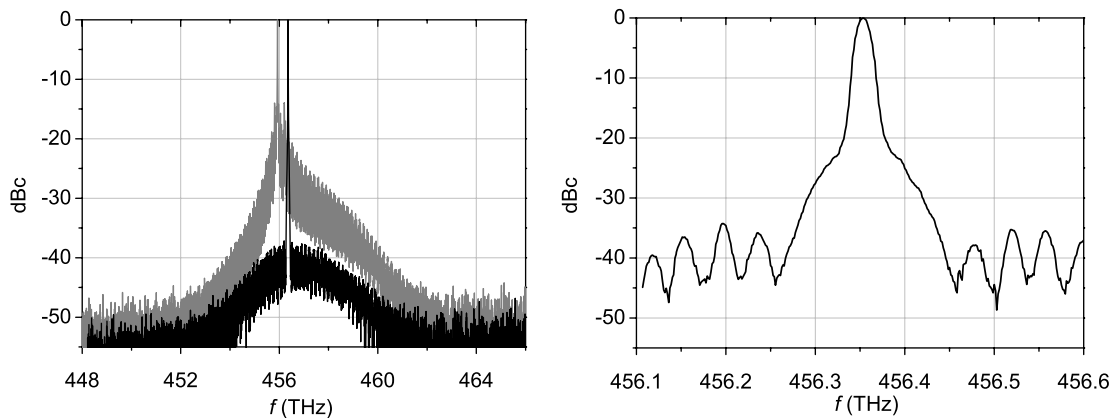


Fig. 3.25 Optical power spectrum of the slave laser: free running (grey line) and injection-locked (black line).

3.6. Frequency stability of the laser

3.6.1. Long term drift of the reference cavity

The reference cavity is made of ultra low expansion (ULE) glass. The glass material shows due to a relaxation process a slow volume contraction, which persists over years. Within the scope of this work the long term drift of the reference cavity used for the stabilization of Master2 was measured over a period of more than 200 days. Therefore the frequency offset between the calcium intercombination line $^1S_0-^3P_1$ and the eigenmode of the cavity was measured by stabilizing the laser to the atomic transition by means of the Doppler-free spectroscopy (Lamb-dip). The course of the measured offset frequency is shown in Fig. 3.26. The measured linear long term drift amounts to 55 mHz/s or 4.75 kHz per day. The relative length changes of the cavity is $1.2 \cdot 10^{-16}/s$. This value is comparable to the one of the reference cavity used for the stabilization of Master1 ($1.6 \cdot 10^{-16}/s$, [sto04]).

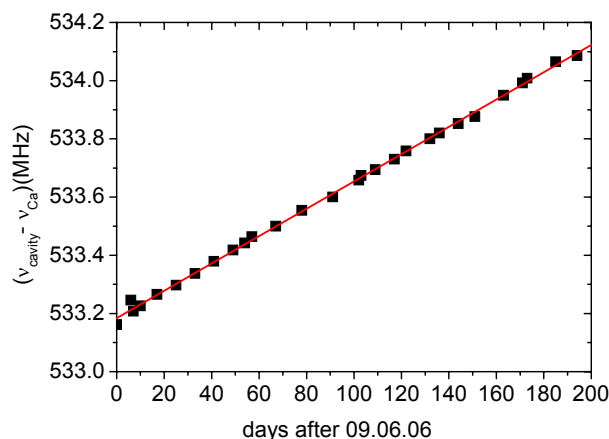


Fig. 3.26 Long term drift of the reference cavity, measured from the offset between the calcium intercombination line and an eigenmode of the cavity, amounts to 55 mHz/s.

3.6.2. Influence of power fluctuations

Since the high reflection mirrors of the reference cavity have a relative absorption in the range of several parts per million, they are heated locally by the laser beam incident onto the cavity and expand leading to the change of the length of the cavity and thus its resonance frequency. To quantify this effect, the power coupled into the cavity was changed stepwise and the beat frequency between two laser systems was recorded at the same time (Fig. 3.27).

The transmitted power through the cavity was changed by $2.6 \mu\text{W}$ and $4.2 \mu\text{W}$. The corresponding change in the beat frequency amounted to -110 Hz and -180 Hz . The measured beat frequency is given as $f_{beat} = f_{M2} - f_{M1}$. Thus the measured reduction of the beat frequency by lowering the transmitted power corresponds to the decrease of the eigenfrequency of the cavity and thus to the expansion of the length. This means the cooling of the mirror substrate due to a positive thermal expansion coefficient of the substrate.

From this measurements a sensitivity of $43 \text{ Hz}/\mu\text{W}$ is determined. In order to be sure that the frequency change is only due to the power change and no electronic offsets are involved, a neutral density filter was put in front of the Pound-Drever-Hall detector and the beat frequency was monitored. If it would be an offset in the electronic loop, it would be decreased by the filter leading to a change in the beat frequency. No frequency change was observed in this case. Thus, the measured sensitivity of $43 \text{ Hz}/\mu\text{W}$ is addressed to be caused only by the power fluctuations. The thermal effect leads to a slow

change of the laser frequency with an exponential time constant of 2 s.

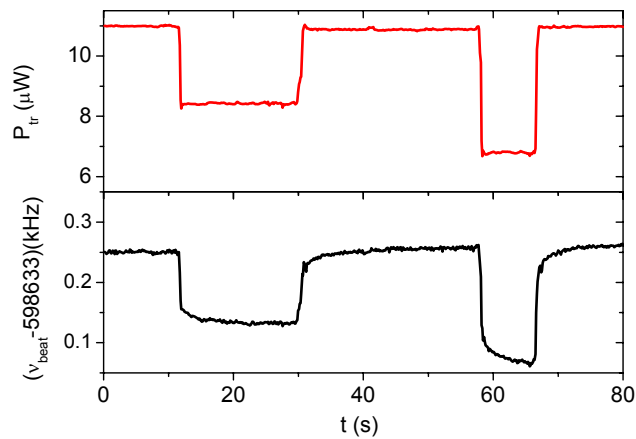


Fig. 3.27 Influence of fluctuations of transmitted power (upper graph) on the frequency stability of the laser (lower graph, the linear drift of the beat note is subtracted).

To determine the influence of the power fluctuations on the achievable frequency stability of the laser, the transmitted power was monitored over a period of several hours and an rms-fluctuation of 0.1% was found. The power used for the Pound-Drever-Hall stabilisation was kept to the minimum that is still sufficient to injection-lock the slave laser. In this case the transmitted power of $11 \mu\text{W}$ would contribute to the frequency instability with 0.4 Hz. Thus, if a sub-Hertz linewidth is aimed, an active power stabilisation technique must be employed. For example, the phase modulator of the Pound-Drever-Hall stabilisation could be additionally used as an actuator for this purpose.

3.6.3. Residual amplitude modulation

The electro-optical modulator, which is used as a phase modulator for the Pound-Drever-Hall stabilisation (see Fig. 3.2), can also act as an amplitude modulator due to the birefringence of the crystal. The temperature fluctuations in the crystal lead to the change of the birefringence and thus to slow variations of the residual amplitude modulation (RAM). Furthermore the residual amplitude modulation is caused by the etalon effect along the beam path. The RAM causes an offset in the Pound-Drever-Hall signal. Thus any fluctuations of the RAM lead to fluctuations of the laser frequency in the low frequency range.

A method to control the RAM was proposed in [won85]. There, an additional dc voltage is applied to the crystal, which arranges that the phase shift due to the natural birefringence and the birefringence due to the applied voltage compensate each other. Within the scope of this thesis a control loop for the RAM compensation was implemented. The schematics is shown in Fig. 3.28. The RAM detector measures the instantaneous amplitude modulation which is mixed down by the mixer with the oscillator frequency of 16 MHz. The control amplifier generates a dc voltage, which is applied to the phase modulator so that the measured signal is zero. The maximum voltage that can be applied at the input of the phase modulator is 250 V due to the type of the construction. The $\lambda/10$ voltage of the phase modulator (PM 25, Linos) amounts to 200 V. Thus, an additional control parameter is needed in order to enable a wide range of controlling. Furthermore, the fact that the index of refraction depends on the temperature of the crystal is employed. The temperature control signal is used to compensate slow fluctuations of the index of refraction.

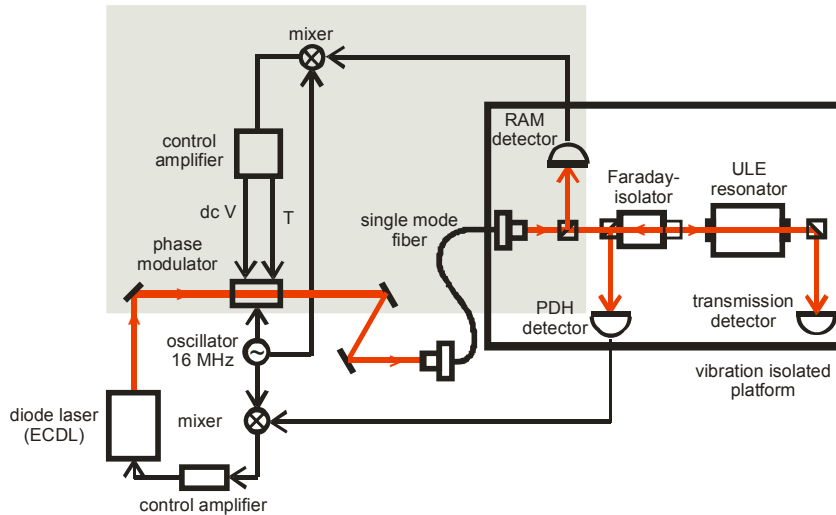


Fig. 3.28 Schematics of the RAM compensation (grey box). The RAM is measured with the RAM detector. The mixer generates two control signals, which are applied to the phase modulator: dc voltage for the fast servo loop and a temperature signal for the slow loop.

As it is mentioned above, there are two different effects that cause the RAM: the birefringence of the crystal and the etalon effect. It is shown in [whi85] that the signals caused by these effects have different phases compared to the Pound-Drever-Hall (PDH) signal. The birefringence effect generates a spurious signal that is in phase with the PDH signal while the etalon effect is shifted by 90° compared to it and thus does not affect the stabilization. Hence, the signal measured on the RAM detector should be adjusted in such way that its phase coincides with the phase of the PDH signal.

To characterize the RAM compensation loop, the signal of the Pound-Drever-Hall detector mixed with the oscillator frequency was analysed with a FFT spectrum analyser in case of the open and the closed compensation loop (Fig. 3.29). The laser was free running far from the resonance.

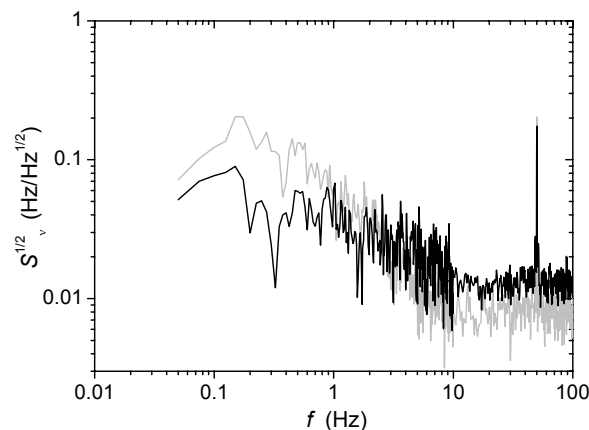


Fig. 3.29 The Pound-Drever-Hall error signal in case of open (grey line) and closed (black line) servo loop for the RAM compensation.

The RAM compensation (black line) reduces the frequency fluctuations of the laser in the low frequency range (below several Hertz). The increase of the frequency fluctuations at higher frequencies can be explained by as follows. When the RAM compensation loop is open, the signal of the Pound-Drever-Hall detector is shot-noise limited. In case of the closed loop the signal of the RAM detector is decreased by the control electronics by adding the same signal with an opposite sign. Thus, the measured shot-noise of the Pound-Drever-Hall detector increases by 3 dB.

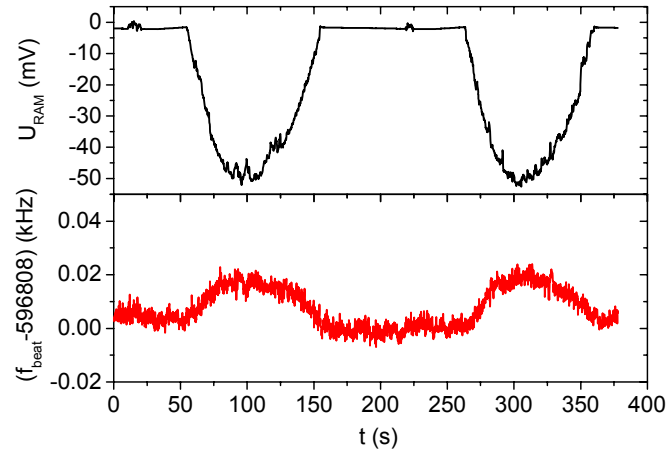


Fig. 3.30 Influence of the residual amplitude modulation (RAM) on the frequency stability of the laser indicated by the beat note between two master lasers. The drift of the reference cavities is subtracted.

To characterize the influence of the RAM on the frequency stability of the laser, the beat note between two master lasers was recorded while the RAM compensation loop was not working properly. The upper graph in Fig. 3.30 shows the fluctuations of the RAM measured with the RAM detector while the RAM compensation loop was oscillating. The lower graph presents the beat note, which was taken simultaneously. A clear correspondence between the RAM and the frequency stability of the laser can be seen.

Next, the signal on the RAM detector was changed stepwise by changing the polarization of the incident laser beam and the beat was recorded at the same time (Fig. 3.31). From this measurement the influence of the RAM on the frequency stability of the laser of 0.3 Hz/mV was determined. The fluctuations of the RAM over a period of several hours were monitored. They amounted to 1.7 mV leading to a frequency instability of 0.5 Hz .

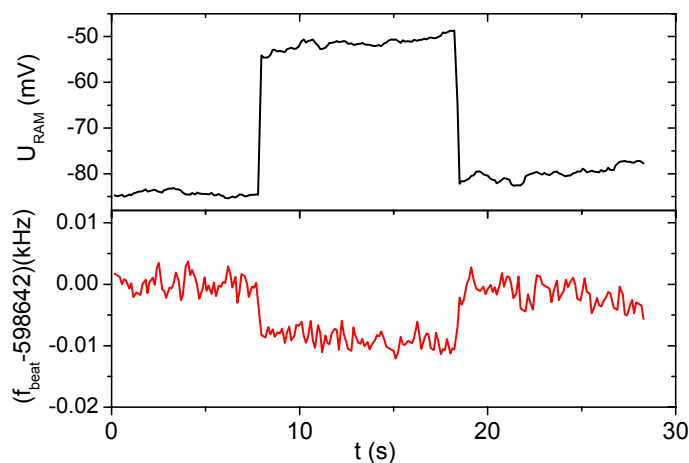


Fig. 3.31 Measurement of the influence of the RAM on the frequency stability of the laser

3.6.4. Comparison of highly stable lasers

To determine the frequency stability and the linewidth of a laser system, it is compared with another laser by means of the beat measurement. The lasers which are compared should have similar properties since the beat signal is dominated by the laser

with the poorer properties. The two lasers at the frequency of 456 THz used for the interrogation of the calcium intercombination line (in this subsection named as Ca1 and Ca2 lasers) can be compared directly by measuring the beat frequency which is in rf range with a photo diode. At PTB, another highly stable laser (in the following named as Yb laser) is available, which is used as a clock laser in $^{171}\text{Yb}^+$ -ion frequency standard ([tam04], [pei06]). Since the frequency of the Yb laser is 344 THz a femtosecond frequency comb is used for the comparison with the calcium lasers.

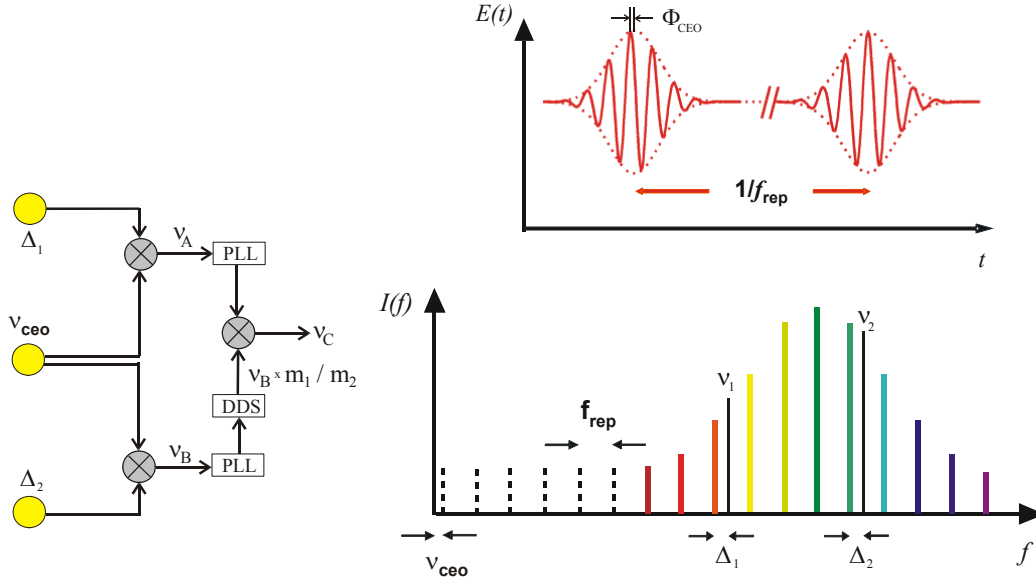


Fig. 3.32 Femtosecond frequency comb in the time and frequency domain (on the right-hand side). On the left-hand side, the principle of the oscillator transfer principle is depicted.

The femtosecond frequency combs are widely used nowadays in the optical frequency metrology because they transfer the measurements of the optical frequencies in the rf domain. The output of a femtosecond laser in the time domain (Fig. 3.32) is a train of short pulses separated by the time $t = 1/f_{rep}$, where f_{rep} is the repetition rate of the laser. In the frequency domain the output is a comb of frequencies with equidistant spacings f_{rep} . Since the group velocity and the phase velocity of the light are not equal the carrier-envelope phase differs from pulse to pulse. Thus, the comb has an offset of v_{CEO} . Any mode of the frequency comb can be described as

$$v_m = v_{CEO} + m f_{rep}, \quad (3.21)$$

where m is an integer, which gives the number of the comb tooth.

To measure the beat between the Ca1 and the Yb laser the transfer-oscillator principle is used [tel02b]. Let v_1 and v_2 be the two frequencies that have to be compared. First the beats between the respective frequency and the next comb tooth Δ_1 and Δ_2 are measured which can be expressed as

$$\begin{aligned} \Delta_1 &= v_1 - (v_{CEO} + m_1 f_{rep}) \\ \Delta_2 &= v_2 - (v_{CEO} + m_2 f_{rep}) \end{aligned} \quad (3.22)$$

After beating Δ_1 and Δ_2 with v_{CEO} one gets the frequencies v_A and v_B :

$$\begin{aligned} v_A &= v_1 - m_1 f_{rep} \\ v_B &= v_2 - m_2 f_{rep} \end{aligned} \quad (3.23)$$

The frequency v_B is divided by the factor m_2/m_1 . The beat frequency between v_A and $v_B \cdot m_1/m_2$ is then given as

$$v_C = v_1 - \frac{m_1}{m_2} v_2. \quad (3.24)$$

The measured beat frequency v_C is independent of the comb parameters v_{CEO} and f_{rep} . Thus, the femtosecond comb does not degrade the frequency stability of the measured lasers. This was demonstrated to a level of $5 \cdot 10^{-18}$ [gro07].

In the case of the particular measurements performed here the beat frequency can be written as

$$v_{\text{beat1}} = v_{\text{Ca1}} - \frac{m_{\text{Ca}}}{m_{\text{Yb}}} v_{\text{Yb}}. \quad (3.25)$$

Simultaneously the beat frequency between the two lasers Ca1 and Ca2 is measured, which is given as

$$v_{\text{beat2}} = v_{\text{Ca2}} - v_{\text{Ca1}}. \quad (3.26)$$

From (3.25) and (3.26) the beat between the Ca2 and Yb laser can be calculated as

$$v_{\text{beat1}} + v_{\text{beat2}} = v_{\text{Ca2}} - \frac{m_{\text{Ca}}}{m_{\text{Yb}}} v_{\text{Yb}}. \quad (3.27)$$

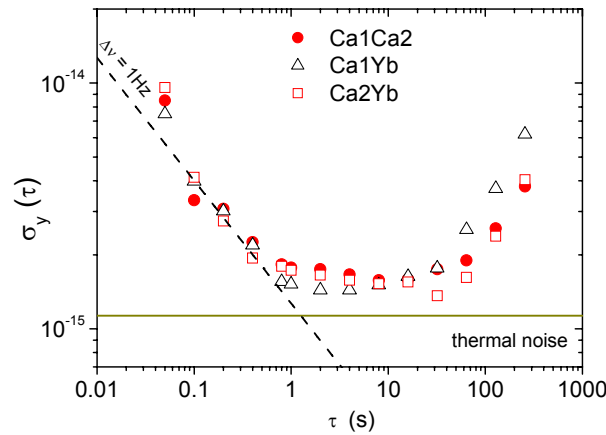


Fig. 3.33 Allan standard deviations calculated from the measured beat frequencies. The dashed line is calculated from the white frequency noise level corresponding to a laser linewidth of each laser of 1 Hz.

Fig. 3.33 shows the Allan standard deviations, which are calculated from the measured beat frequencies. All lasers were locked to their reference cavities. The linear drift of the respective cavities is subtracted. All three beats exhibit very similar behaviour. The $1/\sqrt{\tau}$ slope for $\tau < 1$ s corresponds to the white frequency noise level of 1 Hz. The flicker frequency floor for $1 \text{ s} < \tau < 30 \text{ s}$ lies slightly above the thermal noise level [num04], which gives the fundamental limitation of the frequency stability (see 3.6.5).

When all beat notes are recorded simultaneously the individual instabilities can be estimated using the so called “three-corned hat” method [tn1337]. Three possible joint variances $\sigma_{y_{\text{Ca1}, \text{Yb}}}^2$, $\sigma_{y_{\text{Ca1}, \text{Ca2}}}^2$, and $\sigma_{y_{\text{Ca2}, \text{Yb}}}^2$ are the sums of the individual contributions:

$$\begin{aligned}
 \sigma_{y, Ca1, Yb}^2 &= \sigma_{y, Ca1}^2 + \sigma_{y, Yb}^2 \\
 \sigma_{y, Ca1, Ca2}^2 &= \sigma_{y, Ca1}^2 + \sigma_{y, Ca2}^2 \\
 \sigma_{y, Ca2, Yb}^2 &= \sigma_{y, Ca2}^2 + \sigma_{y, Yb}^2
 \end{aligned} \tag{3.28}$$

The expression for each individual variance is given by

$$\begin{aligned}
 \sigma_{Ca1}^2 &= \frac{1}{2} (\sigma_{Ca1, Ca2}^2 + \sigma_{Ca1, Yb}^2 - \sigma_{Ca2, Yb}^2) \\
 \sigma_{Ca2}^2 &= \frac{1}{2} (\sigma_{Ca1, Ca2}^2 + \sigma_{Ca2, Yb}^2 - \sigma_{Ca1, Yb}^2) \\
 \sigma_{Yb}^2 &= \frac{1}{2} (\sigma_{Ca2, Yb}^2 + \sigma_{Ca1, Yb}^2 - \sigma_{Ca1, Ca2}^2)
 \end{aligned} \tag{3.29}$$

This method works best if all three lasers have comparable properties.

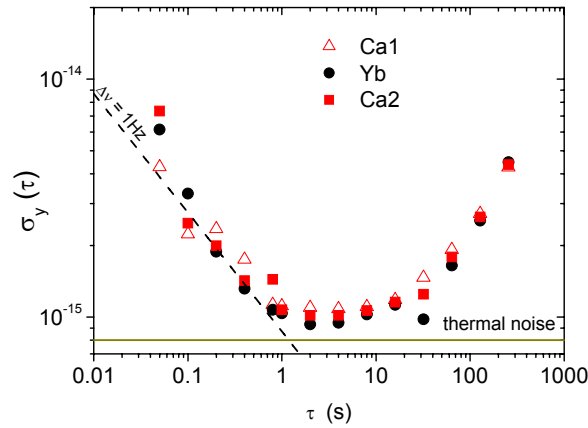


Fig. 3.34 Calculated Allan standard deviations of the individual lasers

Fig. 3.34 shows the calculated Allan standard deviation of each individual laser. As it was already seen in the beat notes, all three lasers have similar performances. In the region between 1 Hz and 20 Hz the Allan standard deviation corresponds to a white frequency noise of a level of 1 Hz. The improvement of the frequency stability of the Master2 laser in the low frequency range due to the novel vibration insensitive mounting of the reference cavity can not be shown since the measured noise now is dominated by the laser with the old mounting.

3.6.5. Thermal noise

As it was shown in the previous subsection, the frequency fluctuations of the interrogation lasers show a flicker floor at a level close to the thermal noise level. In this subsection the thermal noise of the reference cavity is considered and the ways for further improvements are shown. The problem of the thermal noise in the reference cavities used for the stabilization of ultrastable (narrow linewidth) lasers was first pointed out by Numata *et. al* in 2004 [num04]. The thermal noise originates from the mechanical motion of the atoms in the matter due to a nonzero temperature. Even if the coefficient of thermal expansion (CTE) is zero, the thermal noise leads to fluctuations of the length of the reference cavity, which limit the achievable frequency stability, if the laser is stabilized to the cavity. The thermal noise of a cavity is composed of the thermal noise contributions of the spacer itself, the mirror substrates, and the mirror coatings. A basic quantity in considerations of the thermal noise is the mechanical loss

factor φ , which is inverse proportional to the decay time of free mechanical oscillations of the sample. To describe the displacements caused by the thermal fluctuations, the one-sided power spectrum $G_x(f)$ of the displacement x at frequency f is used. The $G_x(f)$ of the spacer, the mirror substrate, and the mirror coating is calculated in [num04] to be

$$G_{spacer}(f) = \frac{4k_B T}{2\pi f} \frac{L}{3\pi R^2 E} \varphi_{spacer}, \quad (3.30)$$

$$G_{mirror}(f) = \frac{4k_B T}{2\pi f} \frac{1-\nu^2}{\sqrt{\pi E w_0}} \varphi_{sub}, \quad (3.31)$$

$$G_{coating}(f) = \frac{4k_B T}{2\pi f} \frac{1-\nu^2}{\sqrt{\pi E w_0}} \frac{2}{\sqrt{\pi}} \frac{1-2\nu}{1-\nu} \frac{\varphi_{coat}}{\varphi_{sub}} \frac{d}{w_0}, \quad (3.32)$$

where L is the length of the cavity, R is its radius, E is the Young modulus, ν is Poisson's ratio, w_0 is the beam radius on the mirror, d is the coating thickness, φ gives the mechanical loss factor of the respective material. The resulting frequency noise is given as

$$\sqrt{S_\nu(f)} = \sqrt{G(f)} \frac{\nu_0}{L} \quad (3.33)$$

with $G(f) = 2(G_{spacer}(f) + G_{mirror}(f) + G_{coating}(f))$ and ν_0 is the laser frequency.

For our cavity with $L = 10.2$ cm, $R = 4$ cm, $w_0 = 204.5$ μm , $E = 6.8 \cdot 10^{10}$ Pa, $\nu = 0.18$, $d = 2$ μm and $\varphi_{spacer} = \varphi_{mirror} = 1.7 \cdot 10^{-5}$, $\varphi_{coating} = 4 \cdot 10^{-4}$ the frequency noise contributions amount to

$$\begin{aligned} \sqrt{S_{\nu spacer}(1\text{Hz})} &= 0.009 \text{ Hz}/\sqrt{\text{Hz}} \\ \sqrt{S_{\nu mirror}(1\text{Hz})} &= 0.186 \text{ Hz}/\sqrt{\text{Hz}} \\ \sqrt{S_{\nu coating}(1\text{Hz})} &= 0.084 \text{ Hz}/\sqrt{\text{Hz}} \end{aligned} \quad (3.34)$$

leading to a total frequency noise of $\sqrt{S_\nu(1\text{Hz})} = 0.3 \text{ Hz}/\sqrt{\text{Hz}}$. The resulting Allan standard deviation can be calculated using the relationship

$$\sigma_y(\tau) = \frac{\sqrt{2 \ln 2 S_\nu(f) f}}{\nu_0} \quad (3.35)$$

giving $\sigma_y(1\text{s}) = 8 \cdot 10^{-16}$.

In the following the possibilities for reducing the thermal noise are discussed. As it is shown in (3.33), the frequency noise is inversely proportional to the cavity length. Thus, one can reduce the thermal noise by increasing the cavity length. However, the length of the ULE blocks is limited by the manufacturing process to 14 cm². In the present case the main contribution to the thermal noise is given by the mirror substrates (see (3.34)). To reduce this contribution, one can increase the size of the beam or, more efficient, to use the substrate made of fused silica, which has a mechanical loss factor of $\varphi_{silica} = 10^{-6}$. Using the fused silica mirror substrates and keeping all other parameters fixed would reduce the thermal noise to $\sqrt{S_\nu(1\text{Hz})} = 0.14 \text{ Hz}/\sqrt{\text{Hz}}$. On the other hand, using two different materials, i.e. ULE for the spacer and fused silica for the

² According to the manufacturer *Corning*, U.S.

mirror substrate, with two different CTE would lead to a shift of the effective CTE of the system resulting in a higher sensitivity to the temperature fluctuations at the working point. This problem can be solved by applying proper measures [leg07].

3.7. Laser system at 657 nm

The drawing of the entire laser system at 657 nm is shown in Fig. 3.36. In the lower part of the picture the master laser, which is stabilized to the reference cavity, the additional slave laser for the power amplification as well as the fibre compensation are depicted. This setup is situated in a separate quiet room in order to reduce the environmental influences as vibration, temperature. The upper part of the drawing represents the setup, which is situated in the calcium laboratory. The light coming from the quiet room, i.e. approx. 0.33 mW, is first amplified by the Slave1.

The main part of this light is sent via fibre to the frequency comb. The remaining light is used for injection locking of the further three slaves. The slave lasers deliver 50 mW output power. Slave2 and Slave3 are generate the light for a spectroscopy beam while Slave4 is used for the cooling on the intercombination line.

Acousto-optical modulators (AOM) are used to shift the laser frequency and for switching the laser beams. For the cooling beam (Slave4) a galvo shutter (*T4-150C, MFE Corporation*) is used instead of the switching AOM in order to get more power as well as to eliminate the stray light causing ac-Stark effect. The galvo shutter allows operating at high repetitions rates, which was not possible with the previous used mechanical shutters [deg05a].

Fig. 3.35 shows the relative frequencies of the master laser and the slave lasers with reference to the calcium intercombination line.

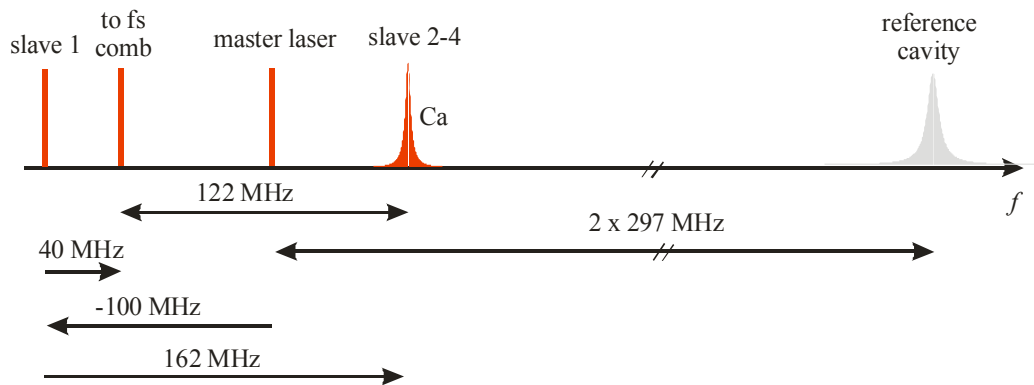


Fig. 3.35 Relative frequencies of the master and slave lasers with the reference to the calcium intercombination line.

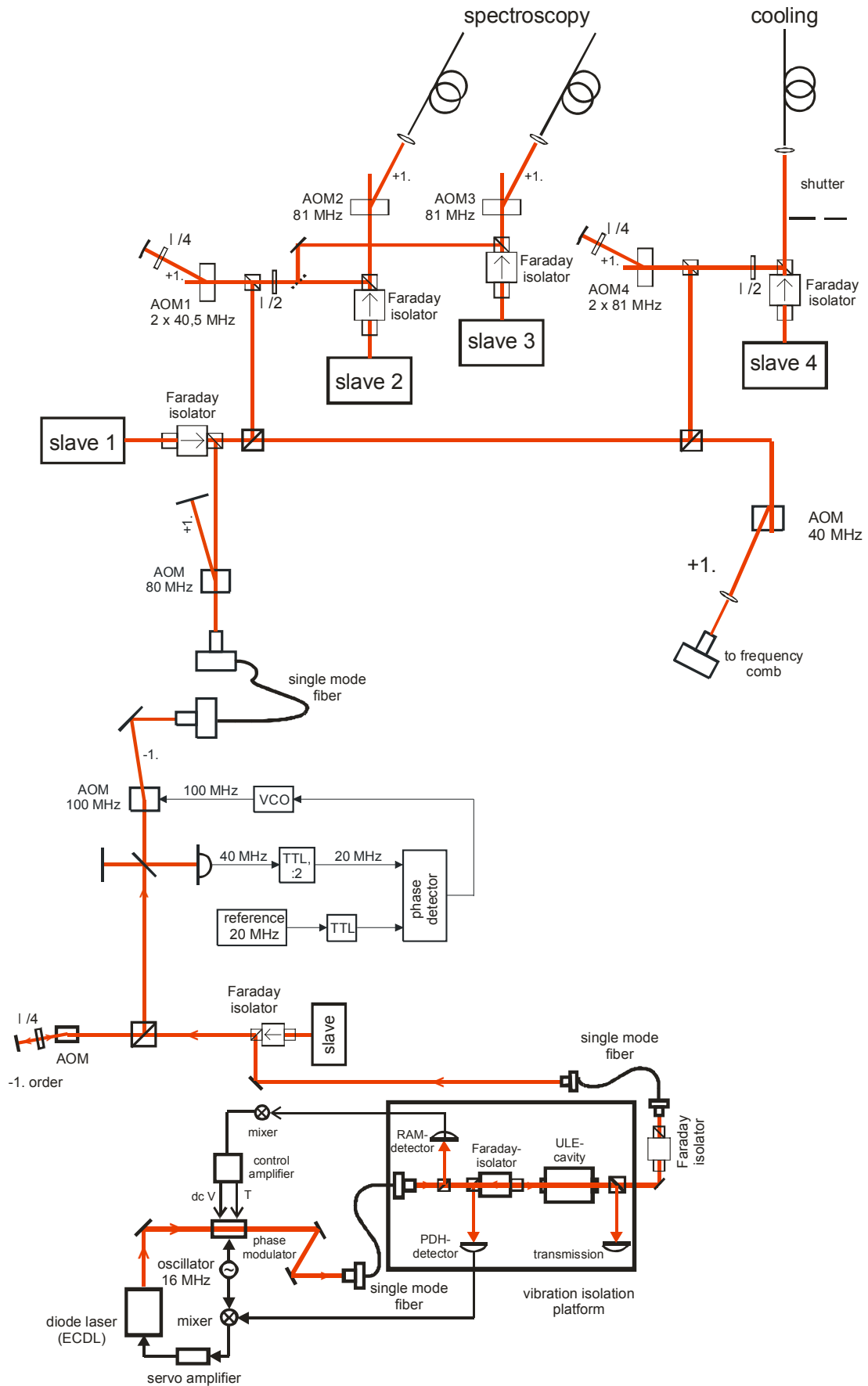


Fig. 3.36 Drawing of the entire laser system at 657 nm

4. Noise in atom interferometers

Any noise in the interrogation process of the atomic line is converted to fluctuations of measured excitation probability. The frequency stability of an atom interferometer, described by the Allan standard deviation, is derived in (2.20) and recalled here as

$$\sigma_y(\tau) = \frac{1}{\pi} \frac{1}{Q} \frac{1}{S/N} \sqrt{\frac{T_c}{\tau}},$$

where $S = Cp_{mean}$ is the signal amplitude, C is the contrast as defined in the subsection 2.2.1, and N is the standard deviation of a dataset of measurements of the excitation probability. The noise appearing in atom interferometers can be organized in two classes, the noise caused by the interrogation itself and the noise due to the detection of the quantum state of the atoms after the interrogation. In this chapter a comprehensive consideration of independent noise contributions N_i is given.

4.1. Quantum projection noise

After performing the atom interferometry each individual atom is in a superposition of the ground $|n_g\rangle$ and excited $|n_e\rangle$ state: $|\psi\rangle = c_e|n_e\rangle + c_g|n_g\rangle$, where $|c_e|^2 = p_e$ and $|c_g|^2 = p_g$ are the probabilities to find the atom in the state $|n_e\rangle$ and $|n_g\rangle$ respectively. When the state of the atom is measured, the atomic wave function is projected onto one of the states. In general the outcome of this measurement cannot be predicted with certainty except in the case when either c_e or c_g is zero. This source of fluctuations is called quantum projection noise (QPN) [ita93] and represents the fundamental limit in interferometric measurements with independent particles.

With N_0 independent atoms the average number $\langle N_e \rangle$ of atoms, which are projected into the excited state is given by

$$\langle N_e \rangle = N_0 p_e, \quad (4.1)$$

where p_e is the excitation probability. N_e has a binomial distribution with the variance

$$\sigma_{N_e}^2 = N_0 p_e (1 - p_e). \quad (4.2)$$

Thus the QPN contribution N_{QPN} to the noise of the measured excitation probability is given by

$$N_{QPN} = \sqrt{\frac{p_e(1-p_e)}{N_0}}. \quad (4.3)$$

The quantum projection noise gives a fundamental limitation for the measurements with independent particles. In the quantum regime, i.e. in measurements with non independent particles (e.g. Bose-Einstein-condensates), the Heisenberg-limit can be achieved, which scales the uncertainty in the measurements as $1/N_0$.

For $N_0 = 4 \cdot 10^6$ atoms, an average excitation probability of $p_e = 0.3$, and a contrast of $C = 0.3$ the QPN contribution to the noise of the measured excitation probability amounts to $N_{QPN} = 2.2 \cdot 10^{-4}$. For a cycle time of $T_c = 50$ ms the achievable stability amounts according to (2.20) to $\sigma_y(1s) = 6 \cdot 10^{-16}$. In order to achieve this ultimate

frequency stability, all other technical contributions must be reduced below the QPN limit.

4.2. Detection noise

An important noise source is the noise of the detection laser since its frequency and power fluctuations between the two pulses lead to fluctuations of the spontaneous emission rate and thus of the detected atom number.

The scattering rate γ of atoms in a laser field is generally given by [met99]

$$\gamma(s, \delta) = \frac{\Gamma}{2} \frac{s}{1 + s + (2\delta/\Gamma)^2}, \quad (4.4)$$

where Γ is the decay rate from the excited state, s is the saturation parameter of the laser beam, and δ is the laser detuning from the atomic transition. The saturation parameter is defined as $s = I/I_{\text{sat}}$, where I is the intensity of the laser beam and $I_{\text{sat}} = \pi\hbar c/3\lambda^3\tau$ is the saturation intensity of the transition, i.e. 600 W/m² for the $^1S_0 - ^1P_1$ transition in calcium.

In the following the origin of the detection noise and its contribution to the noise of the measured excitation probability will be discussed.

4.2.1. Detection noise – a model

Correction of the measured excitation probability

In the experiment the ratio $n = I_2/(I_1 + I_2)$ is measured, where I_1 and I_2 are the fluorescence signals collected in the respective pulse. The measured ratio n is equal to the excitation probability that is given by $p_e = N_e/(N_g + N_e)$ only if $I_1 \propto N_g$ and $I_2 \propto N_e$, which is not the case in the experiment. Hence, the following corrections must be applied. During the first detection pulse of a duration of 40 μs approximately 9% of the excited atoms decay in the ground state, thus $I_1 = N_g + \alpha_1 N_e + \gamma N_0$ with $\alpha_1 = 0.045$ giving the average number of N_e during the first pulse. γ represents the fraction of the hot background atoms, which cannot be excited by the excitation pulse but still contributes to the fluorescence in the first pulse. For the lifetime of the clock transition of 430 μs [deg05a], 10 % of the excited atoms are still absent during the second detection pulse after the detection delay of 1 ms. Furthermore, the detection scheme uses a blow-away pulse of 150 μs duration to remove the atoms detected in the first pulse. However, a fraction of $\beta = 0.02$ of the atoms detected in the first pulse is still present in the second pulse. During the first 190 μs of the detection scheme 36 % of the atoms in the excited state decays. A small fraction of them, i.e. the atoms decaying in the last 50 μs of the blow-away pulse (approx. 10 %) cannot be removed by the laser beam. Let α_2 be the part of excited atoms detected in the second pulse, then $I_2 = \beta N_g + \alpha_2 N_e$. The measured ratio n must be corrected in order to achieve the true excitation probability as follows:

$$p_e = \frac{n(1 + \gamma) - \beta}{n(1 + \beta - \alpha_1 - \alpha_2) + \alpha_2 - \beta} \quad (4.5)$$

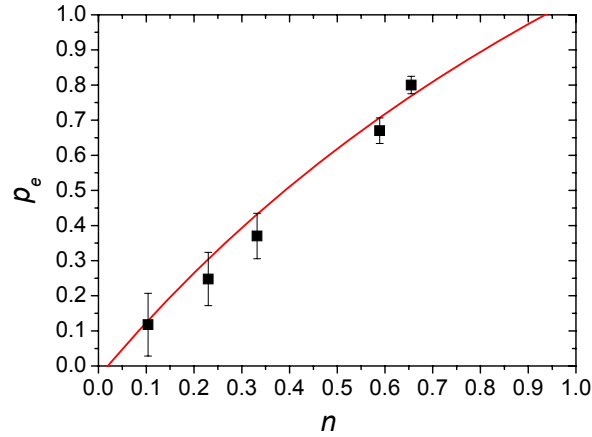


Fig. 4.1 The real excitation probability p_e as a function of the measured ratio n and the fit according to (4.5).

In order to verify the correction formula, the excitation probability was measured directly with another detection scheme. In this measurement, before the excitation pulse the atom number was determined with the first detection pulse while the second pulse gives the number of atoms in the ground state. The directly measured excitation probability is shown in Fig. 4.1 (squares). The solid line shows the fit according to (4.5). From this measurement the missing parameters were determined as $\alpha_2 = 0.65$ and $\gamma = 0.03$. In the following table the correction parameters are summarized.

measured values	abbr.	expression	correction parameter	comment
fluorescence (1. pulse)	I_1	$I_1 = N_g + \alpha_1 N_e + \gamma N_0$	$\alpha_1 = 0.045$	average number of N_e in 1. pulse
fluorescence (2. pulse)	I_2	$I_2 = \beta N_g + \alpha_2 N_e$	$\alpha_2 = 0.65$	fraction of N_e detected in 2. pulse
measured ratio	n	$n = I_2 / (I_1 + I_2)$	$\beta = 0.02$	fraction of N_g present in 2. pulse
excitation probability	p_e	$p_e = \frac{n(1+\gamma) - \beta}{n(1 + \beta - \alpha_1 - \alpha_2) + \alpha_2 - \beta}$	$\gamma = 0.03$	fraction of hot background atoms

Table 4.1 Parameters for the correction of the excitation probability

The parameters used for the correction (i.e. α_2 , β , γ) vary due to variations of the experimental conditions, i.e. the power fluctuations of the blow-away pulse (α_2 , β) and the fluctuations of the velocity distribution of the atomic ensemble (γ). This will be treated in subsection 4.3.

The maximum theoretical excitation probability is unity (i.e. all atoms are excited). This is only valid if the atoms are at rest. Since in the experiment each atom has due to its velocity via the Doppler effect different Rabi oscillation frequencies the average excitation probability differs from unity. Thus, Monte Carlo simulations were performed where the optical Bloch equations were solved for a model system consisting of a laser beam and an atomic ensembles with actual experimental parameters. From this simulations a theoretical value of 0.8 for the average excitation probability was obtained, which well describes the measured value.

Frequency fluctuations of the detection beam

The detection beam can be experimentally realized either as a travelling wave or as a standing wave. In case of the travelling wave atoms are accelerated by the laser beam leading to a change in the detuning during the pulse due to the Doppler-effect and thus the scattering rate is changing with time, i.e. $\gamma = \gamma(\delta(t))$, while the saturation parameter remains constant. The measured signal is the detected number of scattered photons within the duration of the pulse t_{det} .

$$n_{scat} = \int_0^{t_{det}} \gamma(\delta(t)) dt. \quad (4.6)$$

The contribution of frequency fluctuations of the detection laser $\sigma_{\delta \text{ laser}}$ to the noise of the measured excitation probability $\mathbf{N}_{f \text{ det}}$ is given by the noise of the measured photon number

$$\mathbf{N}_{f \text{ det}} = \left| \frac{\partial n_{scat}}{\partial \delta} \right| \sigma_{\delta \text{ laser}} = \int_0^{t_{det}} \left(\frac{d\gamma}{d\delta} \right)_{\delta(t)} \sigma_{\delta \text{ laser}} dt, \quad (4.7)$$

where $\sigma_{\delta \text{ laser}}$ is the frequency fluctuation of the detection laser between two successive pulses. In order to calculate the time-dependent scattering rate, one has to determine the velocity of the atoms during the pulse by solving the differential equation for the atomic movement.

Fig. 4.2 shows the change of the scattering rate of atoms in the laser beam (solid curve) depending on the instantaneous velocity of atoms during a pulse of $40 \mu\text{s}$ duration and the derivative of the scattering rate with respect to the frequency (dashed curve). The scattering rate was calculated for the saturation parameter $s = 1.6$. To determine the contribution of the frequency fluctuations of the detection beam in case of a travelling wave, one has to calculate the integral in (4.7) from 0 to t_{det} . For the given example (travelling wave with the saturation parameter $s = 1.6$, pulse duration $40 \mu\text{s}$, and rms frequency fluctuations of the laser beam $\sigma_{\delta \text{ laser}} = 200 \text{ kHz}$ between two successive pulses) the laser frequency noise contributes with $\mathbf{N}_{f \text{ det}} = 3 \cdot 10^{-3}$ to the noise of the measured excitation probability.

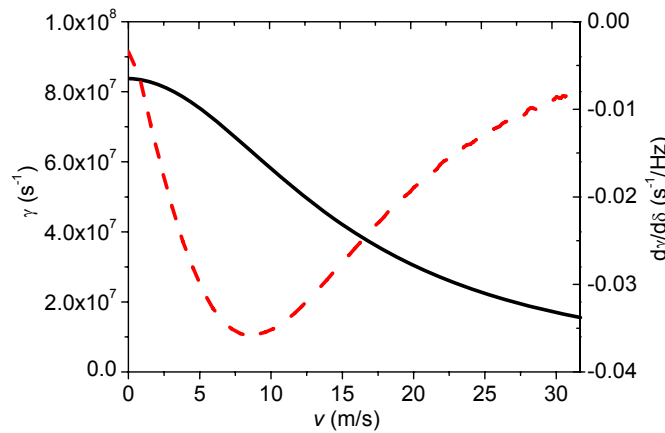


Fig. 4.2 Scattering rate γ of atoms (solid line) and derivative of the scattering rate with respect to the frequency (dashed line) as a function of the instantaneous atomic velocity during a pulse of $40 \mu\text{s}$ duration.

Another detection approach used in this work is to utilize a standing wave, which consists of two independent counter-propagating balanced beams. In this case the atoms

do not get a pronounced average velocity in the direction of the detection beam, only their rms-velocity increases due to the heating in the standing wave. In a particular case of a 8 MHz red detuned standing wave with the average saturation parameter of 3.2 and a pulse of 40 μ s, the rms-velocity of the atomic ensemble amounts to $v_{\text{rms}} = 1.6$ m/s after the first detection pulse. The scattering rate must be replaced in this case by the sum of the scattering rates of both beams of the standing wave (with the saturation parameters s_1 and s_2):

$$\gamma_{sw}(\delta, v) = \frac{\Gamma}{2} \frac{s_1}{1 + s_1 + s_2 + (2(\delta - kv)/\Gamma)^2} + \frac{\Gamma}{2} \frac{s_2}{1 + s_1 + s_2 + (2(\delta + kv)/\Gamma)^2}. \quad (4.8)$$

In the ideal case the saturation parameters of both beams should be equal, i.e. $s_1 = s_2$. In the experiment, however, they differ by a factor of 1.3 (i.e. $s_1 = 1.4$ and $s_2 = 1.8$) due to the slightly different divergence of the beams and losses along the propagation paths.

The total scattering rate γ can be calculated by integration of $\gamma_{sw}(\delta, v)$ over the whole velocity distribution. By solving (4.7) the noise contribution of the frequency fluctuations of the detection beam can be calculated. It amounts to $N_{\text{fdet}} = 5 \cdot 10^{-5}$ in the case of a resonant standing wave. If the detection beam is detuned from the resonance, the noise contribution increases, e.g. to $N_{\text{fdet}} = 1 \cdot 10^{-4}$ for $\delta = 8$ MHz.

Power fluctuations of the detection beam

Power fluctuations of the laser beam lead to additional noise through the fluctuations of the spontaneous emission rate. The scattering rate γ of atoms in a laser field as a function of the saturation parameter is given in (4.4). Since the scattering rate shows a saturating behaviour at higher saturation parameters s , i.e. has different slopes, the measured number of scattered photons has different sensitivities to power fluctuations of the laser beam. Here, a suppression factor f , which describes the ability of the atoms to reduce the relative power fluctuations of the detection laser, is introduced as

$$\frac{d\gamma}{\gamma} \equiv f \frac{ds}{s}, \text{ i.e. } f = \frac{d\gamma}{ds} \frac{s}{\gamma}. \quad (4.9)$$

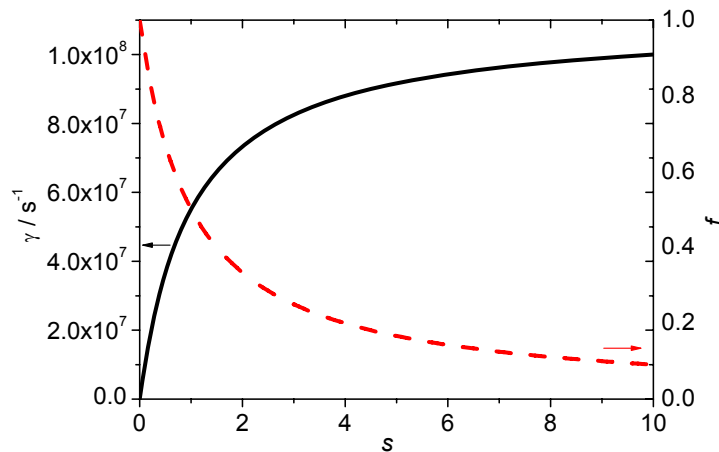


Fig. 4.3 Scattering rate γ of atoms in a laser field (solid line) and atomic suppression factor f for the power fluctuations of the detection beam (dashed line).

Fig. 4.3 shows the scattering rate γ of atoms in a resonant laser field (solid line) and the atomic suppression factor f (dashed line) for different saturation parameters s . In case of a standing wave the atoms see a laser field with a periodically changing intensity, i.e. saturation parameter. Here, a saturation parameter averaged over a half period is used to describe the standing wave. For the maximal experimentally achiev-

ble average saturation parameter of 3.2 relative power fluctuations of the detection beam are suppressed by a factor of 4.

Now the contributions of the power fluctuations of the detection beam to the noise of the measured excitation probability p_e are considered in more detail. Let P_1 be the power of the laser beam in the first and P_2 in the second detection pulse. The parameter κ describes the power fluctuations from pulse to pulse: $P_2 = \kappa P_1$ with the average $\tilde{\kappa} = 1$. To characterise the power fluctuations of the detection beam σ_κ a measurement with stray light sent to the avalanche photodiode and the same time sequence as in experiments with atoms was performed. In this measurement the avalanche photodiode measures scattered light, which is proportional to the power of the detection beam, since no saturation effects occur, i.e. $I \propto P$. The measured signal here is according to (2.22)

$$P_{\text{ampl}} = \frac{\kappa}{1 + \kappa} \quad (4.10)$$

and the fluctuations of σ_κ can be calculated from measured fluctuations of σ_{ampl} as

$$\sigma_{\text{ampl}} = \frac{1}{(1 + \kappa)^2} \sigma_\kappa = \frac{1}{4} \sigma_\kappa. \quad (4.11)$$

In measurements with atoms the signal of the avalanche photodiode is proportional to the scattering rate, which shows a saturation behaviour, i.e. $I_1 = \gamma(s_1)(1 - p_e)$, $I_2 = \gamma(\kappa s_1)\alpha_2 p_e$ with $s_2 = \kappa s_1$. Here, we consider only the correction factor α_2 and neglect the others since they are in order of 2 % to 4 % (see Table 4.1). Thus the measured excitation probability can be written as

$$p_e = \frac{\alpha_2 p_e \gamma(\kappa s_1)}{(1 - p_e)\gamma(s_1) + \alpha_2 p_e \gamma(\kappa s_1)}. \quad (4.12)$$

In order to determine the contribution of power fluctuations of the detection laser $\sigma_{p_e \text{ ampl}}$ to the noise in the measured excitation probability, one has to linearize the scattering rate in the working point:

$$\sigma_{p_e \text{ ampl}} = \left| \frac{\partial p_e}{\partial \gamma(\kappa s_1)} \frac{\partial \gamma(\kappa s_1)}{\partial \kappa} \right| \sigma_\kappa = \frac{\alpha_2 p_e (1 - p_e)}{(\alpha_2 p_e + 1 - p_e)^2} f(s_1) \sigma_\kappa. \quad (4.13)$$

The definition of the suppressing factor f according to (4.9) was used.

4.2.2. Optimization of the detection

The beam reflected at the Brewster surface of the doubler crystal is used as detection beam (see Fig. 2.8). After the electro-optical modulator, which is used for power stabilisation, and the acousto-optical modulator, which is used for switching the beam, about 20 mW laser power is available for the detection beam.

The cloud of ultracold atoms has an rms-radius (decrease of the atom number to $1/e^{1/2}$) of 0.5 mm. The size of the detection beam is a trade-off between the sufficient saturation parameter (i.e. the beam should be small enough) and the homogeneity of the beam in the region of the atoms (i.e. the beam should be big enough). The detection beam has a waist radius of 2.5 mm. The waist radius of a laser beam is defined as the radius, where its intensity drops down to $1/e^2$. With these parameters the intensity of the detection beam at the rms-radius of the cloud amounts to 92 % of its peak intensity. The average saturation parameter of the standing wave is 3.2.

Power fluctuations of the detection beam

In the next step the power fluctuations of the detection beam were characterized. For this purpose the stray light was sent to the avalanche photodiode and the signal was recorded with the same detection scheme as in experiments with atoms. The power fluctuations of the detection beam were measured to be $\sigma_{\kappa} = 4.8 \cdot 10^{-3}$. For the experimental values of $p_e = 0.3$ and $s = 3.2$ they are suppressed by atoms according to (4.13) to $N_{ampl} = 2 \cdot 10^{-4}$. To reduce this contribution well below the level of the QPN of $N_{QPN} = 2.2 \cdot 10^{-4}$ for $4 \cdot 10^6$ atoms, an active power stabilization of the detection laser was built. It uses an electro-optical modulator. A beam splitter splits a part of the laser beam whose intensity is measured by a photodiode and kept constant by means of an electronic control loop.

Fig. 4.4 shows the measured power fluctuations of the detection beam for different time delays between two detection pulses. The line shows the noise level without power stabilisation. The power fluctuations was reduced by a factor of two to $\sigma_{\kappa} = 2.6 \cdot 10^{-3}$ by using the power stabilisation. Their contribution to the noise of the excitation probability amounts to $N_{ampl} = 1.1 \cdot 10^{-4}$ and are now smaller than the QPN.

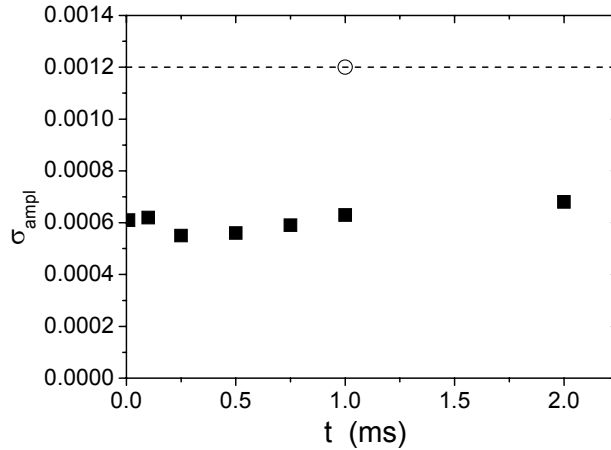


Fig. 4.4 Power fluctuations of the detection beam measured with stray light with (squares) and without (circle) power stabilisation as a function of the time delay between two pulses.

Electronic noise

The electronic noise is due to detector dark noise, amplifier noise, and A/D conversion noise (aliasing and sampling effects). To determine the electronic noise, measurements with no atoms and no laser light were performed with the same detection scheme as in the real experiment. The electronic noise amounts to $\sigma_{dm} = 3.4 \cdot 10^{-4}$ V. Its contribution to the noise of the excitation probability can be calculated by applying the Gaussian law of error propagation to (2.22)

$$N_{dark} = \sigma_{dm} \frac{\sqrt{p_e^2 + (1 - p_e^2)^2}}{I_1 + I_2}. \quad (4.14)$$

For a total measured signal above $I_1 + I_2 = 1.2$ V on the avalanche photodiode the electronic noise lies with $2.2 \cdot 10^{-4}$ in the range of the QPN for $4 \cdot 10^6$ atoms. For the typical experimental value of $I_1 + I_2 = 4$ V the noise amounts to $N_{dark} = 6 \cdot 10^{-5}$.

Duration of the detection pulse

The duration of the detection pulse must be long enough to allow the avalanche photodiode to collect sufficient photons so that the signal is shot noise limited. At least one photon per atom must be detected in order to reach the quantum projection noise regime, i.e. the shot noise of the photodiode should be smaller than the QPN. For the pulse duration of 40 μs and a signal of 4 V on the photodiode the contribution of the photon shot noise to the noise of the excitation probability amounts to $N_{\text{psn}} = 8 \cdot 10^{-5}$ and is below the contribution of the QPN of $N_{\text{qpn}} = 2.2 \cdot 10^{-4}$.

Photon-shot noise

In the shelving detection scheme every atom scatters during a detection pulse of 40 μs duration many photons. But only a part of them are detected. Let n_{ph} be the mean number of detected photons per atom in the ground state. The photon-shot noise contributes to the noise in both detection pulses and leads to a noise in the measured excitation probability:

$$N_{PSN} = \sqrt{\frac{p_e(1-p_e)}{N_0 n_{ph}}}. \quad (4.15)$$

As soon as more than one photon per atom are detected, this contribution becomes smaller than the QPN. The photo current at the avalanche photodiode (APD) of typically 1.5 μA at a resistor of $R = 2.1 \text{ M}\Omega$ is measured directly. The gain of the APD amounts to 6. Then the mean number of detected photons per atom is calculated to be $n_{ph} \approx 8$. This corresponds to a detection efficiency of about 0.03 % of all scattered photons. This is in agreement with the detection efficiency calculated from the detection geometry (the solid angle of the detection is 0.012) and the quantum efficiency of the APD at 423 nm, i.e. 0.2. The contribution of the photon-shot noise to the noise of the measured excitation probability amounts to $N_{PSN} = 8 \cdot 10^{-5}$ for $p_e = 0.3$.

Heating of the atomic ensembles during the detection pulse

A rather high saturation parameter ($s = 3.2$) of the detection beam leads to the heating of the atomic ensembles during the pulse. To investigate this process a cloud of cold calcium atoms with the initial temperature of 1.5 mK was exposed to a detection pulse of 40 μs duration. Afterwards a series of absorption pictures after different expansion times was taken with a CCD camera. From this measurements velocities and temperatures in the direction of the detection beam (x) and perpendicular to it (y) were determined.

With atoms in a resonant 1D molasses in addition to absorption and spontaneous emission also cycles of induced emission take place in the direction of the standing wave absorption. The diffusion coefficient for induced processes along the laser beam, averaged over a period of the standing wave, is given by [coo80] in case of the resonant beam as:

$$D_i = \hbar^2 k^2 \Gamma \frac{s_1}{2}, \quad (4.16)$$

where k is the wave vector and s_1 is the saturation parameter of one beam. The corresponding heating rate amounts to

$$\frac{\partial E}{\partial t} = \frac{D_i}{m_{Ca}} \quad (4.17)$$

with m_{Ca} the mass of the calcium atom.

The resulting temperature increase T_i in the direction of the beam after a detection pulse of the duration t_{det} is given using $E = 1/2 k_B T$ by

$$T_i = \frac{2D_i t_{\text{det}}}{m_{\text{Ca}} k_B} = \frac{t_{\text{det}} (\hbar k)^2 \Gamma}{m_{\text{Ca}} k_B} s_1. \quad (4.18)$$

Eq. (4.18) shows that the temperature increase in the direction of the standing wave is proportional to the saturation parameter and thus does not saturate.

In all direction the heating of the atomic ensembles is caused additionally by the spontaneous emission. The scattering rate for spontaneous processes shows a saturation behaviour (see (4.4)). The temperature increase in this case can be calculated as

$$T_s = \frac{2\hbar^2 k^2 t_{\text{det}} \Gamma}{3m_{\text{Ca}} k_B} \frac{s}{2 + s + (2\delta/\Gamma)^2}. \quad (4.19)$$

Fig. 4.5 shows the temperatures of the atomic ensembles in both directions as a function of the saturation parameter. On the left-hand side the measured final temperature perpendicular to the standing wave is depicted. The curve indicates the theoretical values for spontaneous scattering according to (4.19). The measured temperatures are lying higher than theoretically predicted. Especially at lower saturation parameters where the temperature increases steeper than expected the discrepancy between the theory and the experiment is big. The discrepancy could not be clarified.

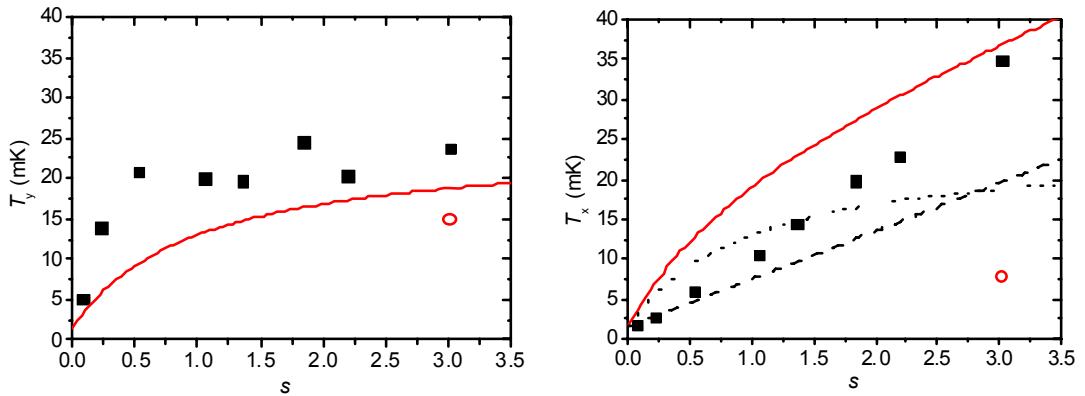


Fig. 4.5 Temperatures of atomic ensembles of cold calcium atoms after a detection pulse of $40 \mu\text{s}$ duration. On the left-hand side: the heating perpendicular to the detection beam saturates due to spontaneous emission. The curve gives the theoretical values according to (4.19). On the right hand-side: the heating along the detection beam does not saturate since here induces processes occur. The lines are theoretical values for spontaneous (dotted line), induced (dashed line) processes and their sum (solid line). The detection beam is resonant with the atomic transition. In case of red detuned beam (10 MHz) the atoms are cooled in a 1D molasses (open circles).

The heating in the direction of the standing wave is the sum of induced and spontaneous processes. On the right-hand side the dashed line shows the calculated values for the temperature increase in case of induced processes according (4.18). The dotted line gives the theory values for spontaneous emission. The calculated sum (solid line) lies higher than the measured points. One possible explanation therefore is that the standing wave was slightly red detuned during this experiment.

As it will be shown later the heating of atoms during the first pulse increases the noise of the measured excitation probability. Thus, the heating process should be

reduced. For this purpose the standing wave was red detuned. In this configuration the detection beam is acting as a 1D cooling molasses. In case of a 10 MHz red detuned standing wave and a saturation parameter of 3.2 the temperature of the atomic cloud amounts to 8 mK along the beam and 15 mK in the perpendicular direction (open circles in Fig. 4.5).

Optimal saturation parameter and detuning for detection

After the general investigations on the influence of the saturation parameter (i.e. suppression of power fluctuation of the detection laser) and the detuning (i.e. heating of atoms during the detection pulse) given above, in the next step their contributions to the noise of the measured excitation probability were characterized more in detail. For these measurements an ensemble of approx. 10^8 cold calcium atoms with an initial temperature of 1.5 mK was prepared. With the applied detection scheme the ratio ξ of the atoms left in the detection region after a delay time of 1 ms was measured, which amounts to $\xi = 0.7$. The noise σ_ξ is the standard deviation of ξ over 200 cycles.

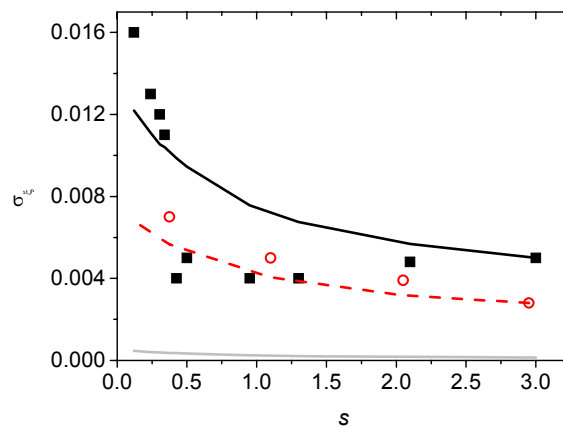


Fig. 4.6 The noise of the measured ratio ξ of atoms remaining in the detection region after 1 ms as a function of the saturation parameter in a resonant standing wave (squares) and a 5 MHz red detuned beam (circles). The grey line depicts the calculated noise due to power fluctuations of the detection beam. The lines are calculated contributions of an excess noise process attributed to the heating of atoms during the first pulse (see text for details).

Fig. 4.6 shows the noise σ_ξ for different saturation parameters. The grey line displays the noise level expected from power fluctuations of the detection beam weighted by the suppressing factor of atoms. The excess noise is attributed to have its origin in the heating of the atomic ensemble during the first pulse. Thus, these atoms contribute stronger to the noise in the second pulse due to fluctuations caused by temperature fluctuations after the first pulse. To explain this noise behaviour as a function of the saturation parameter more quantitatively, the following model is used. In the beginning of this section it was shown, that the atoms suppress power fluctuations of the detection beam at higher saturation parameters. Now we consider the temperature of atoms depending on the saturation parameter. The temperature is an average over all three spatial dimensions. In two of these dimensions (perpendicular to the detection beam) the temperature saturates with s (compare with (4.19)). In the direction of the beam the temperature grows linear with s . Thus, the average temperature rises less than linearly with the saturation parameter for small s . Thus the same formalism can be applied in this case and a kind of temperature suppressing factor can be calculated in analogy to those in (4.9).

Then the contribution of fluctuations due to the heating during the first pulse is

calculated for the highest measured saturation parameter and carried on for other s taking into account the temperature suppressing factor (solid line). The squares depict the measured values in case of a resonant standing wave. The measurement does not show the expected behaviour. Especially the fast decrease of σ_ξ at low saturation parameters cannot be explained. The same measurement was performed with a red detuned detection beam (circles). In this case the course can be explained qualitative much better by the theory (dashed line) although a small discrepancy between measured and calculated values persists. At high saturation parameters the noise σ_ξ is lower in case of the red detuned beam. This can be explained by fact that in this case atoms have a smaller temperature after the first pulse since they are cooled in a 1D molasses. Thus, the fluctuations of the heating contribute less to the noise in the second pulse.

In order to reduce the heating of atoms during the detection pulse, the detection beam was red detuned. However, with increasing detuning the scattering rate becomes more sensitive to frequency fluctuations of the detection beam. Thus, the ratio ξ of atoms remaining in the detection region after a time delay of 1 ms was measured at different detunings of the standing wave (see Fig. 4.7).

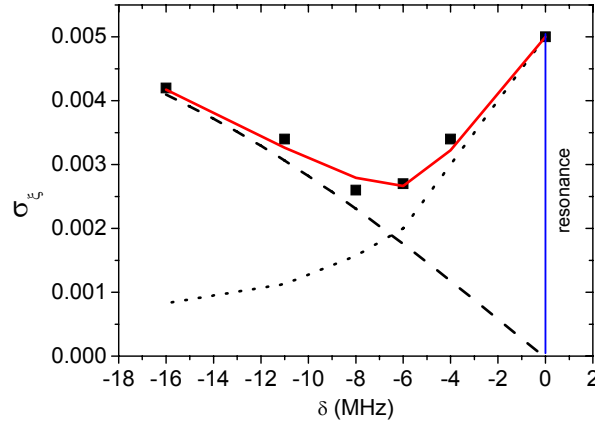


Fig. 4.7 The noise of the measured ratio ξ of atoms remaining in the detection region after 1 ms as a function of the detuning of the detection beam. The dashed line shows the calculated contributions of the frequency noise of the laser. The dotted lines gives the decrease of the noise due to smaller heating of atoms during the first pulse. The red solid line is the calculated sum of both contributions.

In order to explain the measured behaviour of the noise, the following model is assumed. There are two noise sources: one is due to the heating of atoms during the first pulse, an other is due to frequency fluctuations of the detection beam.

The first contribution decreases as the detection beam becomes red detuned due to smaller heating of the atomic ensemble during the first pulse. The dotted line indicates the calculated contribution of the temperature of atoms after the first pulse. The final temperature T_f after the cooling in a molasses is given in [let89] as

$$T_f = \frac{D_i}{\alpha k_B} \quad \text{with} \quad \alpha = 4\hbar k^2 s \frac{2\delta/\Gamma}{(1 + (2\delta/\Gamma)^2)^2}, \quad (4.20)$$

where α is the damping coefficient in the molasses. The calculated final temperatures are a factor of 5 higher then the measured. Thus, they were scaled for the calculations of the noise contributions.

The contribution of frequency fluctuations of the laser beam increases with higher detuning. This can be explained by higher sensitivity to the frequency fluctuations (i.e.

the derivative of the scattering rate with respect to the detuning) with increasing detuning. The contribution of frequency fluctuations $\mathbf{N}_{\text{f det}}$ are calculated according to (4.7) using the expression (4.8) for the scattering rate in case of a standing wave at the appropriate detuning with rms frequency fluctuations of $\sigma_{\delta\text{laser}} = 200$ kHz. The measured noise in Fig. 4.7 can be well explained by the sum of the two contributions.

4.2.3. Detection performance

In this subsection the contribution of the noise of the single detection pulse to the noise of the measured excitation probability is studied. Therefore measurements on ensembles of ultracold calcium atoms with an initial temperature of 25 μK were performed. As a signal n' was again taken a ratio of the detected number of atoms between the second and the first pulse while the time delay between the pulses can also vary. One measures $n' = 1.015 \pm 7 \cdot 10^{-4}$ at a time delay of 10 μs . The apparent increase of the atoms in the second pulse is due to the rise time of the avalanche photodiode. For an experimentally realistic time delay of 1 ms the noise increases about one order of magnitude: $n' = 0.701 \pm 8 \cdot 10^{-3}$. This increase is due to the heating of atoms during the first detection pulse (see 4.2.2). As a consequence the detection scheme was modified and the atoms after the first pulse are blown away by using a propagating resonant beam. The duration of the blow away pulse amounts to 150 μs .

Once as the detection noise of the measurements of the ratio $n' = I_1/I_2$ is determined (i.e. $\sigma_{n'} = 7 \cdot 10^{-4}$) one can calculate the contribution of the noise of the single detection pulse to the noise of the excitation probability as described in (4.12)

$$\mathbf{N}_{\text{det}} = \frac{\alpha_2 p_e (1 - p_e)}{(\alpha_2 p_e + 1 - p_e)^2} \sigma_{n'} \quad (4.21)$$

The noise contribution amounts to $\mathbf{N}_{\text{det}} = 1.7 \cdot 10^{-4}$ for a $\pi/2$ -puls and can be well described by the sum of the power fluctuations ($\mathbf{N}_{\text{ampl}} = 1.1 \cdot 10^{-4}$) and the frequency fluctuations ($\mathbf{N}_{\text{f det}} = 1 \cdot 10^{-4}$) of the detection laser.

In all following measurements the following detection scheme is used:

- Excitation of atoms with an excitation pulse
- Detection of the ground state atoms with the first detection pulse of 40 μs duration
- Blowing away the detected atoms with a pulse of 150 μs duration
- Detection of the excited state atoms with the second detection pulse after 1 ms delay time

The optimal parameter for the detection were following:

- Detuning (red) of 8 MHz
- Average saturation parameter of 3.2
- Pulse duration of 40 μs

Finally all noise contributions to the noise of the measured excitation probability are summed up in the following table. The calculations were done for $N_0 = 4 \cdot 10^6$ atoms, an average excitation probability of $p_e = 0.3$ and a contrast of $C = 0.3$.

Contribution	N_i
QPN	$2.2 \cdot 10^{-4}$
PSN	$8 \cdot 10^{-5}$
Electronic noise	$6 \cdot 10^{-5}$
Detection laser	$1.7 \cdot 10^{-4}$

Table 4.2 Noise contributions of a single detection pulse

4.3. Noise of the single pulse excitation

After the noise of a single detection pulse was characterized in the previous section, the next step was to measure the noise introduced by the excitation through the interrogation laser. This was first done in case of single pulse excitation (Rabi-excitation), since this kind of excitation is less sensitive to the frequency fluctuations of the interrogation laser, which is contrary to the Ramsey-Bordé interferometry. The measurements were performed on an ensemble of $4 \cdot 10^6$ ultracold atoms at a temperature of $20 \mu\text{K}$. The intensity of the excitation pulse was kept constant.

Fig. 4.8 depicts the noise of the measured excitation probability σ_{p_e} versus the excitation probability p_e . The noise was determined as the standard deviation of the measured excitation probability of 200 cycles. The values of p_e were corrected according to the model described in (4.5). The noise of the single pulse excitation lies significantly above the detection noise calculated in 4.2.3.

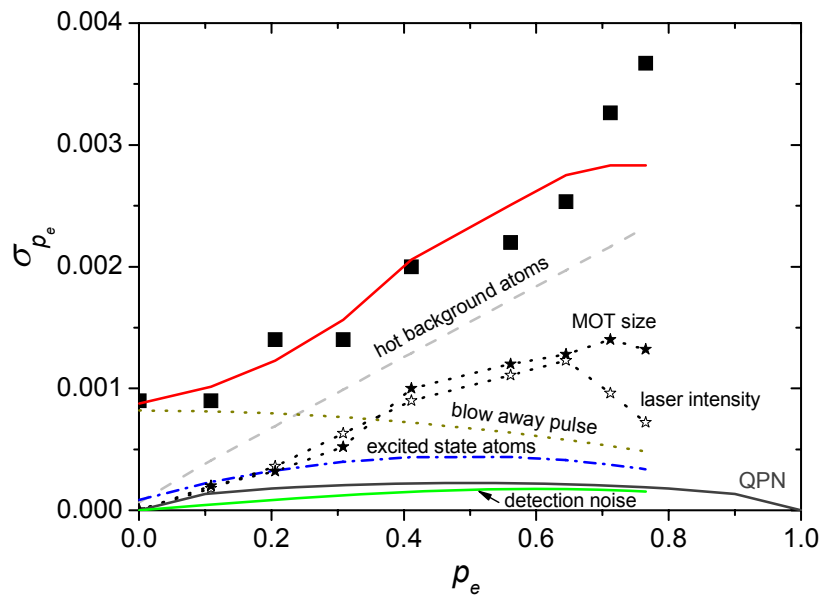


Fig. 4.8 The noise of the measured excitation probability (squares). The noise of a single detection pulse would allow a QPN-limited detection. The contributions of the imperfection of the blow away pulse are shown by the dotted and the dashed-dotted lines. The noise of the excitation process itself is described by the dashed line with open stars for the power fluctuations of the laser, the dashed line with filled stars for the fluctuations of the size of the atomic cloud. The main contribution here is caused by the fluctuations of the number of the hot background atoms (see text for more detail). The red solid line is the sum of all contributions.

The noise contributions can be divided in three groups due to their origin:

- The noise of a single pulse detection pulse (as treated in 4.2.3).

- The noise caused by the imperfection of the blow away pulse.
- The noise of the excitation process.

First, we consider the noise of the processes occurring due to the blow away pulse. Here, we recall again the correction formula (4.5) for the excitation probability as it was derived in the subsection 4.2.1: $p_e = \frac{n(1+\gamma)-\beta}{n(1+\beta-\alpha_1-\alpha_2)+\alpha_2-\beta}$, where n is the measured ratio of the fluorescence of the two detection pulses, $\alpha_1 = 0.045$ is the average percentage of excited atoms measured in the first detection pulse, α_2 is the fraction of the excited atoms measured in the second pulse, β is the part of the ground state atoms contributing to the second pulse due to the imperfection of the blow away pulse, γ describes the proportion of hot background atoms that cannot be excited by the excitation pulse but contribute to the second pulse. The correction parameters fluctuate due to the fluctuations of the experimental conditions. Their contributions to the noise of the excitation probability are calculated using the law of error propagation as

$$\begin{aligned}\sigma_{p\beta} &= \frac{n(\alpha_1 + \alpha_1 + \gamma - n(1+\gamma)) - \alpha_2}{(n(1+\beta-\alpha_1-\alpha_2)+\alpha_2-\beta)^2} \sigma_\beta \\ \sigma_{p\alpha_2} &= \frac{(1-n)(n(1+\gamma)+\beta)}{(n(1+\beta-\alpha_1-\alpha_2)+\alpha_2-\beta)^2} \sigma_{\alpha_2} \\ \sigma_{p\gamma} &= \frac{(1-n)(n(1+\gamma)+\beta)n}{n(1+\beta-\alpha_1-\alpha_2)+\alpha_2-\beta} \sigma_\gamma\end{aligned}\quad (4.22)$$

and are shown in Fig. 4.8. The dotted line represents the contribution of β and was calculated with the measured value of $\beta = 0.02 \pm 0.001$. Approximately 10 % of the excited atoms, i.e. the atoms decaying during the last 50 μs of the blow away pulse, are not removed by the pulse. These atoms are heated and accelerated by the resonant laser beam and contribute stronger to the noise in the second pulse as it was discussed in the subsection 4.2.2. This contribution is shown as a dashed-dotted line in Fig. 4.8 assuming that 10 % of α_2 are fluctuating with $\sigma_{\alpha_2} = 0.01$. The biggest contribution to the noise of the excitation probability is the influence of the hot background atoms. The dashed line was calculated for $\gamma = (3 \pm 1)\%$.

In order to characterize the noise of the excitation process itself, further Monte-Carlo simulations were performed, where the experimental parameters as the initial temperature T of the atomic ensemble, the size x_{rms} of the cloud, and the intensity P in the excitation beams were changed and their influence on the excitation probability Δp_e was determined. The real fluctuation of these parameters were measured ($\sigma_x = 5 \mu\text{m}$ and $\sigma_p/P = 0.03$) and their contributions to the noise of the excitation probability were calculated. Fig. 4.8 displays the calculated noise caused by the fluctuations of the size of the atom cloud (dotted line with filled stars) and by fluctuations of the power of the excitation pulse (dashed line with open stars). The influence of the temperature fluctuations is smaller by one order of magnitude and thus not shown in the graph.

The sum of the possible noise contributions named above is indicated by the red solid line in Fig. 4.8. The behaviour of the measured noise of the excitation probability is well described by the model although the discrepancy for pulses close to the π -pulse is visible.

The excitation probability of $\pi/2$ -pulse was detected as $p_e = 0.4 \pm 0.002$. While the noise of a single detection pulse $N_{\text{det}} = 1.7 \cdot 10^{-4}$ would allow a quantum projection limited detection of $4 \cdot 10^6$ atoms ($N_{\text{QPN}} = 2.2 \cdot 10^{-4}$), the main noise contributions to the

noise of the excitation probability are due to the excitation process itself. The big influence of the hot background atoms is caused by short interrogation times that do not allow the background atoms to leave the detection volume. This problem can be solved by storing the atoms in an optical lattice and using narrow atomic transitions, where longer interrogation times are possible. To decrease the fluctuations due to the size of the cloud, the size of the excitation laser beam should be increased.

4.4. Dick effect

Atom interferometers are operated in a discontinuous periodic mode. In each interrogation cycle a dead time exists while the atomic ensemble is cooled down and prepared for the interrogation. During this time intervals no information about the laser frequency can be obtained when the atom interferometer is used as a frequency standard. Thus the control signal for the clock laser is updated at time intervals T_c . It has been shown that this mode of operation leads to a degradation of the frequency stability of an atomic frequency standard due to down-conversion (aliasing) of laser frequency noise at harmonics of the interrogation frequency $1/T_c$. This effect was first pointed out by G. J. Dick for microwave frequency standards [dic87]. The Dick effect for an optical frequency standard using Ramsey-Bordé interrogation was first addressed by Quessada *et al.* [que03]. There, the contribution of the aliasing effect to the stability of the frequency standard is given by

$$\sigma_y^2(\tau) = \frac{1}{\tau} \sum_{k=0}^{\infty} \left| \frac{g_k}{g_0} \right|^2 S_y \left(\frac{k}{T_c} \right), \quad (4.23)$$

where g_k and g_0 are the zeroth and k^{th} Fourier component of the sensitivity function g , $S_y(f)$ is the relative frequency noise of the interrogation laser. The sensitivity function $g(t)$ is defined as the change in the excitation probability δp_e at the operation point of the frequency standard due to small frequency excursions of the interrogation laser $\delta \nu_L$ at time t :

$$\delta p_e = \frac{1}{2} \int_0^{T_c} g(t) 2\pi \delta \nu_L(t) dt. \quad (4.24)$$

The sensitivity function in case of a 4-pulse Ramsey-Bordé atom interferometer is for the first pair of pulses is then:

$$g(t) = \frac{1}{2} \begin{cases} \sin(\Omega t) & 0 < t < T_p \\ 1 & T_p < t < T_p + T \\ \sin(\Omega(t-T)) & T_p + T < t < 2T_p + T \\ 0 & \text{otherwise} \end{cases}, \quad (4.25)$$

with T_p duration of the $\pi/2$ -pulse. For the second pair of pulses $g(t)$ is said to be $g(t) = g(t - (2T_p + T + T'))$. Fig. 4.9 shows the sensitivity function for a 4-pulse Ramsey-Bordé atom interferometer for a separation time of $T = 454 \mu\text{s}$ and a pulse duration of $T_p = 1 \mu\text{s}$. The Fourier components g_k of the sensitivity function are calculated as:

$$g_k = \frac{2}{T_c} \int_0^{T_c} g(t) \cos \left(\frac{2\pi k t}{T_c} \right) dt. \quad (4.26)$$

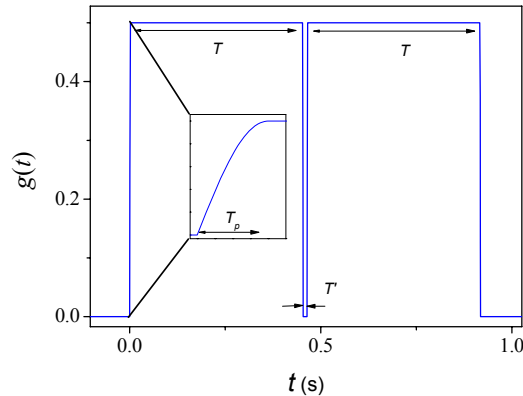


Fig. 4.9 Sensitivity function for the 4-pulse Ramsey-Bordé interrogation. The inset shows the function during the first excitation pulse.

In the following the contribution of the Dick effect to the noise in the atom interferometer according to (4.23) are discussed. The calculation are performed with the known spectral properties of Master2 laser and the slave laser with pure spectral properties in the high frequency range. For details on laser properties see Fig. 3.21. The pulse width amounts to $\tau = 1 \mu\text{s}$, the cycle time $T_c = 50 \text{ ms}$.

Fig. 4.10 a) shows the measured spectral density of frequency fluctuations of the master laser (grey line). The calculated improvement due to the optical filtering according to (3.19) is depicted in red. The frequency fluctuations of the slave laser (black line), which is injection-locked with the cavity filtered light of the master laser, is calculated with taking into account the additional noise caused by the injection-locking itself according to (3.20) (green line).

Fig. 4.10 b) shows the calculated coefficients of the sensitivity function g_k normalized by g_0 for different pulse separation times T of the four-pulse Ramsey-Bordé atom interferometer. g_k/g_0 shows three different slopes: Starting with the value of one, it changes the slope to -1 at the frequency $f \approx 1/(2T)$. About the frequency $f \approx 1/(2T_p)$ it rolls off as f^{-2} .

The values $\sigma_y^p(\tau, f_{\max})$ shown in Fig. 4.10 c) are the partial sums of (4.23) taken up to a maximum index $k_{\max} = f_{\max} T_c$, i.e. considering only frequency noise $S_y(f)$ up to a maximum frequency f_{\max} . They visualize the contributions of the frequency noise at different Fourier frequencies. This calculations show that the reduction of the frequency fluctuations in the high-frequency range can enormously improve the stability of an optical clock (e.g. for $T = 216 \mu\text{s}$, $T_p = 1 \mu\text{s}$, and $T_c = 50 \text{ ms}$ from $\sigma_y(1\text{s}) = 7 \cdot 10^{-14}$ in case of the master laser to $\sigma_y(1\text{s}) = 9.1 \cdot 10^{-15}$ for the filtered light). It is also advantageous to use long separation times T , since in this case the sensitivity function starts to drop at lower frequencies, which, however, is limited by the $430 \mu\text{s}$ lifetime of the excited state.

From the calculations the following conclusions are drawn:

- The contribution of the Dick effect reduces with increasing pulse separation time T because the sensitivity function starts to drop at the frequency $1/(2T)$.
- The high frequency noise of the master laser at the frequencies above 10 kHz is the main contribution to the Dick effect.

This calculations will be used in the next subsection, which considers the noise in the Ramsey-Bordé interrogation scheme.

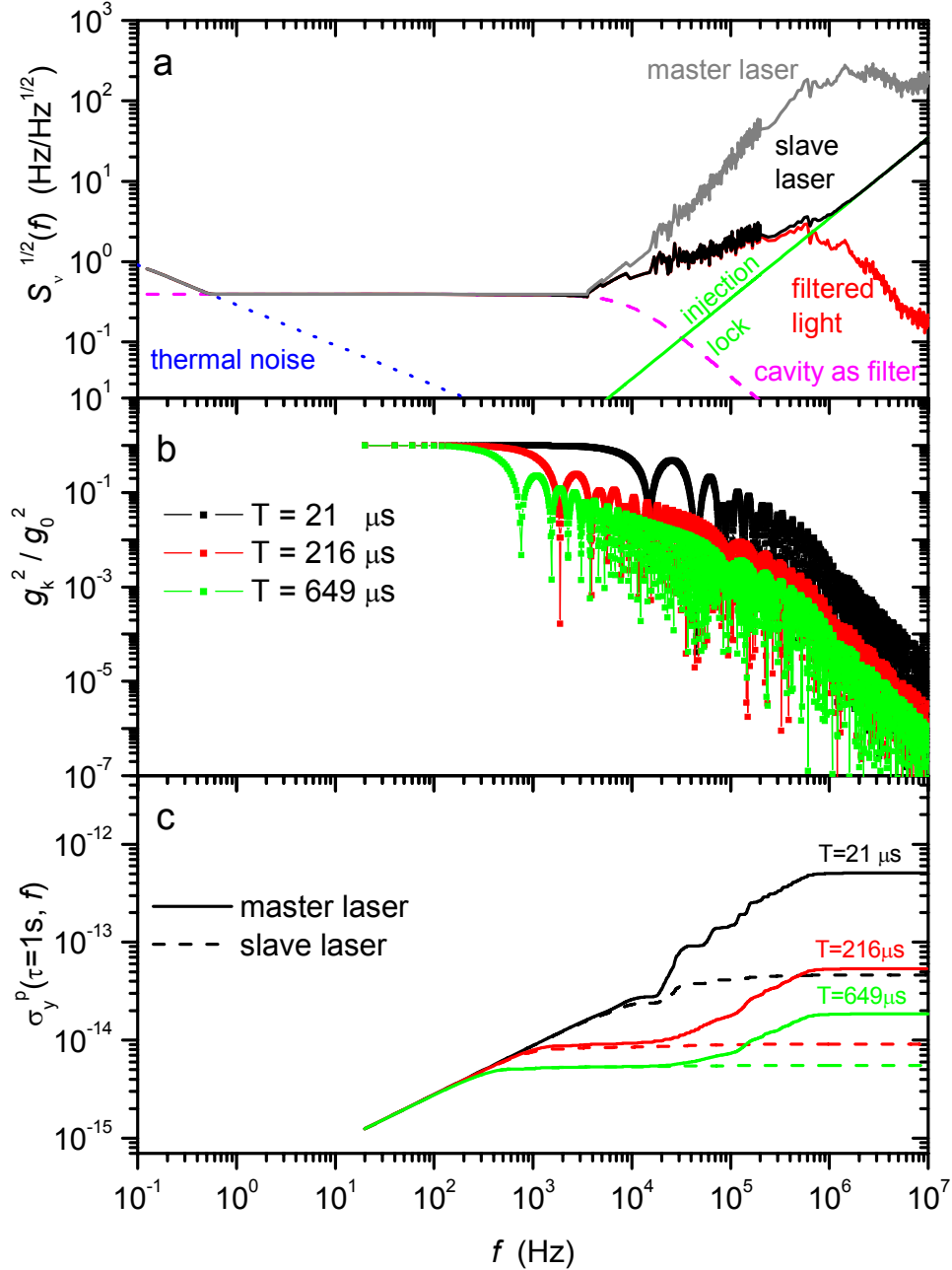


Fig. 4.10 Laser frequency noise and its contribution to the Dick effect. a) spectral density of frequency fluctuation of Master2 laser and of the slave laser, which is injection-locked with the cavity filtered light of Master2 (for detail see Chapter 3). b) calculated coefficients of the sensitivity function g_k for different pulse separation times T in 4-pulse-Ramsey-Bordé atom interferometer. c) partial sum of contributions to the Dick effect for different lasers and separation times (see text).

4.5. Noise of the Ramsey-Bordé interrogation

To demonstrate the improvement due to better spectral properties of the interrogation laser, measurements on an ensemble of $4 \cdot 10^6$ ultracold calcium atoms with a temperature of $15 \mu\text{K}$ were performed using an asymmetric 4-pulse Ramsey-Bordé atom interferometer. The cycle time amounted to $T_c = 50 \text{ ms}$, the duration of the excitation pulse was $T_p = 1.1 \mu\text{s}$ and the pulse separation time was varied from $T = 21.6 \mu\text{s}$ to $T = 649.3 \mu\text{s}$.

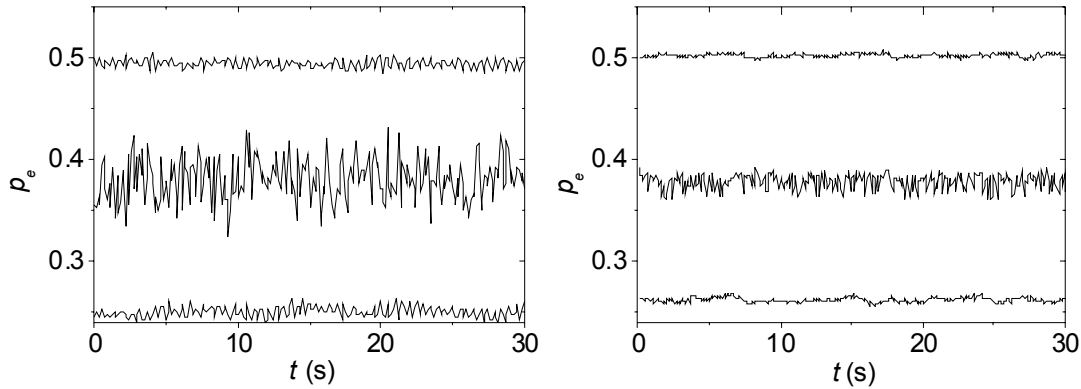


Fig. 4.11 The excitation probability on the maximum, minimum, and turning point (maximum slope) of the Ramsey fringes ($T = 21 \mu\text{s}$) measured with the master laser (left-hand figure) and with the slave laser locked to the light filtered by the cavity (right-hand figure).

The rms-noise of the excitation probability p_e was measured on the maximum, minimum, and turning point (maximum slope) of the central Ramsey fringe using the master laser, which has high noise in the high-frequency range, and the slave laser, which is locked to the light filtered by the reference cavity, for different pulse separation times T . The noise at the top and bottom of the Ramsey fringes is in first order insensitive to frequency fluctuations of the laser and contains all noise sources except the Dick effect, i.e. the additional noise on the slope of the fringe is due to the Dick effect. Fig. 4.11 shows the measurement for the pulse separation time of $T = 21 \mu\text{s}$ using the master laser (left-hand figure) and the slave laser (right-hand figure). The noise on the slope of the fringe in the measurement with the slave laser is about a factor of 3.5 smaller than in the measurement with the master laser.

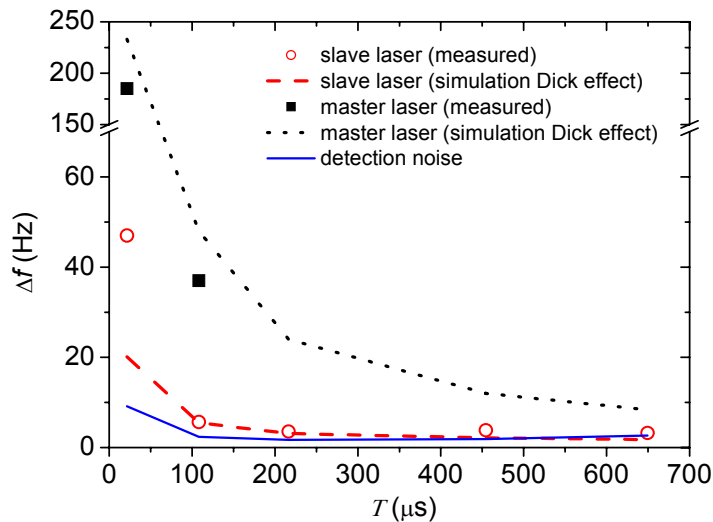


Fig. 4.12 Noise of the measured excitation probability expressed as the standard deviation of the frequency fluctuations on the slope of Ramsey-Bordé fringes for different pulse separation times T measured with the master laser and with the slave laser, which is injection-locked to the light filtered by the reference cavity. The detection noise is averaged from the measurements on maximum and minimum of the fringes. The calculations of the Dick effect are according to (4.23) using the noise spectra in Fig. 4.10 a.

The measured rms-noise of p_e is converted to the frequency noise and shown in Fig. 4.12 for two different interrogation laser configurations: master laser and slave laser. Due to a technical problem at the time of the measurements with the master laser (i.e. stray light from the cooling laser, which shortens the lifetime of the excited state

leading to fast decrease of the contrast of the Ramsey fringes) this measurement could be only performed for short separation times. This problem was solved using a chopper in the measurements with the slave laser. The solid line gives the average noise measured on the maximum and minimum of the fringe and represents the detection noise. The dashed and dotted lines indicate the calculated contributions of the Dick effect according to (4.23) using the noise spectra in Fig. 4.10 a. The measurement clearly indicates the decrease of the noise of the excitation probability when the slave laser with reduced noise in the high frequency range is used. This behaviour is in agreement with the simulations carried out above and the measured noise is well represented by the quadratic sum of the Dick effect and the non-frequency dependent noise.

The expected frequency stability of the atom interferometer was determined from the observed signal-to-noise ratio of the interference fringes for different separation times T according to (2.20) using the signal-to-noise ratio as $S/N = Cp_{mean}/N$, where C is the contrast of the fringe, p_{mean} is the mean excitation probability, and N is the standard deviation of a dataset of measurements of the excitation probability.

Fig. 4.13 shows the Allan standard deviation as a function of the pulse separation time T of the interferometric measurement performed with the spectrally pure slave laser (squares). The achieved S/N ratio of 8.6 at the resolution of $\Delta\nu = 385$ Hz, i.e. $T = 649.3 \mu\text{s}$ leads to a stability of $\sigma_y(1\text{s}) = 7 \cdot 10^{-15}$. The red solid line indicates the detection noise, the quantum projection noise limit for $4 \cdot 10^6$ atoms and the cycle time of 50 ms is depicted by the blue solid line. The triangles represent the calculated contributions of the Dick effect according to (4.23). The part of the Dick effect due to the laser frequency noise in the low-frequency range is given by the dashed-dotted line. This is the main contribution to the Dick effect at higher resolutions according to the simulations in subsection 4.4. The current measurement is limited by the low-frequency laser frequency noise.

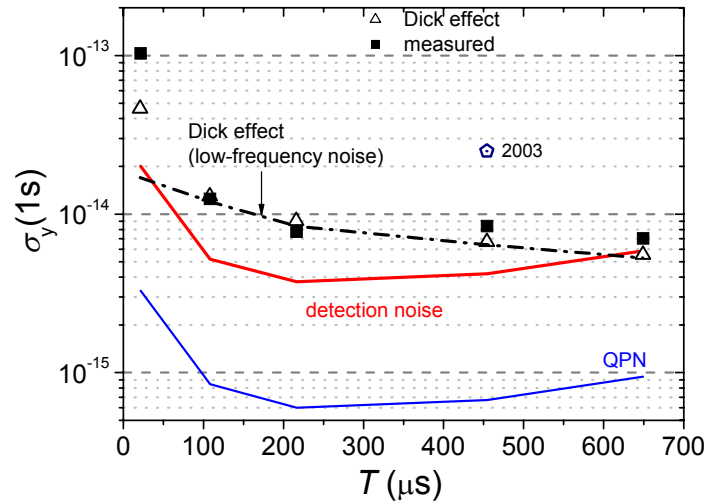


Fig. 4.13 Expected frequency stability of the atom interferometer (squares) determined from the signal-to-noise ratio as a function of the separation time T and the calculated contributions of the Dick effect. The quantum projection noise limit is calculated for $4 \cdot 10^6$ atoms and a cycle time of 50 ms.

In order to show the influence of the low-frequency laser frequency noise on the measured noise on the slope of the fringes, the measurements were compared with the measurements performed using the Master1 laser [sto04]. This laser has a higher frequency noise in the low-frequency range due to the conventional reference cavity

design, which is more sensitive to vibrations [naz06]. The comparison is shown in Fig. 4.14 for $T = 649 \mu\text{s}$. The measurement with the Master2 laser indicates a signal-to-noise ratio that is a factor of two higher than in case of the Master1 laser. Due to the laser drift during the measurements, the noise was calculated via the Allan standard deviation of the measured excitation probability as $N = \sigma_{p_e}(T_c)$.

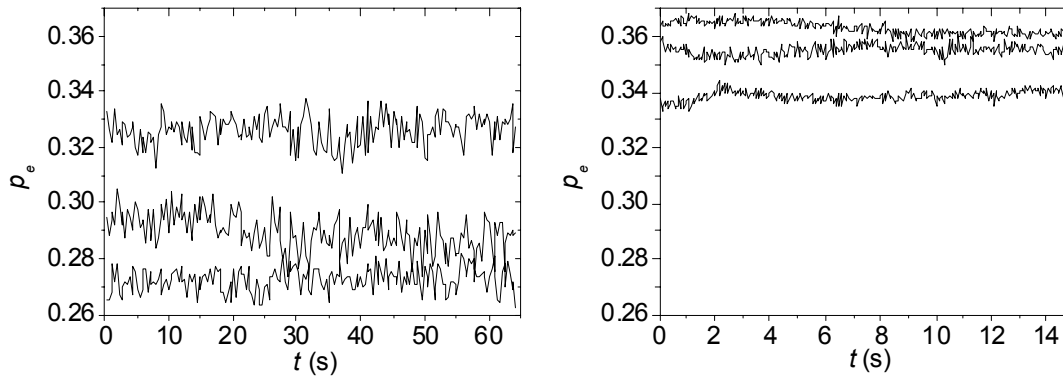


Fig. 4.14 The excitation probability on the maximum, minimum, and turning point (maximum slope) of the Ramsey fringes ($T = 649 \mu\text{s}$) measured with the Master1 laser (left-hand figure) and with Master2 laser (right-hand figure), which has reduced frequency noise in the low-frequency range due to vibration-insensitive mounting.

The noise in the measurement with the Master1 laser was mainly caused by the laser frequency noise in the low-frequency range as it was shown in [sto04]. Since the current measurement with the Master2 laser is also limited by the low-frequency noise, a significant improvement of the frequency noise in this range due to the novel vibration-insensitive cavity mounting of the Master2 could be demonstrated.

4.6. Reducing the Dick effect

Since the stability of the atom interferometer is currently limited by the Dick effect, further measures, which can lead to the reducing of the Dick effect, are discussed in this section. The different interrogation schemes, i.e. the Ramsey-Bordé and the Rabi scheme, are treated separately.

4.6.1. Dick effect in the Ramsey-Bordé interrogation

In the Ramsey-Bordé interrogation scheme, for an optimal separation time T , which is dictated by the lifetime of the excited state, and the minimal possible cycle time T_c further improvements can be achieved by reducing the spectral noise of the frequency fluctuations of the interrogation laser as shown in Fig. 4.15. First, the influence of the residual high frequency noise of the laser in the range above 10 kHz was studied (see Fig. 4.10, a). If we would be able to reduce the noise in the high frequency range so that the interrogation laser would have white frequency noise in the whole frequency range, this would only slightly reduce the influence of the Dick effect, e.g. for $T = 454 \mu\text{s}$ and $T_c = 50 \text{ ms}$ from $\sigma_y(1\text{s}) = 4.8 \cdot 10^{-15}$ to $\sigma_y(1\text{s}) = 4.4 \cdot 10^{-15}$ as indicated by the solid and the dashed line in Fig. 4.15. A considerable reduction can be further only achieved by decreasing the frequency noise in the low frequency range. The black dotted line shows the calculated contribution under the assumption of a white frequency noise in the low frequency range of $\sqrt{S_v} = 0.16 \text{ Hz/Hz}^{1/2}$, which is a realistic level for the present laser

system, if the influence of the residual amplitude modulation and the fluctuations of the power coupled into the reference cavity would be reduced, and the remaining high frequency noise as assumed in Fig. 4.10. The grey dashed-dotted line gives the influence of the Dick effect for the case of white laser frequency noise of $\sqrt{S_V} = 0.16 \text{ Hz/Hz}^{1/2}$ in the entire frequency range. Even with these significant improvement in the frequency stability of the interrogation laser the Dick effect limited frequency stability of the atom interferometer could be only improved by a factor of two. The limitation here for is given by the interrogation scheme itself. As it was shown in the subsection 4.4, the interrogation scheme determines the form of the sensitivity function g that weights the contributions of the frequency noise of the interrogation laser. In order to reach higher frequency stabilities of the atom interferometers, the Rabi interrogation scheme should be applied.

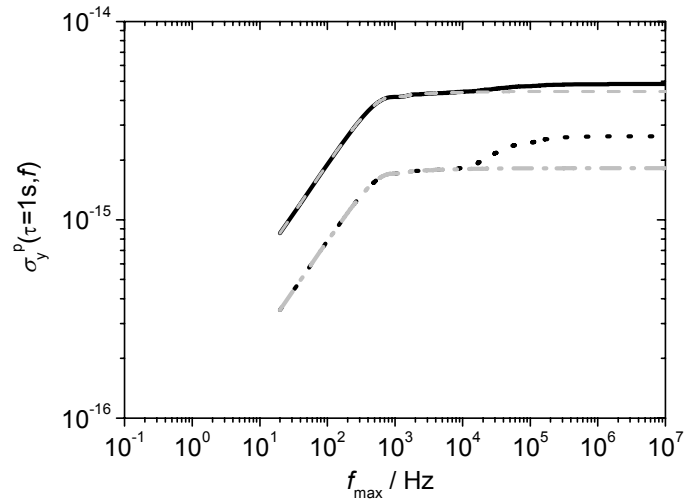


Fig. 4.15 Strategies for reducing of the Dick effect. The black solid line shows the current frequency stability of the atom interferometer. The grey dashed line gives the contribution of the present low frequency noise. Only the reduction of the low frequency noise would reduce significantly the Dick effect (black dotted line) with further prospects of improving by reducing the high frequency noise (grey dashed-dotted line). All calculations are performed for the pulse separation time $T = 454 \mu\text{s}$ and the cycle time $T_c = 50 \text{ ms}$.

4.6.2. Dick effect in the Rabi interrogation

In the Rabi interrogation scheme the atoms are excited by a resonant laser pulse of the duration T_p that meets the requirement $\omega_R T_p = \pi$, where ω_R is the Rabi frequency describing the coupling strength between the atom and the laser field. The Rabi interrogation can be treated as a special case of the Ramsey-Bordé interrogation for $T = 0$. The coefficients of the sensitivity function g are calculated in [que05] as

$$g_0 = \frac{4d}{\pi}, \quad g_k = \frac{4\pi/d}{(\pi/d)^2 - (2\pi k)^2} \cos(\pi k d), \quad (4.27)$$

where d is the duty cycle, which is in case of the Rabi interrogation $d = T_p / T_c$.

Fig. 4.16 compares the coefficients of the sensitivity function g in case of the Ramsey-Bordé interrogation calculated for $T = 454 \mu\text{s}$ and $T_c = 50 \text{ ms}$ (squares) and in case of the Rabi excitation calculated for $T_p = 770 \text{ ms}$ and $T_c = 1 \text{ s}$ (circles). The advantage of the Rabi excitation is clearly seen from this representation as the coefficients of the sensitivity function start to drop at earlier frequencies ($f = 1/T_p$) in the Rabi

case leading to less noise contributions.

However, the application of the Rabi scheme enhances the requirements on the interrogation laser. For the long excitation pulses, the phase fluctuations of the laser broaden the laser linewidth leading to a broadened excitation spectra and a reduced excitation probability. The current performance of the interrogation laser as shown in Fig. 4.10, a) with the white frequency noise in the low frequency range down to a Fourier frequency of $f = 0.5$ Hz corresponds to a laser linewidth of $\Delta\nu_L = 0.5$ Hz. If we would try to resolve a natural linewidth of an atomic transition, which is much narrower than the laser linewidth, the optimal pulse duration would be as shown in [pei06]

$$T_p = 2.44 / (2\pi\Delta\nu_L) = 0.77 \text{ s}.$$

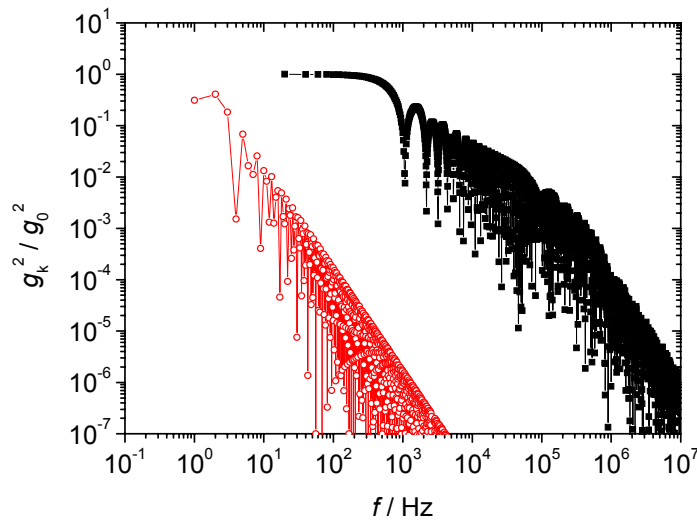


Fig. 4.16 The coefficients of the sensitivity function in case of the Ramsey-Bordé interrogation $T = 454 \mu\text{s}$ (squares) and in case of the Rabi-excitation $T_p = 0.77$ s (circles).

The full potential of the interrogation laser can not be exploited on the atomic system used in this work due to a short lifetime of $^1\text{S}_0 - ^3\text{P}_1$ transition of $430 \mu\text{s}$. Thus, another atomic system is needed. Let us consider for example the case of forbidden optical transitions between the $^1\text{S}_0$ and $^3\text{P}_0$ state in alkaline earth atoms (e.g. ^{87}Sr). Due to the hyperfine mixing this transition is weakly allowed resulting in an extremely narrow linewidth of 1 mHz [tai06]. If we would apply a laser with such spectral performance to this transition using the following time scheme $T_p = 770$ ms and $T_c = 1$ s, the contribution of the Dick effect would be only $\sigma_y(1\text{s}) = 5 \cdot 10^{-16}$.

5. Conclusions

In this work the relevant noise sources in atom interferometers of Ramsey-Bordé type were investigated. The first part of this work describes methods that allowed to reduce the frequency noise of the laser. Two different approaches for the low and the high frequency range were employed. In the low-frequency range, the frequency fluctuations are caused by acoustic vibrations leading to deformations of the reference cavity, which the laser is stabilized to. In this work a novel mounting configuration was realized, which reduces the sensitivity to 1.5 kHz/ms^2 in the vertical and 14 kHz/ms^2 in the horizontal direction. The optical axis is oriented horizontally and the cavity is supported in its symmetry plane on four points. The position of the points were optimized by finite-element analysis. In the conventional design, the reference cavity was supported from below at Airy points. This resulted in a high sensitivity to the acceleration of 120 kHz/ms^2 . In combination with the improved passive vibration-isolation system, the vibrations acting on the cavity contribute with 25 mHz in the horizontal and 5 mHz in the vertical direction to the laser linewidth and are not the most dominant contributions any more.

The other effects, which influence the frequency noise in the low-frequency range, are the residual amplitude modulation (RAM) and the influence of the fluctuations of the power coupled to the cavity. With an additional implemented RAM compensation scheme it is possible to keep the RAM constant over a period of several hours with a precision corresponding to a frequency instability of 0.5 Hz . The fluctuations of the coupled laser power contributed with currently 0.4 Hz to the laser linewidth. With all improvements performed on the laser diode, the reference cavity, and the electronic loop, the laser system shows an extreme stable behaviour. The laser system stayed locked to the reference cavity up to four months.

By comparison with two other narrow linewidth lasers it was shown that the frequency stability of the lasers in the low-frequency range was limited by the thermal fluctuations of the cavity length, which is in the order of $\sigma_y(\tau) = 8 \cdot 10^{-16}$ for $\tau = 1 \text{ s}$ to 10 s for an ULE cavity of 10 cm length.

Furthermore, the influence of the high-frequency laser frequency noise on the frequency stability of an atom interferometer was studied in this work. It was shown that the laser noise in the high-frequency range strongly contributes to the frequency stability via the Dick effect. It can degrade the stability by up to one order of magnitude. It was observed that the linewidth of a free running extended cavity diode laser can differ from one laser system to another by one order of magnitude in spite of careful alignment of the laser leading to a higher frequency noise in the high-frequency range due to the limited gain of the servo loop near the unity-gain frequency. From this point of view it is essential to have an additional possibility to reduce the high-frequency laser frequency noise as it was done in this work by filtering the laser light with an optical cavity, which is the reference cavity itself in this case. The optical cavity acts as a low pass filter for the frequency fluctuations of the laser and suppresses them at frequencies above its linewidth.

In the second part of this work, a systematic study of the noise sources in the atom interferometers of the Ramsey-Bordé type was carried out. Since for an atom interferometer with good stability and accuracy it is necessary to achieve a sufficient signal-to-noise ratio in detecting of the quantum state of the atoms, one focus of this work was on the improvement of the detection scheme. In the new setup, the detection laser is

applied as a standing wave instead of a propagating wave used before. This makes the measurement less sensitive to the frequency fluctuations of the detection laser. In addition, the detection beam is now operated at a higher saturation parameter, which makes the system immune to the power fluctuations of the detection laser. Furthermore, an additional intensity stabilization scheme was established. With these improvements the noise of the single detection pulse contributes to the noise of the excitation probability with $N_{\text{det}} = 1.7 \cdot 10^{-4}$, which already would allow the quantum projection noise limited detection of $4 \cdot 10^6$ atoms ($N_{\text{QPN}} = 2.2 \cdot 10^{-4}$). The improved detection scheme was applied to characterize the noise of the excitation probability in case of the Rabi-excitation. The excitation probability of a $\pi/2$ -pulse was detected with a noise of $N_{\text{pe}} = 2 \cdot 10^{-3}$. The additional noise of the excitation process was found to be caused mostly by hot background atoms, which cannot be excited by the laser pulse but contribute to the measured signal. This fact is due to short interrogation times that do not allow the hot atoms to leave the interrogation region. This problem would be reduced by storing the atoms in an optical lattice and using narrow atomic transitions, which allow longer interrogation times.

Finally, interferometric measurements were performed on ultracold calcium atoms using the improved interrogation laser system and the improved detection scheme. The short-term stability of the atom interferometer was characterized applying Ramsey-Bordé interferometry on an ensemble of $4 \cdot 10^6$ ultracold calcium atoms at $20 \mu\text{K}$. From the observed signal-to-noise ratio a frequency stability of the atom interferometer of $\sigma_y(1 \text{ s}) = 7 \cdot 10^{-15}$ was determined for the cycle time of 50 ms. This is an improvement of a factor of three compared to the measurement with the previous system in 2003. The quantum projection noise limit for this measurements amounts to $\sigma_y(1 \text{ s}) = 6 \cdot 10^{-16}$ in one second and lies hence one order of magnitude under the measured stability. The measurement is mainly limited by the Dick effect.

The methods developed in this work can find wide applications in a variety of fields. The ultra stable narrow-linewidth lasers like the ones developed here, are of great importance for optical frequency metrology, high-resolution spectroscopy, tests of fundamental physics as well as in interferometric measurements including future space missions like the Laser Interferometer Space Antenna project (LISA) [jen04]. Since the laser stability now is already limited by the thermal noise, a lot of effort is currently put into its reduction. One efficient way therefore is to operate the reference cavity at low temperatures because this reduces the thermal fluctuations of the cavity. However, cooling to cryogenic temperatures will introduce additional mechanical vibrations, which may degrade the laser stability. From this point of view vibration-insensitive reference cavities as developed in this work offers due to their high immunity to the vibrations a possibility to take advantage of the cryogenic cooling without losing the narrow laser linewidth.

Aside from the improved frequency stability in the atom interferometers, the reduced frequency noise in the high-frequency range also plays an important role in the high harmonic generation. In the process of high harmonic generation the phase noise power in the signal is amplified with respect to the carrier by the factor m^2 , where m is the harmonic order. For higher harmonic orders the noise background can become larger than the carrier signal so that the carrier cannot be defined any more.

To reach the ultimate frequency stability of a atom interferometer given by the quantum projection noise, it is necessary to reduce further the influence of the Dick effect. This can be obtained by storing the atoms in an optical lattice. This allows to

increase the interrogation time leading to a better duty cycle and thus the reduction of the Dick effect. However, there are some kinds of interferometric measurement that can be only performed on ballistic atoms (like inertial sensors). Those interferometers benefit mostly from the improvement of the stability of the lasers. The new ultra stable spectral narrow lasers as realized in this work offers a possibility of reaching the quantum projection noise limit also for these applications.

References

- [all66] D. W. Allan. Statistics of atomic frequency standards. *Proc. IEEE*, 54:221–230, 1966.
- [ans71] ANSYS 7.1 by ANSYS Inc. Canonsburg, PA, USA.
- [bak76] Ye. V. Baklanov, B. Ya. Dubetsky, and V. P. Chebotayev. Non-linear Ramsey resonance in the optical region. *Appl. Phys.*, 9:171–173, 1976.
- [ber77b] J. C. Bergquist, S. A. Lee, and J. L. Hall. Saturated Absorption with Spatially Separated Laser Fields: Observation of Optical "Ramsey" Fringes. *Phys. Rev. Lett.*, 38:159–162, 1977.
- [bev87a] N. Beverini and F. Strumia. High precision measurements of the Zeeman effect in the Calcium metastable states. In *Interaction of Radiation with Matter, A Volume in honour of A. Gozzini*, Quaderni della Scuola Normale Superiore de Pisa, pages 361–373, Pisa, 1987.
- [bev89] N. Beverini, F. Giammanco, E. Maccioni, F. Strumia, and G. Vissani. Measurement of the calcium $^1P_1 - ^1D_2$ transition rate in a laser-cooled atomic beam. *J. Opt. Soc. Am. B*, 6:2188–2193, 1989.
- [bin01a] T. Binnewies, G. Wilpers, U. Sterr, F. Riehle, J. Helmcke, T. E. Mehlstäubler, E. M. Rasel, and W. Ertmer. Doppler cooling and trapping on forbidden transitions. *Phys. Rev. Lett.*, 87:123002–1–4, 2001.
- [bor84] Ch. J. Bordé, Ch. Salomon, S. Avrillier, A. Van Lerberghe, Ch. Bréant, D. Bassi, and G. Scoles. Optical Ramsey fringes with traveling waves. *Phys. Rev. A*, 30:1836–1848, 1984.
- [bor89] Ch. J. Bordé. Atomic interferometry with internal state labelling. *Phys. Lett. A*, 140:10–12, 1989.
- [bou97] P. Bouyer and M. A. Kasevich. Heisenberg-limited spectroscopy with degenerate bose-einstein gases. *Phys. Rev. A*, 56:R1083–R1086, 1997.
- [car91] O. Carnal and J. Mlynek. Young's double-slit experiment with atoms: A simple atom interferometer. *Phys. Rev. Lett.*, 66:2689–2692, 1991.
- [coo80] R. J. Cook. Theory of resonance-radiation pressure. *Phys. Rev. A*, 22:1078–1098, 1980.
- [dav27] C. Davisson and L. H. Germer. Diffraction of electrons by a crystal of nickel. *Phys. Rev.*, 30:705–740, 1927.
- [deg04a] C. Degenhardt. *Freie und gespeicherte Calcium-Atome für ein optisches Frequenznormal*. PhD thesis, Universität Hannover, Welfengarten 1, 2004. online available at <http://www.tib.uni-hannover.de>.
- [deg05a] C. Degenhardt, H. Stoehr, Chr. Lisdat, G. Wilpers, H. Schnatz, B. Lipphardt, T. Nazarova, P.-E. Pottie, U. Sterr, J. Helmcke, and F. Riehle. Calcium optical frequency standard with ultracold atoms: Approaching 10^{-15} relative uncertainty. *Phys. Rev. A*, 72:062111–1–17, 2005.
- [deh75] H. Dehmelt. Proposed $10^{14} \Delta\nu < \nu$ Laser Fluorescence Spectroscopy on Tl^+ Mono-Ion Oscillator II (spontaneous quantum jumps)", *Bull. Am. Phys. Soc.*, 20:60, 1975.

-
- [dic87] G.J. Dick. Local oscillator induced instabilities in trapped ion frequency standards. In *Proceedings of 19th Annu. Precise Time and Time Interval Conf.*, pages 133–147, Redondo Beach, 1987.
- [dre83] R. W. P. Drever, J. L. Hall, F. V. Kowalski, J. Hough, G. M. Ford, A. J. Munley, and H. Ward. Laser phase and frequency stabilization using an optical resonator. *Appl. Phys. B*, 31:97–105, 1983.
- [ell82] D. S. Elliott, R. Roy, and S. J. Smith. Extracavity laser band-shape and bandwidth modification. *Phys. Rev. A*, 26:12–26, 1982.
- [ess55a] L. Essen and J. V. L. Parry. An atomic standard of frequency and time interval: A caesium resonator. *Nature*, 176:280–282, 1955.
- [est30] I. Estermann and O. Stern. Beugung von Molekularstrahlen. *Z. Phys.*, 61: 95–125, 1930.
- [gal85] P. Gallion, H. Nakajima, D. Debarge, and C. Chabran. Contribution of spontaneous emission to the linewidth of an injection-locked semiconductor laser. *Electron. Lett.*, 21:626–628, 1985.
- [gro07] G. Grosche, B. Lipphardt, and H. Schnatz, to be submitted to *Eur. Phys. J. D*, 2007.
- [gus97] T. L. Gustavson, P. Bouyer, and M. A. Kasevich. Precision rotation measurements with an atom interferometer gyroscope. *Phys. Rev. Lett.*, 78:2046–2049, 1997.
- [hal05] J. Hald and V. Ruseva. Efficient suppression of diode-laser phase noise by optical filtering. *J. Opt. Soc. Am. B*, 22:2338–2344, 2005.
- [hel82] J. Helmcke, D. Zevgolis, and B. Ü. Yen. Observation of high contrast, ultra narrow optical Ramsey fringes in saturated absorption utilizing four interaction zones of travelling waves. *Appl. Phys. B*, 28:83–84, 1982.
- [ita93] W. M. Itano, J. C. Bergquist, J. J. Bollinger, J. M. Gilligan, D. J. Heinzen, F. L. Moore, M. G. Raizen, and D. J. Wineland. Quantum projection noise: Population fluctuations in two-level systems. *Phys. Rev. A*, 47:3554–3570, 1993.
- [jac95] J. Jacobsen, G. Björk, and Y. Yamamoto. Quantum limit for the atom-light interferometer. *Appl. Phys. B*, 60:187–191, 1995.
- [jen04] O. Jennrich, editor. Proceedings of the 5th International LISA Symposium and the 38th ESLAB Symposium, ESTEC, Noordwijk, The Netherlands, 12–15 July 2004, 2004. Special issue of *Class. Quantum. Grav.* **22**, n. 10.
- [kei91] D. W. Keith, Ch. R. Ekstrom, Q. A. Turchette, and D. E. Pritchard. An interferometer for atoms. *Phys. Rev. Lett.*, 66:2693–2696, 1991.
- [lab07] J. Labaziewicz, P. Richerme, K. R. Brown, I. L. Chuang, and K. Hayasaka. Compact, filtered diode laser system for precision spectroscopy. *Opt. Lett.*, 32:572–574, 2007.
- [leg07] T. Legero, private communications, 2007
- [lel87] L. P. Lellouch and L. R. Hunter. Measurement of the $4s4p^1P-4s3d^1D$ spontaneous emission rate in calcium by use of a Stark-electric-quadrupole interference. *Phys. Rev. A*, 36:3490–3493, 1987.

-
- [let89] P. D. Lett, W. D. Phillips, S. L. Rolston, C. E. Tanner, R. N. Watts, and C. I. Westbrook. Optical molasses. *J. Opt. Soc. Am. B*, 6:2084–2107, 1989.
- [mai62] H. Maier–Leibnitz and T. Springer. Ein Interferometer für langsame Neutronen. *Z. Phys.*, 167:386–402, 1962.
- [mcg02] J. M. McGuirk, G. T. Foster, J. B. Fixler, M. J. Snadden, and M. A. Kasevich. Sensitive absolute-gravity gradiometry using atom interferometry. *Phys. Rev. A*, 65:033608–1–14, 2002.
- [met99] H. J. Metcalf and P. van der Straten. *Laser Cooling and Trapping*. Springer, New York, Berlin, Heidelberg, 1999.
- [moe57] G. Möllenstedt and M. Keller. Elektroneninterferometrische Messung des inneren Potentials. *Z. Phys.*, 148:34–37, 1957.
- [nag86] W. Nagourney, J. Sandberg, and H. Dehmelt. Shelved optical electron amplifier: Observation of quantum jumps. *Phys. Rev. Lett.*, 56:2797–2799, 1986.
- [naz06] T. Nazarova, F. Riehle, and U. Sterr. Vibration-insensitive reference cavity for an ultra-narrow-linewidth laser. *Appl. Phys. B*, 83:531–536, 2006.
- [not95] M. Notcutt, C. T. Taylor, A. G. Mann, and D. G. Blair. Temperature compensation for cryogenic cavity stabilized lasers. *J. Phys. D: Appl. Phys.*, 28:1807–1810, 1995.
- [not96] M. Notcutt, C.T. Taylor, A.G. Mann, R. Gummer, and D.G. Blair. Cryogenic system for a sapphire Fabry-Perot optical frequency standard. *Cryogenics*, 36:13–16, 1996.
- [num04] K. Numata, A. Kemery, and J. Camp. Thermal-noise limit in the frequency stabilization of lasers with rigid cavities. *Phys. Rev. Lett.*, 93:250602–1–4, 2004.
- [pei06] E. Peik, T. Schneider, and Chr. Tamm. Laser frequency stabilization to a single ion. *J. Phys. B: At. Mol. Phys.*, 39:145–158, 2006.
- [pet01] A. Peters, K. Y. Chung, and S. Chu. High-precision gravity measurements using atom interferometry. *Metrologia*, 38:25–61, 2001.
- [que03] A. Quessada, R. P. Kovacich, I. Courtillot, A. Clairon, G. Santarelli, and P. Lemonde. The Dick effect for an optical frequency standard. *J. Opt. B: Quantum Semiclass. Opt.*, 5:S150–S154, 2003.
- [que05] A. Quessada-Vial. Developpement d'une horloge à atomes de strontium piégés : Réalisation d'un laser ultra-stable et stabilité de fréquence, 2005. dissertation, Université Pierre et Marie Curie - Paris VI (2005-05-30) - Tuckey Philip (Dir.).
- [ram50] N. F. Ramsey. A molecular beam resonance method with separated oscillating fields. *Phys. Rev.*, 78:695–699, 1950.
- [rat68] C. Rathmann, G. Mann, and M. Nordberg. A new ultralow-expansion, modified fused-silica glass. *Appl. Opt.*, 7:819–823, 1968.
- [rau74] H. Rauch and W. Treimer. Test of a single crystal neutron interferometer. *Physics Letters*, 47A:369–371, 1974.
-

-
- [ric86] L. E. Richter, H. I. Mandelberg, M. S. Kruger, and P. A. McGrath. Linewidth determination from self-heterodyne measurements with subcoherence delay times. *IEEE J. Quantum Electron.*, QE-22:2070–2074, 1986.
- [rie92a] F. Riehle, Th. Kisters, A. Witte, and J. Helmcke. Matter wave interferometry with Ca atoms. In M. Ducloy, E. Giacobino, and G. Camy, editors, *Laser Spectroscopy*, pages 246–251, Singapore, 1992. World Scientific.
- [ros04] This has been suggested by Till Rosenband e.g. at the meeting of the CAUAC network in Porquerolles in April 2004.
- [rut78] J. Rutman. Characterization of phase and frequency instabilities in precision frequency sources: fifteen years of progress. *Proc. IEEE*, 66:1048–1075, 1978.
- [sie86] A. E. Siegman. *Lasers*. University Science Books, Mill Valley, California, 1986.
- [ste03] U. Sterr, T. Binnewies, C. Degenhardt, G. Wilpers, J. Helmcke, and F. Riehle. Prospects of Doppler cooling on forbidden lines. *J. Opt. Soc. Am. B*, 20:985, 2003.
- [ste04a] U. Sterr, C. Degenhardt, H. Stoehr, Ch. Lisdat, H. Schnatz, J. Helmcke, F. Riehle, G. Wilpers, Ch. Oates, and L. Hollberg. The optical calcium frequency standards of PTB and NIST. *C. R. Physique*, 5:845–855, 2004.
- [ste92] U. Sterr, K. Sengstock, J. H. Müller, D. Bettermann, and W. Ertmer. The magnesium Ramsey interferometer: Applications and prospects. *Appl. Phys. B*, 54:341–346, 1992.
- [ste06] U. Sterr, private communications, 2006
- [sto04] H. Stoehr. *Diodenlaser mit Hertz-Linienbreite für ein optisches Calcium-Frequenznormal*. PhD thesis, Universität Hannover, Universität Hannover, 2004. in German, urn:nbn:de:gbv:089-4850973620.
- [sto06] H. Stoehr, F. Mensing, J. Helmcke, and U. Sterr. Diode laser with 1 Hz linewidth. *Opt. Lett.*, 31:736–738, 2006.
- [tai06] A. V. Taichenachev, V. I. Yudin, C. W. Oates, C. W. Hoyt, Z. W. Barber, and L. Hollberg. Magnetic field-induced spectroscopy of forbidden optical transitions with application to lattice-based optical atomic clocks. *Phys. Rev. Lett.*, 96:083001, 2006.
- [tam04] Chr. Tamm, T. Schneider, and E. Peik. Comparison of two single-ion optical frequency standards at the sub-hertz level. In P. Hannaford, A. Sidorov, H. Bachor, and K. Baldwin, editors, *Laser Spectroscopy, Proceedings of the XVI International Conference*, pages 40–48, New Jersey, 2004. World Scientific.
- [tel02b] H. R. Telle, B. Lipphardt, and J. Stenger. Kerr-lens mode-locked lasers as transfer oscillators for optical frequency measurements. *Appl. Phys. B*, 74:1–6, 2002.
- [tim51] S. Timoshenko and J. N. Goodier. *Theory of Elasticity*. McGraw-Hill, New York, 1951.
- [tn1337] NIST technical notes n. 1337

-
- [van89a] J. Vanier and C. Audoin. *The Quantum Physics of Atomic Frequency Standards*. Adam Hilger, Bristol and Philadelphia, 1989.
- [wil02] G. Wilpers. Ein Optisches Frequenznormal mit kalten und ultrakalten Atomen. PTB-Bericht PTB-Opt-66 (ISBN 3-89701-892-6), Physikalisch-Technische Bundesanstalt, Braunschweig, 2002. Dissertation, University of Hannover.
- [wil62] D. C. Williams. The parallelism of a length bar with an end load. *J. Sci. Instrum.*, 39:608–610, 1962.
- [win92] D. J. Wineland, J. J. Bollinger, W. M. Itano, F. L. Moore, and D. J. Heinzen. Spin squeezing and reduced quantum noise in spectroscopy. *Phys. Rev. A*, 46:R6797–R6800, 1992.
- [wit92] A. Witte, Th. Kisters, F. Riehle, and J. Helmcke. Laser cooling and deflection of a calcium atomic beam. *J. Opt. Soc. Am. B*, 9:1030–1037, 1992.
- [wit92a] A. Witte. Laserpräparation eines Kalziumatomstrahls für die hochauflösende Spektroskopie. PhD thesis, Universität Hannover, 1992.
- [wil98a] B. Willke, N. Uehara, E. K. Gustafson, R. L. Byer, P. J. King, S. U. Seel, and Jr. R. L. Savage. Spatial and temporal filtering of a 10-W Nd:YAG laser with a Fabry-Perot ring-cavity premode cleaner. *Opt. Lett.*, 23:1704–1706, 1998.
- [won85] N. C. Wong and J. L. Hall. Servo control of amplitude modulation in frequency-modulation spectroscopy: demonstration of shot-noise-limited detection. *J. Opt. Soc. Am. B*, 2:1527–1533, 1985.
- [you99] B. C. Young, F. C. Cruz, W. M. Itano, and J. C. Bergquist. Visible lasers with subhertz linewidths. *Phys. Rev. Lett.*, 82:3799–3802, 1999.
- [zha07] Y. Zhang, K. Hayasaka and K. Kasai. Efficient noise suppression of an amplified diode-laser by optical filtering and resonant optical feedback. *Appl. Phys. B*, 86:643–646, 2007.

List of Symbols

C	contrast of the interference fringes
d	duty cycle of the interrogation
δ	laser detuning from the atomic transition
γ	scattering rate of atoms in a laser field
Γ	decay rate from the excited state
g	sensitivity function for the Dick effect
I	intensity of a laser beam
N	noise of the measured excitation probability
N_e	number of atoms in the excited state
N_g	number of atoms in the ground state
p_{mean}	average excitation probability
p_e	excitation probability
S	signal of the interference fringe
S_ϕ	spectral density of phase fluctuations
S_ν	spectral density of frequency fluctuations
$\sigma_y(\tau)$	Allan standard deviation
T	time separation between the two pulses in Ramsey-Bordé atom interferometer
T_c	cycle time
T_p	duration of an excitation pulse in Ramsey-Bordé atom interferometer
T'	time separation between the pulse pairs in Ramsey-Bordé atom interferometer

Danksagung

An dieser Stelle möchte ich mich ganz herzlich bei allen Mitarbeitern des Instituts für Quantenoptik der Universität Hannover sowie der Abteilung Optik der Physikalisch-Technischen Bundesanstalt in Braunschweig bedanken, die zum Gelingen dieser Arbeit beigetragen haben. Mein besonderer Dank geht an

- Herrn Prof. Dr. Wolfgang Ertmer für die Betreuung der Arbeit von Seiten der Universität Hannover sowie die Anregungen und den Erfahrungsaustausch innerhalb des Sonderforschungsbereichs,
- Herrn Prof. Dr. Fritz Riehle für die Betreuung der Arbeit von Seiten der Physikalisch-Technischen Bundesanstalt, sein Engagement und viele aufschlussreiche Diskussionen,
- Herrn Dr. Uwe Sterr für die zahlreichen interessanten Gespräche und Diskussionen, in denen ich sehr viel gelernt habe, sowie für die experimentellen Anleitungen. Seine Ideen und Anregungen haben wesentlich zum Gelingen dieser Arbeit beigetragen.
- Herrn PD Dr. Christian Lisdat für die tatkräftige Unterstützung im Labor sowie viele Gespräche,
- Herrn Dr. Carsten Degenhardt für die Einführung in das Calcium-Experiment, die vielen geduldigen Erklärungen dazu sowie die experimentellen Grundlagen, die er in seiner Arbeit gelegt hat,
- Herrn Dr. Hardo Stoehr für seine schönen Diodenlaser, auf denen ich meine Arbeit wunderbar aufbauen konnte,
- Herrn Dipl.-Phys. Felix Vogt für die Zusammenarbeit im Labor,
- Herrn Dr. Thomas Legero für die Diskussionen zum Thema FEM-Simulationen und thermisches Rauschen,
- Herrn Dr. Paul-Eric Pottie für die Gespräche über den Dick-Effekt sowie Quantenoptik im allgemeinen,
- Herrn Dr. Harald Schnatz für die Unterstützung beim Aufbau der Faserstabilisierungsstrecke, die Messungen mit dem Frequenzkammgenerator, die Leihgabe seiner elektronischen Ausrüstung sowie die zahlreichen Diskussionen,
- Herrn Dipl.-Ing. Burghard Lippardt für die Messungen mit dem Frequenzkammgenerator sowie die Erklärungen dazu,
- Frau Dr. Gesine Grosche für ihr Interesse am Calcium-Experiment, viele aufschlussreiche Diskussionen und die Aufmunterungen zwischendurch,
- Herrn Dr. PD Ekkehard Peik und Herrn Dr. Christian Tamm für die Diskussionen über optische Uhren und Laser sowie die Vergleichsmessungen mit dem Yb-Laser,
- Herrn Dipl.-Ing. Friedhelm Mensing und Herrn Dipl.-Ing. Mattias Misera für ihre elektronischen Meiserwerke und die Erklärungen dazu sowie Frau Marion Wengel für viele elektronische Schaltungen,

-
- Herrn M.Sc. J.S. Raaj Vellore Winfred für das Korrekturlesen der Arbeit,
 - Herrn Klemens Budin, Herrn Patrik Knigge und Herrn Hans-Peter Weßelhöft für die hervorragenden mechanischen Arbeiten sowie Herrn Budin für seine Unterstützung beim Aufbau der Halterung für den Referenzresonator,
 - Herrn Albert Dettmer[†] für die präzise und zuverlässige Bearbeitung vom Referenzresonator,
 - Frau Birgit Voss, Frau Elke Hünitzsch, Frau Katrin Pfennig und Frau Gunhild Faber für ihre freundliche Unterstützung in allen administrativen Fragen.

Diese Arbeit würde gefördert von der Deutschen Forschungsgemeinschaft im Rahmen des Sonderforschungsbereichs 407 „Quantenlimitierte Messprozesse mit Atomen, Molekülen und Photonen“.